

**DEVELOPMENT OF ALUMINA BASED FEEDSTOCK FOR FUSED
DEPOSITION MODELLING 3D PRINTER**

TAN ROE DJER

**A project report submitted in partial fulfilment of the
requirements for the award of Bachelor of Engineering
(Hons.) Mechanical Engineering**

**Lee Kong Chian Faculty of Engineering and Science
Universiti Tunku Abdul Rahman**

May 2020

DECLARATION

I hereby declare that this project report is based on my original work except for citations and quotations which have been duly acknowledged. I also declare that it has not been previously and concurrently submitted for any other degree or award at UTAR or other institutions.

Signature : Roe Djer

Name : Tan Roe Djer

ID No. : 1505057

Date : 17/05/2020

APPROVAL FOR SUBMISSION

I certify that this project report entitled “**DEVELOPMENT OF ALUMINA BASED FEEDSTOCK FOR FUSED DEPOSITION MODELLING 3D PRINTER**” was prepared by **TAN ROE DJER** has met the required standard for submission in partial fulfilment of the requirements for the award of Bachelor of Engineering (Hons.) Mechanical Engineering at Universiti Tunku Abdul Rahman.

Approved by,

Signature

:



Supervisor

:

Dr. Ting Chen Hunt

Date

:

17/05/2020

Signature

:



Co-Supervisor

:

Dr. Tey Jing Yuen

Date

:

17/05/2020

The copyright of this report belongs to the author under the terms of the copyright Act 1987 as qualified by Intellectual Property Policy of Universiti Tunku Abdul Rahman. Due acknowledgement shall always be made of the use of any material contained in, or derived from, this report.

© 2020, Tan Roe Djer. All right reserved.

ACKNOWLEDGEMENTS

I would like to thank everyone who had contributed intellectually, financially, and mentally to the successful completion of this project. I would like to express my gratitude to my research supervisor, Dr. Ting Chen Hunt, and my co-supervisor, Dr. Tey Jing Yuen for his invaluable advice, guidance and his enormous patience throughout the development of the research.

In addition, I would also like to express my gratitude to my loving parents had assisted me financially and given me heartfelt encouragement throughout my project. Undeniably, my friends who are always standing by my side deserve my appreciation. We aided each other whenever help was requested. Knowledge was shared selflessly and encouragement was given out generously.

Lastly, I would like show my gratitude to the UTAR administration that had provided me key equipment and supplies for my research and had permitted me to undergo my research whether inside or outside the campus smoothly without bothersome troubles.

ABSTRACT

Alumina is ceramics with excellent properties such as chemical inertness, high hardness, and thermal stability. However, alumina product forming process like powder metallurgy, casting, and plastic forming could be troublesome as alumina shape manipulation is inflexible. Integration of additive manufacturing (AM) with alumina formulation is a potential game changer that revitalize the alumina forming industry due to flexibility and customizability of AM. In fact, there have been studies done regarding to alumina 3D printing. However, question still remain on the development of alumina-based feedstock for fused deposition modelling (FDM) 3D printing due to very few studies in this sector. Therefore, alumina-based feedstock for FDM 3D printer was developed and investigated in this study. The in-depth understandings provided in this study could guide the alumina manufacturing industry in formulation of complex shape alumina such as body armour as well as rapid alumina prototyping. This work was initiated with doping of 1 wt% Titanium dioxide (TiO_2) into alumina powder to reduce the sintering temperature of alumina. Cellulose acetate (CA) as a binder was then mixed with acetone with concentration of 100 g/L, 150 g/L, and 200 g/L to form a transparent solution. The transparent solution was mixed with alumina powder with binder-solvent volume occupation up to 90 vol% to form a slurry. It was followed by preparation of green samples from the slurry and they were debinded and pressureless sintered at 1400 °C for an hour. Characteristic tests were done to determine the flow curve of the slurries as well as the bulk density and the hardness of the sintered samples. X-ray diffraction (XRD) and microstructure analyses were conducted to further reflect the properties of the samples. Sample prepared by CA-acetone concentration of 200 g/L with 80 vol% binder exhibited the highest bulk density of 2.963 g/cc (75 % relative density), the highest microstructural compaction, and appropriate slurry viscosity as required by FDM. As a result, it is feasible to apply alumina-based feedstock with CA as binder in FDM 3D printer.

TABLE OF CONTENTS

DECLARATION	ii
APPROVAL FOR SUBMISSION	iii
ACKNOWLEDGEMENTS	v
ABSTRACT	vi
TABLE OF CONTENTS	vii
LIST OF TABLES	x
LIST OF FIGURES	xii
LIST OF SYMBOLS / ABBREVIATIONS	xvi

CHAPTER

1	INTRODUCTION	1
	1.1 General Introduction	1
	1.2 Importance of the Study	3
	1.3 Problem Statement	3
	1.4 Aims and Objectives	4
	1.5 Scope and Limitation of the Study	4
	1.6 Contribution of the Study	5
	1.7 Outline of the Report	5
2	LITERATURE REVIEW	7
	2.1 Introduction	7
	2.2 Ceramics	7
	2.2.1 Alumina	9
	2.2.2 Ceramic / Alumina Forming Process	14
	2.3 Effect of Powder Size	22
	2.4 3D Printing	23
	2.4.1 Types of 3D Printing	27

2.5	Cellulose Acetate (CA)	34
2.6	Binder Removal	38
2.7	Sintering	41
	2.7.1 Sintering Behaviour of TiO ₂ -Doped Alumina	45
2.8	Ceramography	47
	2.8.1 Thermal etching	48
2.9	X-Ray Diffraction of Alumina, CA, and TiO ₂	49
2.10	Summary	51
3	METHODOLOGY AND WORK PLAN	52
3.1	Introduction	52
	3.1.1 Raw Materials	52
	3.1.2 Preparation of TiO ₂ -doped Alumina Powder	53
	3.1.3 Preparation of <i>Green</i> Samples	54
	3.1.4 Rheological Test on Slurry	57
	3.1.5 Binder removal and Sintering	57
	3.1.6 Grinding and Polishing	58
	3.1.7 Thermal Etching	59
	3.1.8 Bulk Density Measurement	59
	3.1.9 Vickers Hardness Determination	60
	3.1.10 Microstructure Investigation	62
	3.1.11 X-Ray Diffraction (XRD)	63
3.2	Work Plan Gantt Chart	64
3.3	Summary	64
4	RESULTS AND DISCUSSION	65
4.1	Introduction	65
4.2	Doping of TiO ₂ into Alumina Powder	65
4.3	Flow Curve	66
4.4	Condition of Powder and Sintered Samples	69
4.5	Bulk Density	72

4.6	Vickers Hardness	76
4.7	XRD Analysis	78
4.8	Microstructure Analysis	81
4.9	Summary	83
5	CONCLUSION AND RECOMMENDATIONS	85
5.1	Conclusion	85
5.2	Recommendation for future work	86
	REFERENCES	87
	APPENDICES	93

LIST OF TABLES

Table 2.1:	High-alumina Engineering Ceramics (Auerkari, 1996).	10
Table 2.2:	Engineering Alumina Grades A6 – A9 (Auerkari, 1996).	11
Table 2.3:	Examples of Compositions of Extruded Alumina.	20
Table 2.4:	Comparison of Ceramic Forming Processes (Black and Kohser, 2011).	21
Table 2.5:	CA's Acetyl and Acetic Acid Content in Different DS (Bao, 2015).	35
Table 2.6:	Organic Binders and Their Maximum Decomposition Temperature.	40
Table 2.7:	Alumina Sintering Result (Roy, et al., 1993).	44
Table 2.8:	Relative bulk density of alumina product with increasing weightage of TiO ₂ (Ting, et al., 2008).	46
Table 3.1:	Properties of CA from Sigma Aldrich, USA.	52
Table 3.2:	Volume Composition of TiO ₂ -doped Alumina Powder, CA, and Acetone for 3 Different Concentrations of Binder (Total of 9 Samples).	55
Table 3.3:	Weight of CA and TiO ₂ -doped Alumina with Acetone Volume for Each of the Samples.	56
Table 3.4:	Final Year Project Part I Gantt Chart.	64
Table 3.5:	Final Year Project Part II Gantt Chart.	64
Table 4.1:	The Final Weight, Initial Weight, and the Percentage Difference of the TiO ₂ -doped Alumina Powder for Two Batches.	66
Table 4.2:	Table of Shear Rate Range that Falls between Viscosity of 10 to 100 Pa·s for Different CA-Acetone Concentration and Volume Occupation.	69
Table 4.3:	The Bulk Density and Relative Density Results for Sintered TiO ₂ -doped Alumina Samples.	73

Table 4.4:	Comparison of Relative Bulk Density of Different 3D Printing Method.	75
Table 4.5:	Table of Vickers Hardness Results of Samples Binder 80 vol% with Three Different CA-Acetone Concentration.	76
Table 4.6:	Comparison of Results on Hardness with Different Sources.	77

LIST OF FIGURES

Figure 2.1:	Structure of Crystalline and Non-Crystalline SiO ₂ (Ben Best, 2008).	9
Figure 2.2:	The structure of α -alumina (Kumar, Prabhakar and Saini, 2013).	13
Figure 2.3:	Dry Pressing Steps (Carter and Norton, 2013).	15
Figure 2.4:	Isostatic Pressing Process (Ruslam, 2009).	17
Figure 2.5:	Slip Casting Processes (Encyclopaedia Britannica, 2016).	18
Figure 2.6:	Injection Moulding Process Schematic Diagram (Carter and Norton, 2013).	19
Figure 2.7:	Graph of Tensile Strength vs Mean Diameter of Glass Bead Particle Size (Sofia, Barletta, and Poletto, 2018).	22
Figure 2.8:	Hardness, Yield Stress, and Compressive Strength for Different Alumina Particle Sizes (Rahimian, et al., 2009).	23
Figure 2.9:	Principle of Subtractive Manufacturing and Additive Manufacturing (Jakus, 2018).	24
Figure 2.10:	Processes and Principles of 3D Printing (Jasveer and Jianbin, 2018).	26
Figure 2.11:	AM Processes (Wong and Hernandez, 2012).	28
Figure 2.12:	FDM Schematic Diagram (Singh and Garg, 2016).	30
Figure 2.13:	Types of Extrusion in AM (Gonzalez-Gutierrez, et al., 2018).	30
Figure 2.14:	SL Process Schematic Diagram (Jasveer and Jianbin, 2018).	31
Figure 2.15:	DLP Process Schematic Diagram (Jasveer and Jianbin, 2018).	32
Figure 2.16:	IJP Schematic Diagram (Chen, et al., 2019).	33

Figure 2.17:	Structural Formula of CA (McKeen, 2019).	34
Figure 2.18:	Solubility of CA in Different Organic Solvents (Bao, 2015).	36
Figure 2.19:	Graph of relationship between melting temperature T_m , glass transition temperature T_g , and decomposition temperature T_d with various degrees of substitution of CA (Bao, 2015).	37
Figure 2.20:	Thermogram of DS 2.5 CA (Bao, 2015).	37
Figure 2.21:	Graph of T_d of CA DS 2.46 against M_w which determined by Thermogravimetry (TG) Analysis (Kamide and Saito, 1985).	37
Figure 2.22:	Binder Removal Model (Becker and Gmbh, 2006).	39
Figure 2.23:	CA TG Analysis Thermogram (Trivedi, et al., 2015).	41
Figure 2.24:	PEG Decomposition With and Without Alumina (Becker and Gmbh, 2006).	41
Figure 2.25:	Effect of Sintering (Kang, 2005).	42
Figure 2.26:	Graphs of Relative Sintered Density against Sintering Temperature (Pulgarín and Albano, 2015).	43
Figure 2.27:	Graphs of Mean Grain Size against Sintering Temperature (Pulgarín and Albano, 2015).	43
Figure 2.28:	SEM Image on Sintered Alumina at 1600 °C (Pulgarín and Albano, 2015).	43
Figure 2.29:	Isodensity Curves of Alumina under Pressureless Sintering (Roy, et al., 1993).	45
Figure 2.30:	The relationship between TiO_2 addition, sintering temperature, and Vickers hardness on alumina (Ting, et al., 2008).	46
Figure 2.31:	The relationship between TiO_2 addition, sintering temperature, and Young's modulus on alumina (Ting, et al., 2008).	46
Figure 2.32:	Ceramographic etching methods (Taffner, et al., 2004).	47
Figure 2.33:	Microstructure of thermally etched and cold isostatically pressed alumina (Chinn, 1998).	48

Figure 2.34:	SEM image of thermally etched alumina sintered at 1400 °C (Chinelatto, et al., 2012).	49
Figure 2.35:	XRD Pattern of Pure α -Alumina Powder (Barma and Mandal, 2014).	50
Figure 2.36:	XRD Pattern of Pure CA and Chitosan (Kamal, et al., 2018).	50
Figure 2.37:	XRD Pattern of TiO ₂ (Theivasanthi and Alagar, 2013).	50
Figure 3.1:	Graph of Chamber Temperature over Time.	58
Figure 3.2:	Vickers Hardness Test Schematic Diagram (Mohamed and Hegazy, 2017).	61
Figure 3.3:	Hitachi SEM model S-3400N	62
Figure 3.4:	XRD Device in UTAR	63
Figure 4.1:	Flow Curve for Processed Alumina Samples with Binder CA-Acetone Concentration of 100 g/L.	67
Figure 4.2:	Flow Curve for Processed Alumina Samples with Binder CA-Acetone Concentration of 150 g/L.	67
Figure 4.3:	Flow Curve for Processed Alumina Samples with Binder CA-Acetone Concentration of 200 g/L.	68
Figure 4.4:	SEM Micrographs of Undoped, Unball-milled Spray Dried Grade Alumina Powder.	70
Figure 4.5:	SEM Micrographs of TiO ₂ -doped, Ball-milled Alumina Powder.	70
Figure 4.6:	Sintered Samples with Undoped, Unball-milled Alumina Powder.	71
Figure 4.7:	Sintered Samples with TiO ₂ -doped, Ball-milled Alumina.	71
Figure 4.8:	Bar Chart of Comparison between Relative Density of TiO ₂ -doped Alumina Samples.	74
Figure 4.9:	XRD Pattern and “Search and Match” Result of Samples with CA-acetone Concentration of 100 g/L and CA-acetone Volume Occupation of 80 vol%.	79

- Figure 4.10: XRD Pattern and “Search and Match” Result of Samples with CA-acetone Concentration of 150 g/L and CA-acetone Volume Occupation of 80 vol%. 80
- Figure 4.11: XRD Pattern and “Search and Match” Result of Samples with CA-acetone Concentration of 200 g/L and Binder CA-acetone Volume Occupation of 80 vol%. 81
- Figure 4.12: SEM Micrographs of $\times 1000$ Magnification of TiO₂-doped Alumina Sample with CA-acetone Volume Occupation of 80 vol% and CA-Acetone Concentration of (a) 100 g/L, (b) 150 g/L, and (c) 200 g/L; Sintered at 1400 °C. 82
- Figure 4.13: SEM Micrographs of $\times 5000$ Magnification of TiO₂-doped Alumina Sample with CA-acetone Volume Occupation of 80 vol% and CA-Acetone Concentration of (a) 100 g/L, (b) 150 g/L, and (c) 200 g/L; Sintered at 1400 °C. 83

LIST OF SYMBOLS / ABBREVIATIONS

a	Half of the average diagonal lines length across the indentation, m
b	width of specimen, mm
C	Half of the average crack length, m
D	arithmetic mean of two diagonals, $D1$ and $D2$, mm
L	length of specimen, mm
E	Elastic modulus, Pa
F	Applied load, N
F_f	Fundamental resonant frequency of bar in flexure, Hz
H_V	Vickers hardness, kg/mm ²
K_{IC}	Fracture toughness, MPa m ^{0.5}
m	mass of specimen, g
M_i	chain molecular weight, g/mol
M_n	number average molecular weight, g/mol
M_{WA}	acetyl group molecular weight, g/mol
M_{WC}	cellulose monomer molecular weight, g/mol
N_i	number of chains of M_i
t	thickness of specimen, mm
T_d	decomposition temperature, K
T_g	glass transition temperature, K
T_m	melting temperature, K
T_l	Correction factor for fundamental flexural mode
w_a	weight in air, g
w_w	weight in water, g
$\%_{Acetyl}$	acetyl content, wt%
ρ	density, g/cm ³
ρ_w	Distilled water density, g/cm ³
μ	Poisson's ratio of the specimen/alumina at room temperature

ABS	acrylonitrile butadiene styrene
AM	additive manufacturing
BJP	binder jetting printing
CA	cellulose acetate
CAD	computer-aided design
CIP	cold isostatic pressure
DIW	direct ink writing
DLP	digital light processing
DS	degree of substitution
EBM	electron beam melting
FDM	fused deposition modelling
HIP	hot isostatic pressure
IJP	inkjet printing
LENS	laminated engineering net shaping
LOM	laminated object manufacturing
PC	polycarbonate
PEG	polyethylene glycol
PPSF	polyphenylsulfone
PVA	polyvinyl alcohol
SEM	scanning electron microscope
SL	stereolithography
SLM	selective laser melting
SLS	selective laser sintering
STL	stereolithography file format
TG	thermogravimetry
TiO ₂	Titanium dioxide
TPP	two-photon polymerisation
XRD	X-Ray diffraction
ZBC	zirconium basic carbonate

CHAPTER 1

INTRODUCTION

1.1 General Introduction

Ceramic materials have a long history in mankind; from potteries to semiconductors; from household products to medical and dental implants; due to its excellent properties such as hardness, mechanical strength, decent thermal stability, chemical inertness, and practical magnetic and electrical performance. Ceramics are categorized as inorganic solids that are generally associated with combination of bonding – ionic, covalent, and perhaps, metallic (Carter and Norton, 2013). Alumina or aluminium oxide is one of the key ceramic materials. There are a lot of ceramic forming techniques, which are primarily powder compaction, casting, and plastic forming. Commonly, the products or *greens* require further modifications and processes before they can be accepted by the users. Drying, debinding, and sintering are the conventional ways to amend, densify, and enhance the properties of *greens*.

AM has become one of the hot topics in the fourth industrial revolution. It is sometimes called as 3D printing. Before the introduction of AM in the mankind, the manufacturing methods in mankind have been mainly subtractive or “top-down” in nature where isolated raw materials were collected and subsequently processed, machined, and lastly reduced into smaller and detailed final products (Jakus, 2018). Subtractive manufacturing techniques contain substantial amount of limitations; for examples, inflexibility and no customizability in production, produce piles of waste and less environmentally friendly, and more production steps required. AM is predicted to have potential in aiding many fields. Currently, it has served vastly in rapid prototyping, medical applications, lightweight manufacturing industries, et cetera. Contrary to subtractive manufacturing, the working principles of AM are initially modelling through computer-aided design (CAD) software and converting the model into reality by constructing it layer by layer, bit by bit until the model is fully formed. The evolving of 3D printing technologies has led to invention of various types of 3D printers such as stereolithography (SL) and FDM.

Introducing and integrating AM into the production of ceramics have been being a potential in creating a great advancement in the industries. The traditional manufacturing techniques mentioned previously comprise numerous drawbacks; for instances, high manufacturing costs, inability of rapid prototyping, new product shape requires new mould, machining of ceramic products is difficult and troublesome due to their brittle properties, and the struggle in manufacturing complex cross section ceramic products (Chen, et al., 2019). Without a doubt, ceramic 3D printing is a game-changing opportunity to ceramic manufacturing industries. Today, the technology of ceramic 3D printing has progressed swiftly. AM in ceramic materials is being divided into three main parts regarding to its feedstock form: slurry, powder, and bulk solid methods.

Since public attentions have driven towards ceramic 3D printing, there have been researches done in respect with this topic. Hamano and Ikoma (2018) applied 3D ink-jet powder laminating printer and discovered that polyallylamine is a better binder as compared to polyvinyl alcohol due to interaction between negatively charged alpha alumina particles with polyallylamine; sadly, the alumina they printed has only 40% relative density and 8.2 kPa compressive strength, even after sintering at 1500 °C, the compression strength increased up to only 1.7 – 3.6 MPa which is much lower than conventional manufactured alumina. Peng, et al. (2018) had researched on inkjet printing (IJP) process which its feedstock consists of alumina nano-powder, acrylic acid, ethylene glycol, and deionized water and it resulted into final sintered alumina product with 95% relative density and 10.80% of porosity after sintering at 1550 °C. On the other hand, Zhang, Sha and Zhao (2016) and Zhou, et al. (2016) had printed alumina product through SL technique and have decent relative density of the final sintered product which was up to 99.3%. Hatzenbichler, et al. (2012) had conducted alumina 3D printing through digital light processing (DLP) and resulted into 99.6% relative density of final product. According to Chen, et al. (2019), researches on the surface roughness improvements of FDM printed ceramic products are hardly to be found. One of the very few studies was done by Agarwala, et al. (1996) regarding to elimination of defect such as sub-perimeter void, core void, and inter-road

defect through modification of printing path. Agarwala also produced a GS-44 silicon nitride sample containing 98 % (after sintering) through FDM method.

In this thesis, the investigation on alumina-based feedstock for FDM 3D printer is going to be the centre of attention as this study is hardly to be found. In this case, CA will be used as the binder due to its renewability and biodegradability. The physical properties: rheological properties and bulk density; the mechanical properties: hardness; as well as the microstructure analysis and the XRD analysis will be investigated on the alumina-based feedstock for FDM.

1.2 Importance of the Study

AM is listed as one of the criteria of fourth industrial revolution and it advances quickly due to attention of the communities. It is essential to conduct research regarding to AM. This study may offer a clearer explanation on the applicability of alumina-based feedstock for FDM 3D printing as well as generating a profound understanding of the physical and mechanical properties on sintered alumina product with CA as binder. It may lay the foundation for alumina FDM 3D printing field.

1.3 Problem Statement

Problem statement of this study regarding to alumina-based feedstock for FDM 3D printer are summarized as follows:

- The traditional manufacturing methods of alumina products such as powder metallurgy, casting, and plastic forming are very low in flexibility. FDM 3D printer could be the solution for flexibility in production.
- There have been lots of researches done on ceramic 3D printing in terms of SL, IJP, and BJP due to its potential in high flexibility and customizability; however, questions still remain on the properties of alumina-based feedstock for FDM 3D printing due to very few studies in this sector.

1.4 Aims and Objectives

The overall purpose of this work is to develop alumina-based feedstock for FDM 3D printer. The detailed objectives of this study are as follows:

- To formulate the best alumina – binder composition of feedstock for FDM 3D printing.
- To investigate the physical properties; in terms of rheological properties of the alumina – binder slurry and bulk density of the sintered alumina-based samples.
- To determine the mechanical properties; in terms of hardness of the sintered alumina-based samples followed by microstructure and XRD analyses.

1.5 Scope and Limitation of the Study

This study is conducted in Universiti Tunku Abdul Rahman in year 2019 to 2020. This project covers the preparation of ceramic suspension containing alumina, CA, and acetone by manipulating the CA-acetone concentration: 100 g/L, 150 g/L, and 200 g/L; and the CA-acetone volume occupation or the binder-solvent loadings: 70 vol%, 80 vol%, and 90 vol%. The process is followed by heat treatment on the samples for binder removal and sintering purpose to enhance the properties of *green*. Moreover, it comprises the different methods of data determination, in physical properties determination: bulk density measurement by water immersion method and rheological test by rheometer; in mechanical properties determination: hardness test by Vickers hardness test; for microstructure analysis: scanning electron microscope (SEM); and XRD analysis.

However, this work is subjected to limitations. The dimension of the samples is hard to maintain constant due to its cracking nature after drying and shrinking. In addition, the evaporation rate of acetone is hard to maintain too and too fast the evaporation rate could lead to faster shrinkage and more cracks. Optimum sintering temperature of pure alumina is at 1550 °C and be held for 3 hours; However, the equipment available for heat treatment is the carbolite furnace which could be heated until only 1400 °C and be held not more than 1 hour. If doping is allowed, it has to be made sure the doping composition would not affect much on the properties of the final products. The sintering method

applied is only conventional method while there are still various types of sintering in the industries such as spark plasma sintering and two steps sintering. Moreover, this study comprises only certain kinds of properties, which are rheological properties, bulk density, hardness, XRD analysis and microstructure, but not fatigue limit, creep, and other electrical, thermal, chemical, and magnetic properties.

1.6 Contribution of the Study

The findings of the study would contribute greatly in benefiting the societies especially fields that associated to technologies and engineering. With the advancement of the AM industry, the demand of a series of practical, effective, and efficient options in AM is aroused. Also, the success of this study would cause alteration of traditional alumina forming method into the flexible 3D printing method. This study could contribute an in-depth understanding on the alumina-based feedstock for FDM 3D printers that allow the researchers and engineers to enhance their confidence in decision making for further researches and applications. This study reveals the critical area which is the alumina FDM 3D printing in AM researches that is being overlooked. In addition, this study could boost the interest of the societies and draw their attention towards AM by visualizing the potential of this industry. As a result, it could speed up the development of AM to become a mature technology and contributes vastly to the societies. Individually, this study provides comprehensive knowledge, experience, and opportunity that enlighten my path in engineering fields especially the AM.

1.7 Outline of the Report

This report is going to show five main parts: introduction, literature review, the methodology and work plan, results and discussion, and conclusion and recommendations. "Introduction" is going to briefly discussed about the title, the importance, problem statement, objectives, scope, limitations, and contribution of this study. It is planting an idea on how this study is motivated, the expectations of the study outcome, and the presumptions of problems to the readers so that they will not simply be detached from the main focus of this reports.

“Literature review” is a part where comprehensive studies from other sources like researches, journals, and textbooks are written in. The readers are expected to understand the fundamental knowledge; such as ceramic and alumina properties, current AM technologies, sintering of alumina, thermal decomposition of CA, and doping in alumina; as well as comprehend the similar work and results done by other researches regarding to this topic. With the understandings gained from “literature review”, the readers could be easily keeping up with the following chapters.

“Methodology and work plan” is a section where the particulars of raw materials, the detailed preparation procedures of the experiment, the data determination methods and their theories, as well as the work plan Gantt chart. After thorough study in this section, the readers are expected to know how this experiment is conducted, what the details of raw materials are, how data is collected, and the work plan for this experiment.

“Results and discussion” chapter is the essence of this report where the facts and figures of the results are being revealed and discussed briefly with interpretation of data, explanation, and comparison of data. After studying this chapter, the readers are able to know the real facts, the differences between the data of this report and others, and the reasons of the data obtained.

Lastly, “conclusion and recommendations” section is going to show the summary of the whole report and the suggestions for future work. After reading this part, the readers shall know whether the objectives and aims have attained, the final decision on the best alumina-based feedstock composition, and how to improve future works.

CHAPTER 2

LITERATURE REVIEW

2.1 Introduction

This chapter is going to show thorough and long literature review and understandings from general principle; for examples, ceramics and properties of alumina; to detailed researches; for instances, the temperature that CA starts to decompose for binder removal purpose. Literature review is a necessary for this study as other researchers are being able to provide useful information and this could assist in time-saving and knowledge imparting.

2.2 Ceramics

“Ceramic” is going to be one of the most common used phrases in this report. This word is originated from *kéramos* from Greek or “*potter’s clay*”. Unlike metal and polymer, a ceramic is an inorganic material that is comprised of two or more metallic and non-metallic elements (Black and Kohser, 2011). The elements are mainly bonded with each other in covalent as well as ionic bonds, sometimes, metallic bonds, this can be said that the ceramics are having “blended” bonding.

Ceramics are not unfamiliar to human kind due to its utilization in various kinds of applications and industries; for example, machinery, aerospace engineering, biomedical sector, chemical engineering; and even way back to thousand years ago where human started to fabricate crockery and glassware. Excellent ceramic characteristics and properties are the source of mankind’s reliability on them. It is very misleading and wrongful to assume all of the ceramics are having the same properties instead of “close properties”. The properties of ceramics to be looked at later will prove the previous statement.

Brittleness or zero ductility. When it comes to applying ceramics, brittleness is one of the main considerations. Just drop a ceramic flower pot from a considerable altitude and it will experience a tremendous shattering. This happens due to the mixture of ionic and covalent bonding in most of the ceramics that grip the atoms together. Brittleness of ceramics can be assured at room temperature; nonetheless, in elevated temperature above the glass

transition temperature, unlike other ceramics, glass is not brittle anymore and it behaves more like a viscous liquid. This special property allows glass to be easily shaped.

Next, the poor heat and electrical conduction. In metal, the valence electrons are allowed to move freely but this does not apply in ceramics due to the tying up of valence electrons in bonds. The “free electrons” mentioned earlier is the main cause that determines the thermal and electrical properties of a material; yet, Carter and Norton (2013) stated that there are ceramics with high thermal and electrical conductivity; for thermal conductivity, diamond which is a ceramic is known to have the highest thermal conductivity among all of the materials due to phonon is the conduction mechanism instead of electrons; for electrical conductivity, rhenium trioxide with the formula ReO_3 is can conduct electric even though it is a oxide ceramic.

A metal can have a compressive strength which is almost the same with its tensile strength. For ceramics, it can have an exceptionally high compressive strength but with a comparatively low tensile strength that it may be around ten times lower than the compressive strength; for instance, alumina has a compressive strength of 2400 MPa and a tensile strength of just 138 MPa. Therefore, in applications like load-bearing and concrete buildings, compression on ceramics is highly favourable than tension on ceramics to prevent failures. On the other hand, toughness for ceramics are low and its property can be boosted up in composite materials.

Further distinct properties for a ceramic is that it is chemically inert and having an extremely high melting point. Nearly all of the ceramics are stable and insensitive in severe alkaline and acidic as well as harsh thermal environment. This allows ceramic like Pyrex glass to be widely used in laboratories.

There are three types of ceramic categorizations. Firstly, ceramics can be categorized as crystalline and non-crystalline ceramics. Crystalline ceramics like silicon carbide and alumina are more difficult to be manufactured or processed whereas non-crystalline ceramics like glasses tend to be shaped from melts. Figure 2.1 shows the differences in structure of crystalline and non-crystalline silicon dioxide, SiO_2 .

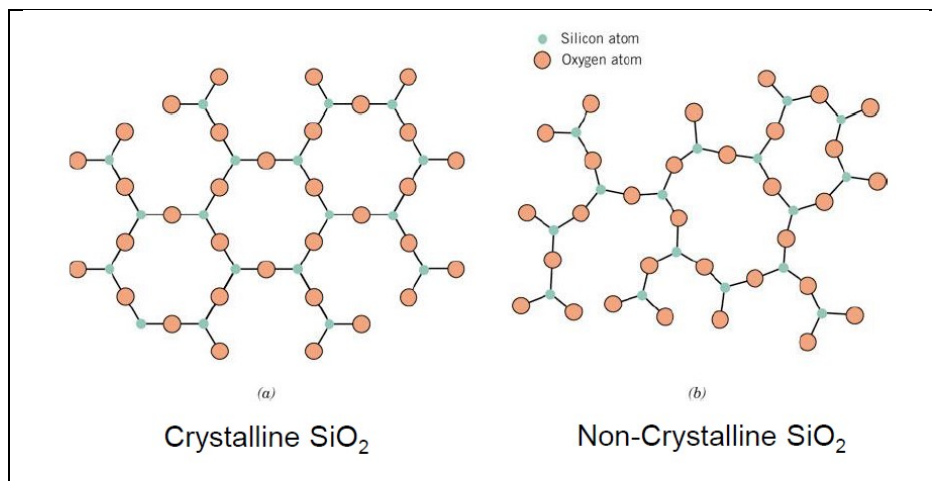


Figure 2.1: Structure of Crystalline and Non-Crystalline SiO_2 (Ben Best, 2008).

Secondly, ceramics can be classified according to its usage: Glasses – optical, composite reinforced, containers; Clay products – whiteware, bricks; Refractories – bricks for high temperature, furnace; Abrasives – sandpaper, cutting, polishing; Cements – composites, structural; and Advanced Ceramics – rotors, bearings, sensors.

Thirdly, ceramics can also be categorized by separating them into oxides, non-oxides, and composite materials. Examples of oxides are alumina and zirconia; examples of non-oxides are carbide and silicide; example of composite materials are fibre reinforced and mixtures of non-oxides and oxides.

2.2.1 Alumina

Ceramics are too general to this project. In this project, alumina is going to be the main subject to be discussed. Alumina, or aluminium oxide, with chemical formula Al_2O_3 , is one of the most valuable, academically evaluated ceramic oxides due to its excellent properties: thermal and chemical stability that it can resist decently towards acids and bases; inert at room temperature; corrosion resistance; electrical and thermal insulation; high hardness; and comparatively good strength. Despite of its attractive features, it is considered as one of the most abundance materials found on Earth. It is widely applied as: an ingredient of producing glass; abrasives; body armour; electrical insulator; paint; composite fibre; catalyst; agent for water purification; etc. In applications, alumina is being categorized into two groups with grades regarding to its purity: Table 2.1 shows the high-alumina grades with 99% of alumina and above, Table

2.2 shows the alumina grades from 80% to 99% of alumina. Both Table 2.1 and 2.2 shows the porosity, density, and applications of different grades of alumina.

Table 2.1: High-alumina Engineering Ceramics (Auerkari, 1996).

Grade	Al₂O₃ (min %)	Type	Porosity (%)	Density (g/cm³)	Applications
A1	99.6	Electrical and Engineering	0.2 – 0.3	3.75 – 3.95	Structural
A2	99.8	Translucent	<1	3.97 – 3.99	Na Lamps
A3	99.5	Hot-pressed	<1	3.90 – 3.99	Machine Tools
A4	99.6	Sintered Recrystallised	3 – 6	3.75 – 3.85	Refractory
A5	99.0	Low Dielectric Loss	1 – 5	3.76 – 3.94	Microwave

Table 2.2: Engineering Alumina Grades A6 – A9 (Auerkari, 1996).

Grade	Al₂O₃ (%)	Type	Porosity (%)	Density (g/cm³)	Applications
A6	96.5 – 99.0	Electrical and Engineering	1 – 5	3.71 – 3.92	Mechanical & Electrical
A7	94.5 – 96.5	Electrical and Engineering	2 – 5	3.60 – 3.90	Insulators, Wear Parts
A8	86.0 – 94.5	Electrical and Engineering	2 – 5	3.40 – 3.90	Insulators, Wear Parts, Refractory
A9	80.0 – 86.0	Electrical and Engineering	3 – 6	3.30 – 3.60	Insulators, Wear Parts, Refractory

Different crystalline phases or polymorph can be found in alumina and different phases might having differences in physical and mechanical properties. According to Kumar, Prabhakar and Saini (2013), α , γ , and θ are classified as three of the most essential alumina polymorphs as there are evidence proves that there are at least 20 other phases of alumina. Table 2.3 states the properties of α -, γ -, and θ -alumina.

Table 2.3 Selected Properties of α -, γ -, and θ -alumina (fu = chemical formula unit) (Andersson, 2005).

	α -Al ₂ O ₃	θ -Al ₂ O ₃	γ -Al ₂ O ₃
Density (kg/m³)	3980 – 3990	3560 – 3600	3200 – 3700
Elastic modulus (GPa)	409 – 441	-	-
Hardness (GPa)	28	-	-
Bulk modulus (GPa)	239	-	-
Band gap (eV)	8.8	7.4	
Melting point (°C)	2051	$\theta \rightarrow \alpha$: 1050 °C	$\gamma \rightarrow \delta$: 700– 800 °C
Structural properties of α-Al₂O₃			
Space group	$R\bar{3}c$ (rhombohedral, two fu/cell)		
Lattice parameter	$a=5.128 \text{ \AA}$, $\alpha=55.33^\circ$, $V=42.6 \text{ \AA}^3/\text{fu}$		
Internal coordinates	Al: (4c) $\pm(u, u, u; u+1/2, u+1/2, u+1/2)$, $u=0.352$ O: (6e) $\pm(w, 1/2-w, 1/4; 1/2-w, 1/4, w; 1/4, w, 1/2-w)$, $w=0.556$		
Structural properties of θ-Al₂O₃			
Space group	$C2/m$ (monoclinic, four fu/cell)		
Lattice parameter	$a=11.85 \text{ \AA}$, $b=2.904 \text{ \AA}$, $c=5.622 \text{ \AA}$, $\beta=103.8^\circ$, $V=47.0 \text{ \AA}^3/\text{fu}$		
Internal coordinates	All atoms: (4i) $\pm(u, 0, u; u+1/2, 1/2, w)$, with:		
	Atom	u	w
	Al1	0.917	0.207
	Al2	0.660	0.317
	O1	0.161	0.098
	O2	0.495	0.253
	O3	0.827	0.427
Structural properties of γ-Al₂O₃			
Space group	$Fd\bar{3}m$ (defect cubic spinel structure, 32 fu/cell)		
Lattice parameter	$a \approx 7.9 \text{ \AA}$, $V \approx 46.2 \text{ \AA}^3/\text{fu}$		

In this thesis writing, α -alumina will be the focal point. *Corundum* is the other name for α -alumina and it is considered as the most abundant natural aluminium oxide. *Sapphire* (different in colour depends on the composition of the iron and titanium as impurities) and *rubies* (deep red in colour due to chromium as impurities) are the gemstones for *Corundum*. The chemical bonds for all alumina phases including the α -alumina (with valences of $+2.63e$ for aluminium and $-1.75e$ for oxygen) are predominantly ionic or electrostatic and this one of the reasons that alumina for being so hard (28 GPa). The crystallization of *corundum* is trigonally symmetry and it falls under the space group of $R\bar{3}c$ and it is rhombohedral along with two chemical formula units which consists of 10 atoms in a unit cell as shown in Table 2.3. However, a hexagonal representation which contains 6 chemical formula unit is more commonly used. Due to the two-third occupation of aluminium ions or atoms in the octahedral spaces, *corundum* can also be defined as a hexagonal-close-packed oxygen sublattice (Kumar, Prabhakar and Saini, 2013).

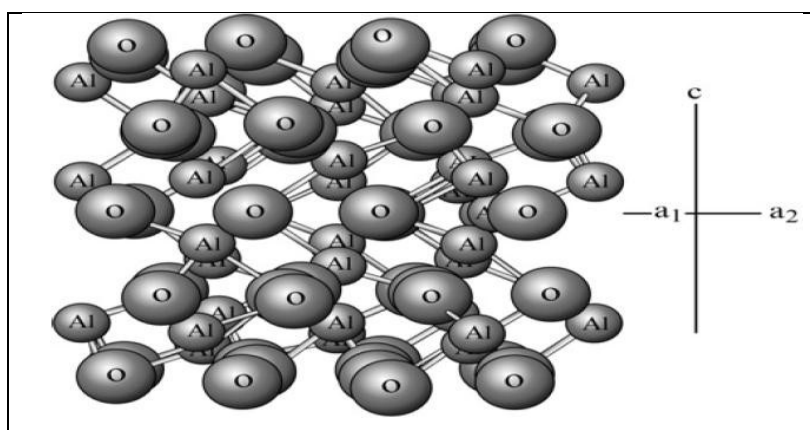


Figure 2.2: The structure of α -alumina (Kumar, Prabhakar and Saini, 2013).

α -alumina possesses a thermodynamic stability that allows it to be implemented in high heat applications. Another stability that α -alumina is having is that it is chemically stable because it does not simply form bonding with other substances and this contributes to its application in highly reactive fields. According to Table 2.3, it can be obtained that α -alumina is having 409 – 441 GPa of elastic modulus and 28 GPa of hardness as it can be compared to the world's current hardest materials, diamond which having 1100 GPa of elastic modulus and 100 GPa of hardness while sole metallic aluminium is

having only 70 GPa of elastic modulus and 0.3 GPa of hardness. The appealing α -alumina properties enhances the production of α -alumina thin film as it is wear-resistant and a decent diffusion barrier coating. 8.8 eV of band gap allows α -alumina to be a great insulator and due to its transparency and thermal stability, α -alumina is widely utilized in optics.

2.2.2 Ceramic / Alumina Forming Process

As mentioned previously in section 2.3.1 and 2.3.2, ceramics including alumina are thermally stable at high temperature, brittle, and a considerable high hardness; therefore, conventional manufacturing processes that involve high tensile stress or require melting of materials such as drawing processes and spinning processes are not practical in ceramic and alumina. However, there are still many methods in forming ceramics products. Ceramic forming processes are being categorized into 3 main parts: Powder compaction (hot pressing, dry pressing, and isostatic pressing), Casting (Slip casting), Plastic forming (extrusion and injection moulding). Before further explanation, some of the significant and common phrases used in ceramics forming processes are as below:

Binder – a substance used to grip the powder together from falling apart by adding it into the powder.

Slurry – a suspension formed with ceramic particles by adding liquid, as the liquid evaporates, the suspension solidifies.

Plasticizer – considered as one of the binders that make the held-ceramic-powder to be pliable, plastic and soft.

Green – A fragile ceramic product before firing process is done.

Slip – a type of slurry utilized in forming glaze during firing process is done.

Binder is one of the most important parts in forming most of the ceramic products. The two reasons of the importance of the binder are: the binder contributes in plasticizing the *green* (for extrusion process) and the binder allows the *green* product to have a higher strength so that it will not collapse in the handling process. However, the binder has to be eliminated. Polymers are often used as binder due to its ability to be eliminated in firing process without

producing any negative effect. Polyvinyl alcohol (PVA) and polyethylene glycol (PEG) are the two commonly used binders in the industries in which they provide sufficient strength and density for the *green*, respectively (Carter and Norton, 2013). In pottery, water is the binder to ease the shaping process of the *green*.

2.2.2.1 Powder Compaction

Powder compaction can be defined as the pressing of ceramics powder. Anand (2014) stipulated that there are a few ways to prepare alumina powder with desired purity and size, which are: decomposition of aluminium salt in high temperature, moisture removing from aluminium hydroxide, and direct machining of fused alumina in the powder form. Three of the common method in powder compaction in forming ceramics are the dry pressing, hot pressing, and isostatic pressing.

Dry pressing is a simple shaping process that comprises three main steps, which are: filling up the die with ceramic powders, pressing the ceramic powders into compacts, and lastly ejecting the compacts. It is a misconception to expect that dry pressing is a shaping process without binder. In fact, less than 5 wt% of binder is added into the ceramic powder in dry pressing. The most preferable particle size of the powder is in between 20 μm to 200 μm and due to big volume fraction, it causes particle flow problem and sticking of the dies. The advantages of applying dry pressing method are the inexpensive equipment and processes; simple; and fast. Therefore, it is implemented in most of the high-volume-ceramic-manufacturing industries. Figure 2.3 illustrates the dry pressing process.

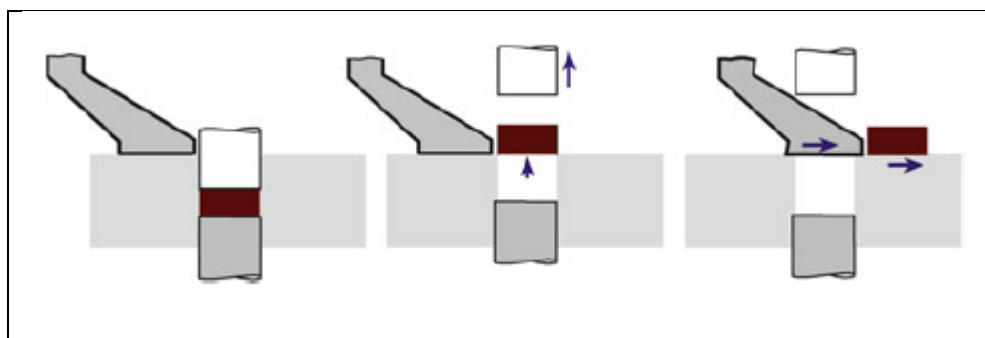


Figure 2.3: Dry Pressing Steps (Carter and Norton, 2013).

If dry pressing is performed in a hot environment, the process is then called the hot pressing. The manufacturing steps and equipment setup for hot pressing is almost the same as dry pressing. Both dry and hot pressings are not achievable for complex shapes of products. The only difference that distinguishes between these two processes is the presence of the high-temperature furnace in hot pressing. The high-temperature environment allows sintering of the ceramic powders to increase the density of the product. Advantages of hot pressing over common dry pressing are that the size of the pores due to random mixing can be diminished; densification at lower temperature at normally 50 % of the melting point of the component than the temperature required for typical low-pressured sintering; the temperature mentioned will not result in secondary recrystallization or over-grain-growth. However, hot pressing process requires expensive dies that can withstand high temperature but normally these dies have shorter tool life. Ceramics such as alumina has a high melting temperature of about 2000 °C and many materials cannot withstand the temperature of half of its melting point. Hot-pressed aluminium oxide products with or without the combination of other materials can be seen in industries and human's daily life; for example, ceramic armours, cutting tool, moulds and dies, microwave absorbers, and sputtering targets.

Isostatic pressing is a ceramic forming process that presses the ceramic powder hydrostatically in a container. The main advantage of isostatic pressing over the previous pressing processes are the uniformity of pressure applied in isostatic pressing. Isostatic pressings can be done with or without the presence of high temperature environment. Figure 2.4 shows the example of cold isostatic process (CIP) which is also known as wet-bag process. First, ceramic powder is poured into the rubber bag followed by sealing of the mouth of the rubber bag with cap. The bag is then placed into a chamber. Fluid (typically oil-water mixture) is filling into the chamber to provide a high hydrostatic pressure environment to the rubber bag and the ceramic powder. The pressure can range from 20 MPa to 1 GPa. Upon the completion of the pressing, the rubber bag is removed after the pressure drops back to atmospheric pressure. The compacted product is taken out for further processing.

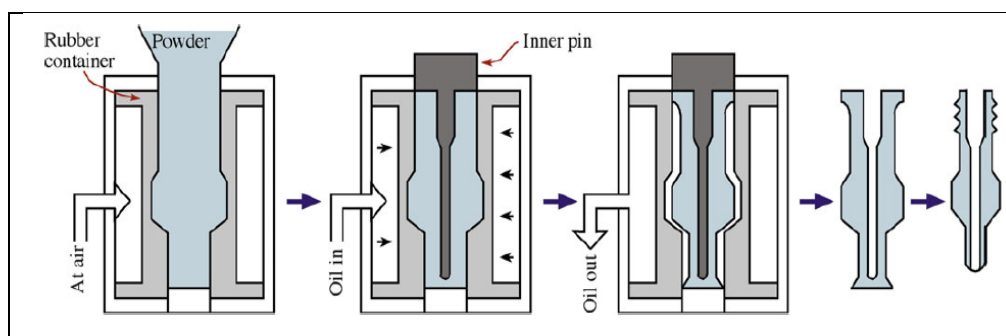


Figure 2.4: Isostatic Pressing Process (Ruslam, 2009).

For hot isostatic pressing (HIP), heat and pressure are simultaneously implemented in the ceramic shaping process. Unlike CIP apparatus arrangement, HIP apparatus is having built-in heater in order to heat the inner chamber up (up to 2000 °C) with pressure between 30 MPa to 100 MPa which is lower than CIP. Another distinction between CIP and HIP is the pressure medium used. Gas (typically Argon) is pumped into HIP apparatus while CIP uses liquid.

2.2.2.2 Casting

Slip casting or drain casting is commonly used in the industries for ceramic casting method. Figure 2.5 depicts clearly the procedure of slip casting from ceramic powder to unfinished ware. To initiate the slip casting process, slurry or slip has to be prepared by mixing the ceramic powder (can be alumina) with liquid. This process is followed by filling up the mould which contains fine pores with the slurry prepared. The liquid is separated from the slurry due to capillary action and the ceramic particles form into *green*. After the formation of the cast, the liquid is then drained off by pressuring the slurry or vacuuming the mould. The *green* is left until partially dried then plugging and separating are done to remove the hollow shape that having the desired thickness.

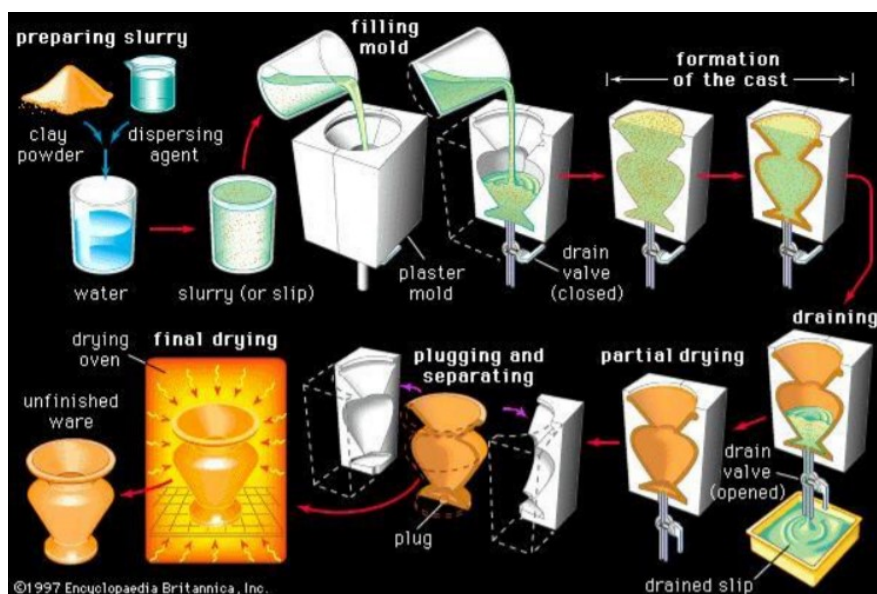


Figure 2.5: Slip Casting Processes (Encyclopaedia Britannica, 2016).

Slip casting has been used since centuries ago and its main purpose was to produce traditional pottery such as jugs and teapots. Today, slip casting has been extensively used in producing advanced ceramic components with complex structure; for example, gas-turbine rotors; due to its low-cost processing.

2.2.2.3 Plastic Forming

From the word “plastic”, it means that the ceramic components have to be pliable and deformable under pressure during the forming process. By adding adequate amount of liquid or binder into ceramic powder, the mixture can be plastic. In traditional plastic forming method, the liquid added to the ceramic powder were mostly water; however, in order to achieve certain viscosity and required burn-out properties, the binders are now more complex with various compositions of components. Extrusion and injection moulding are two of the typical ceramic plastic forming processes. Drawing method is not practical due to weak ceramics tensile strength although it is considered plastic forming.

Injection moulding, in fact, can be easily spotted in thermoplastic polymer processing industries; by applying thermoplastic polymer as a binder in ceramic powder, ceramic forming process through injection moulding can be done. The binder with normally high-volume fraction of organic component allows the ceramic slurry to achieve required rheological properties for injection

moulding. Figure 2.6 describes the injection moulding processes. Initially, the ceramic slurry is being constantly filling up the hopper while the hopper keeps feeding it into the screw conveyor. The screw conveyor moves the mass to the heater and this results in softening of the thermoplastic polymer. Subsequently, the softened slurry fills up the mould and being pressured into the mould. The screw conveyor stops feeding the mould when certain amount of slurry is added into the mould. The mixture slowly cools down accompanied by the hardening of the binder. Due to high-volume fraction of organic component, 15 % to 20 % of shrinkage could happen to the product after sintering and this leads to difficulties in dimensions control; however, complex products can still be produced with low distortion through this forming method due to uniform density provided. Injection moulding requires high costings for initial tooling; yet, it is still widely used in the industries due to its ability for mass production.

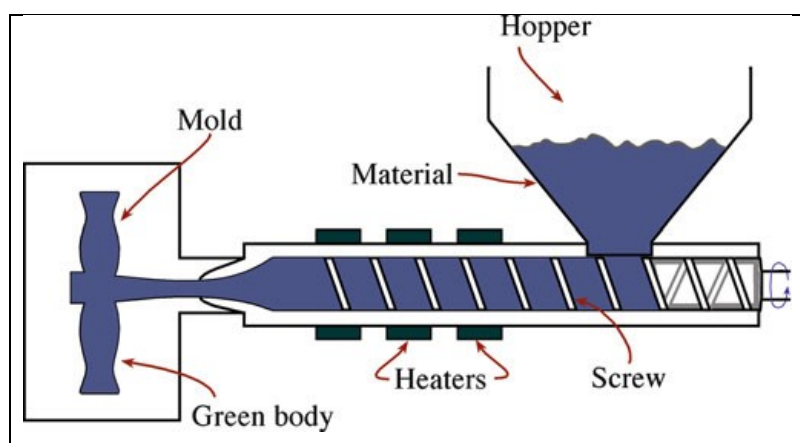


Figure 2.6: Injection Moulding Process Schematic Diagram (Carter and Norton, 2013).

Extrusion is described as applying pressure to a plastic material through a die hole or orifice; therefore, the products for extrusion share the same characteristics which are high length-to-diameter ratio and constant cross-sectional shape (Black and Kohser, 2011). Rheological properties of the clay are very important in extrusion as it has to be self-supporting, unlike injection moulding where mould can hold the slurry. Table 2.3 shows the examples of composition required to extrude alumina.

Table 2.3: Examples of Compositions of Extruded Alumina.

Refractory Alumina	vol%	High Alumina	vol%
Alumina (< 20 μm)	50	Alumina (< 20 μm)	46
Hydroxyethyl cellulose	6	Ball Clay	4
Water	44	Methylcellulose	2
Aluminium Chloride	<1	Water	48
		Magnesium Chloride	<1

Before continuing reviewing the next subtopic, a simple comparison of the ceramic forming processes in terms of feed materials, advantages, and disadvantages are made in Table 2.4.

Table 2.4: Comparison of Ceramic Forming Processes (Black and Kohser, 2011).

Process	Feed Materials	Advantage	Disadvantage
Dry/Hot pressing	Dry powder	Low cost; Ease of automation; Short production time	Density inconsistency; Limited to simple and small shape
Isostatic pressing	Dry powder	Density consistency; Ease of automation; Flexible cross-section	Long production time
Slip casting	Slurry	Large sizes; low tooling cost; complex shapes	Long production time
Injection moulding	Ceramic-plastic mixture	Complex cross-section; Short and high-volume production; Ease of automation	Require for binder burn-out; high initial cost
Extrusion	Ceramic-binder mixture	Low cost; Variable cross-section	Require for binder burn-out; Product limited to high length-to-diameter ratio

2.3 Effect of Powder Size

The raw material of alumina-based feedstock for FDM 3D printer is the alumina powder. Therefore, powder size could draw significant impact towards the properties of final product. Sofia, Barletta and Poletto (2018) has done researches related to the impact of particle size on the properties of sintered glass products. Figure 2.7 illustrates their data of the graph of tensile strength vs mean diameter of glass bead particle and it clearly states that the particle size with mean diameter around $50 \mu\text{m}$ results into the strongest tensile strength of 2200 kPa after sintering. On the other hand, when the particle size is at $184 \mu\text{m}$ and $20 \mu\text{m}$, the tensile strength drops to 200 kPa and 1000 kPa respectively after sintering. It proves that the powder size does affect the final properties and it should not be neither too big nor too small.

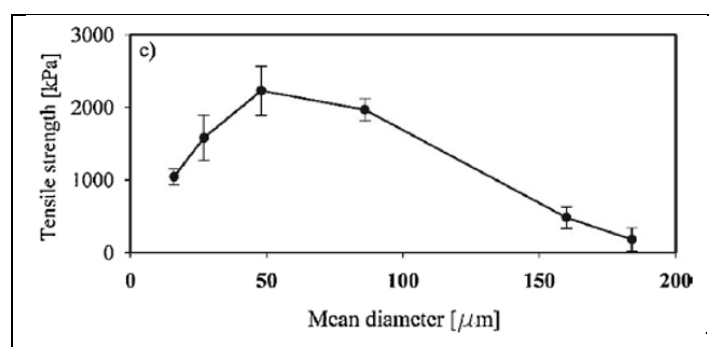


Figure 2.7: Graph of Tensile Strength vs Mean Diameter of Glass Bead Particle Size (Sofia, Barletta, and Poletto, 2018).

Moreover, Rahimian, et al. (2009) did a research to study the effect of alumina particle size. Their result is depicted in Figure 2.8. From Figure 2.8, it can be obviously observed that as alumina particle size decreases, the hardness, yield stress, and compressive stress rises. However, as the alumina particle size is smaller than $4 \mu\text{m}$, the mechanical properties of its final product fall drastically to nearly zero. Consequently, it is important to maintain the particle size in the range between 10 to $50 \mu\text{m}$ to prevent mechanical failure in the final product.

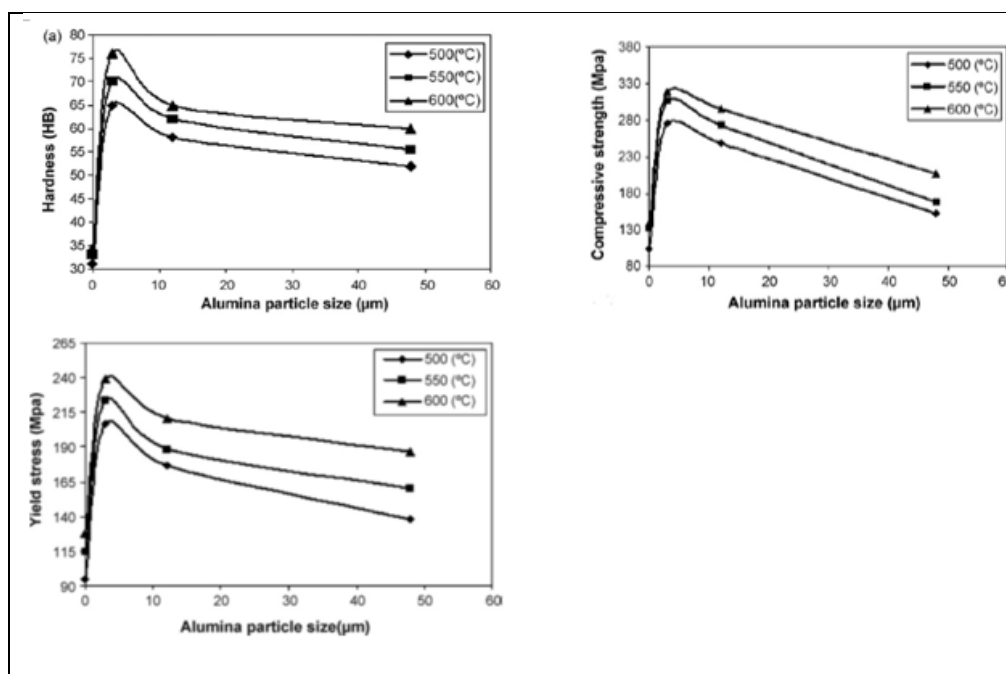


Figure 2.8: Hardness, Yield Stress, and Compressive Strength for Different Alumina Particle Sizes (Rahimian, et al., 2009).

2.4 3D Printing

3D printing or AM is one of the four significant physical evidences for the fourth industrial revolution technological megatrend (Schwab, 2016). Before the invention of AM, things are made and produced mainly on subtractive manufacturing by removing the raw material layer by layer until desired shape is achieved. Contrary to subtractive manufacturing, 3D printing creates physical object by adding layer by layer with the aid of computer-aided design (CAD) in modelling the three-dimensional object. Figure 2.9 illustrates the principle of both subtractive manufacturing and additive manufacturing.

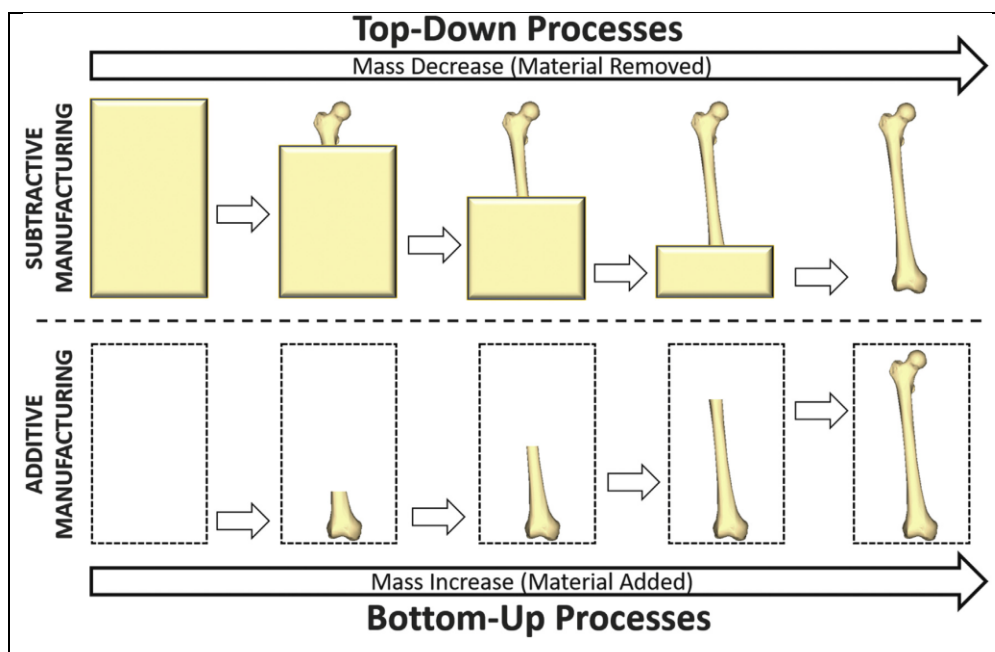


Figure 2.9: Principle of Subtractive Manufacturing and Additive Manufacturing (Jakus, 2018).

The applications of AM are vast; from building large wind turbines to miniature medical implants. The number of filed patents regarding to 3D printing boosted up since 2013 and the average annual increment rate in the number of patents filed from 2013 to 2016 is remarkably 75% (Garechana *et al.*, 2019). Therefore, AM is qualified as an “emergent” technology as its popularity has undergone a tremendous upsurge in the industries.

Long, et al. (2017) and Mukhaimar, Makhool and Samara (2015) both describe profoundly on the advantages and disadvantages of 3D printing as follows. The advantages of 3D printing technology over the other manufacturing methods are:

- in terms of economics;
 - it provides flexibility and customizability in production without causing exorbitant cost; it allows small production batch as contrary to mass-production; it has the potential to support simple and short supply chain with faster lead times and smaller inventories; no mould and tooling is required;
- in terms of environment;
 - it is more environmentally friendly with lesser waste and energy consumption; the waste product is mostly recyclable; no milling, sanding or scrap required;
- in term of technology;

zero skill manufacturing; it can be easily automated; simple or even no assembly work; functionally integrated components can be produced directly; less production steps; can be connected to virtual and digital technologies;

The limitations of 3D printing are:

- in term of economics;
securities on intellectual properties such as patent and copyright have to be invested; higher capital cost for mass-production; decrease in jobs due to automation;
- in terms of technology;
limited options for materials, surface finishes and even colours; concern on precision and stability; lesser unified guidelines and global standards; it contains high risk in product launching.

Figure 2.10 summarises the principles and processes of 3D printing. According to Junji and Sandström (2013), the operation of 3D printing process comprises of the following key principles, which are:

1. Modelling

Modelling represents the virtualization of the structure of desired product. 3D models are commonly created by using CAD software; for example, Solidworks and AutoCAD. Also, with aid of 3D scanner or a digital camera, the digital data of the external features of a 3D object in reality can be traced, collected, and input into the computer as a CAD file based on it. The digital model is normally saved as stereolithography file format (STL) which stores information regarding to triangulations of the CAD model surfaces for additive manufacturing. Occasionally, the other accepted format for 3D printers such as THING and Additive Manufacturing File (AMF) format are applied.

2. Printing

STL format is considered as “repair” because the process of STL generation fixes the errors (holes; self-intersections; faces normal; manifold errors; and noise shells) which are produced by majority of the CAD software and these errors will cease the printing process. After that, “slicer” is required to process

the STL file. In fact, “slicer” is a software that translates the 3D model into a succession of thin layers and it subsequently generates a tailored G-code file for certain 3D printing devices in order to instruct and guide the printing process. Generally, dots per inch (dpi) and micrometres are used to define the X–Y resolution and the layer thickness in terms of printer resolution. 3D printed objects are typically printed layer by layer with approximately 100 micrometres or 250 dpi of thickness in layers. According to studies, some advanced devices are able to print layers up to 16 micrometres of thickness each. The finer the layer, the finer the object printed. Therefore, due to minute thickness, hours or even days are required to be spent for simply the construction of a 3D model.

3. Finishing

As mentioned previously in the limitations of 3D printing, surface finishing is one of the drawbacks of AM. One of the methods to reduce the effect of this drawback is to print object slightly oversized and followed by a precise subtractive manufacturing. The surface finish of some 3D printed polymer products; for instance, acrylonitrile butadiene styrene (ABS), can be enhanced through chemical vapor processes. Additionally, internal supports for features that are hanging or extending outwards from the body are needed to be constructed to avoid collapsing. These momentary supports have to be removed; either mechanically or chemically by dissolving. In actuality, there are already AM techniques that enable multiple materials and multiple colours to be printed simultaneously.

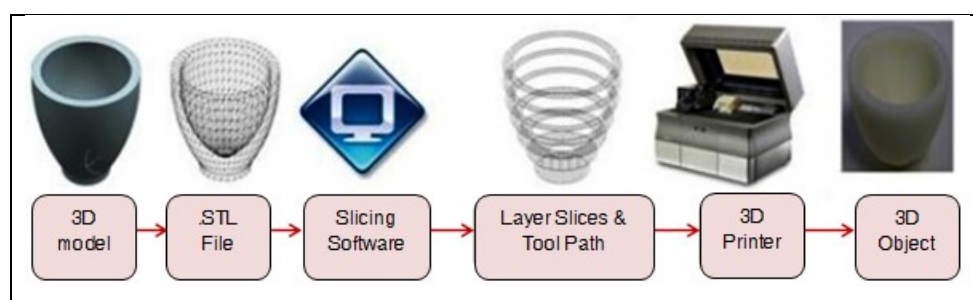


Figure 2.10: Processes and Principles of 3D Printing (Jasveer and Jianbin, 2018).

As mentioned previously that AM is widely applied in the industries. The increasing demand will definitely support this emerging technology and

eventually turns into run-of-the-mill. Wong and Hernandez (2012) expressed that AM does contribute a lot in lightweight manufacturing which is immensely crucial in aerospace and automotive industries. The main reason for the statement previously is the possibility to construct complex and intricate internal or cross-sectional shape such as honeycomb cells that give rise to the strength to weight ratio (lighter but stronger product). Moreover, architectural modelling to be eased with 3D printing. Traditionally, architects have to construct their model with their bare hands, slowly and carefully. This powerful technology together with CAD is going to bring a lot of impacts to the architectural industry as concept realization will be rapid and efficient. Same goes to rapid prototyping where research processes in any field can be speeded up in a high degree. Also, this technology breakthrough has drawn major positive outcome in the medical applications. Yan, et al. (2018) opined that the incorporation between AM and imaging technology such as computed tomography has the ability in achieving rapid production of custom-made scaffolds, creation of organ model, and direct amendment onto fracture or defect part. With the rapid maturation of AM technology, various complicated medical equipment, medical implants as well as cell printing can be easily gained by printing. Fuel cell is the next field to be benefited from the AM technology due to its potential in manufacturing precise and thin film; for instances, deposition of thin platinum film in the production of polymer electrolyte membrane fuel cell (PEMFCs) by using AM (Wong and Hernandez, 2012).

2.4.1 Types of 3D Printing

It has been decades since the first 3D printing idea has been introduced; hence, it is not uncommon to have various types of AM processes emerging in the market. Analysis shows that the standard of AM process categorizations are mainly on three parts: liquid-based, powder-based, and solid-based (Wong and Hernandez, 2012). These processes comprise FDM, SL, and Polyjet for liquid-based processes; laminated object manufacturing (LOM) for solid-based processes; selective laser sintering (SLS), electron beam melting (EBM), laminated engineering net shaping (LENS), 3D printing (3DP), and Prometal for powder-based processes. Figure 2.11 clearly categorizes the AM processes mentioned. Chen, et al. (2019) has done review on ceramic 3D printing and has

listed out ten types of AM processes in ceramics, which are SL, LOM, SLS, 3DP, FDM, IJP, DLP, two-photon polymerisation (TPP), direct ink writing (DIW), and selective laser melting (SLM). Some of the AM methods are discussed in the following subtopic.

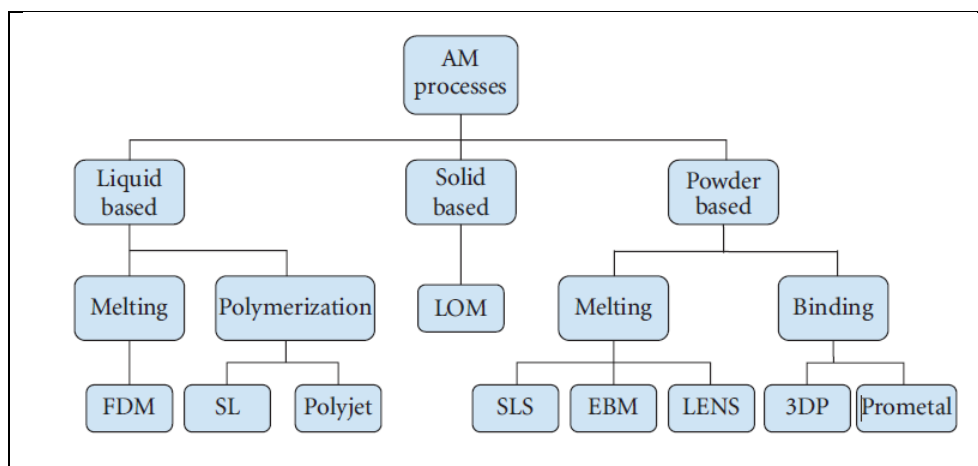


Figure 2.11: AM Processes (Wong and Hernandez, 2012).

2.4.1.1 Fused Deposition Modelling (FDM)

Fused deposition modelling is one of the most typical 3D printers utilized and it shall be the centre of attention in this study as there are no research done on alumina 3D printing in FDM. Singh and Garg (2016) did a study on FDM and expressed that FDM printing method can be defined as feeding feedstock materials into the device nozzle or extrusion head in which heat is applied to achieve semi-liquid state in the feedstock materials; then the nozzle extrudes the materials followed by depositing and constructing the desired structure on the platform layer by layer. The extrusion can be plunger-based, filament-based, and screw-based as depicted in Figure 2.13. Figure 2.12 portrays the schematic diagram of FDM device.

Implementation of ceramic materials in the FDM process will differ from the conventional plastic applications. Typically, the materials applied in FDM are plastics such as polycarbonate (PC), polyphenylsulfone (PPSF), and ABS due to low glass transition temperature (147 °C, 100 °C, and 105 °C respectively) that support the processes; However, in this study, alumina – CA

slurry will be used as the feedstock materials which is contrary to conventional application that uses wind-able and flexible wires. For ceramic 3D printing in FDM, the printed part has to undergo debinding and sintering process to attain desired densification which is opposed to polymer 3D printing that the printed product will be hardened right after printing with no post-processing needed. Ceramic particle distribution, size, and dispersity; the binder and additives ratio implemented; and the viscosity of the slurry are the challenges aroused when applying ceramic materials in FDM process. Generally, the viscosity of the slurry falls between 10 to 100 Pa s, the dispersity of the ceramic particles should be even, and the flow should be stable and constant in order to smoothen the extrusion process in FDM process (Chen, et al., 2019). Another characteristic for FDM is that the product has to solidified immediately to prevent sagging and to support to printed part. Vacuum degassing or centrifugation can be implemented to diminish the entrapment of air in the samples. Furthermore, rapid solidification can prevent collapsing of the sample without support. The major advantages of FDM method are the low process cost and the inexpensive device. The main problem of all FDM processes is the staircase effect and rough surface finishing which depend greatly on the size and resolution of the extruded parts. In order to minimize the effect of this concern, resolution on the z-axis has to be small at about 0.25 mm; nevertheless, longer time up to days is required in constructing the ceramic product through FDM. Agarwala, et al. (1996) had conducted an FDM ceramic printing investigation and he has successfully eliminated defect on the printed structure such as sub-perimeter void, core void, and inter-road defect by modifying the printing path. By eliminating defects, the relative density of sintered ceramic product has increased by 3% from 95% to 98%. With 45 vol% of binder, Agarwala, et al. (1996) achieved a 98 % relative density of GS-44 silicon nitride sample through FDM method.

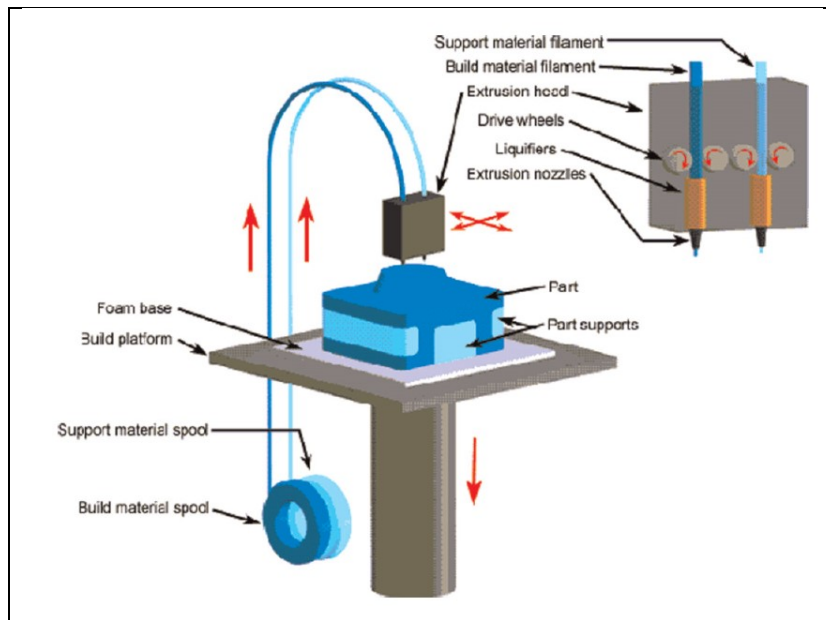


Figure 2.12: FDM Schematic Diagram (Singh and Garg, 2016).

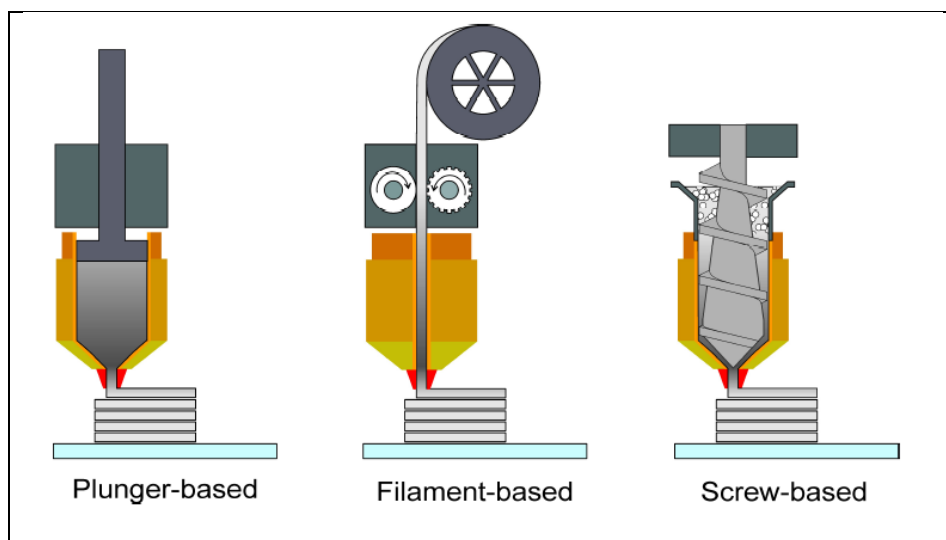


Figure 2.13: Types of Extrusion in AM (Gonzalez-Gutierrez, et al., 2018).

2.4.1.2 Stereolithography (SL)

SL is a common method utilized in AM and it is considered the first process invented in AM. The working principle for SL is applying ultraviolet (UV) laser onto a tank of resin to construct parts (Jasveer and Jianbin, 2018). The UV beam is directed onto the liquid polymer in the vat with desired design. When the liquid polymer is subject to the UV laser, the atoms of the photopolymer link

together, harden and form solids. Layer by layer, the whole product is constructed. Post processing is needed to enhance the properties of the product. The advantages of SL are the solid can be formed very precisely at a resolution up to microscale with a smooth surface in a less time-consuming way.

SL can be applied in ceramic forming process too. Instead of utilizing a vat of liquid polymer, a tank of well-dispersed ceramic suspensions (with aid of additives) is prepared for ceramic SL process. Correspondingly, the UV light shines on the liquid and polymerization only takes place in organic monomer due to inertness of ceramic particles towards light irradiation. The crosslinked organic polymer networks grip the ceramic particles into desired shape. The product formed is called *green* and post treatments such as sintering and binder removal are required to be done in order to obtain a better physical and mechanical properties of the product. Zhang, Sha and Zhao (2016) have conducted an investigation on the SL printed alumina which alumina slurry with 45 vol%, viscosity less than 2 Pa s at 30 s⁻¹ shear rate attains the final product with 96.5% relative density after sintering. On the other hand, Zhou, et al., (2016) utilized alumina suspension with with acrylamide and methylene-bis-acrylamide and they produced a sintered alumina product with 99.3 % of relative density and 17.5 GPa of Vickers hardness are achieved through SL method and the properties are close to the properties of conventional manufactured alumina.

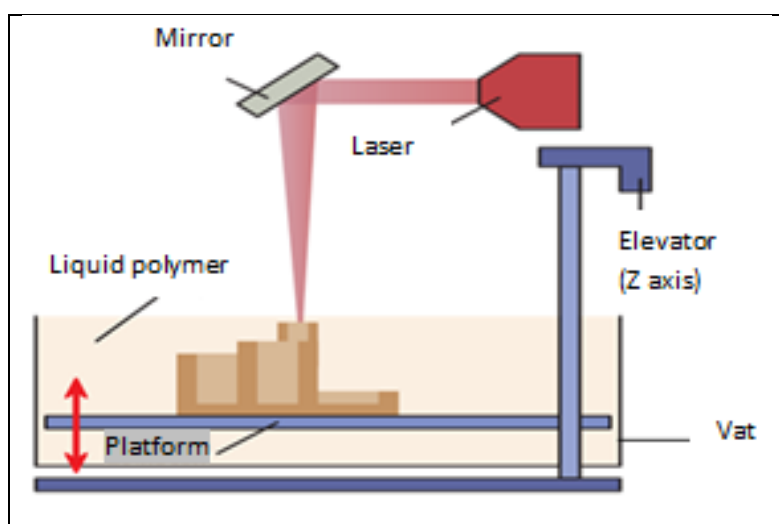


Figure 2.14: SL Process Schematic Diagram (Jasveer and Jianbin, 2018).

2.4.1.3 Digital Light Processing (DLP)

DLP method is similar to SL method; as a substitute of using UV laser source, DLP process applies conventional light source in treating the photosensitive polymer resin. From Figure 2.15, it can be understood that light source is projected and focused towards the photopolymer. The photosensitive gum is hardened and form a layer of solid shaped based on the design. It is followed by lowering of platform to set stage for the subsequent layer to be constructed by light source. This repeated process will eventually form a 3D product. The advantages of DLP are similar to the advantages of SL but with a shorter processing time. The working principle in ceramics for DLP process is parallel to the SL process.

Due to the remarkable advantages on DLP process, studies have been made on DLP process in manufacturing ceramic products. Hatzenbichler, et al. (2012) had fabricated an alumina product through DLP method from slurry with solid loading between 45 – 50 vol% and the result is satisfying – final alumina product with 99.6 % relative density to theoretical value with 510 MPa of biaxial strength. Varghese, et al., (2017) had studied on fabrication of alumina *green* with 25 – 60 wt% from photosensitive resin of mixed polyethylene glycol diacrylate with ethanol-dissolving-photoinitiator through DLP and concluded that 60 wt% of ceramic loading is the saturation point where ceramic loading beyond this point will cause loosely adhered powder.

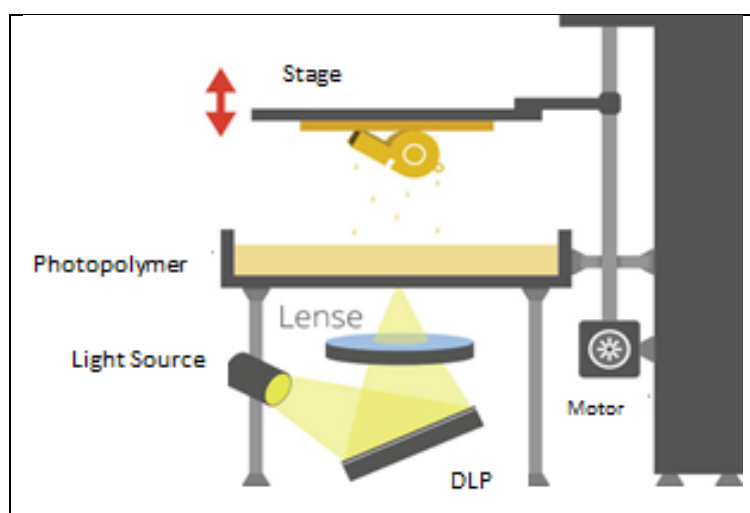


Figure 2.15: DLP Process Schematic Diagram (Jasveer and Jianbin, 2018).

2.4.1.4 Inkjet Printing (IJP) and Binder Jetting Printing (BJP)

IJP is the next popular method in AM. Initially, the IJP technique is being explained as discharging liquid such as ink in the form of droplet onto paper or other substrate through the nozzles and it is normally creating two-dimensional structures. Recently, due to rapid progress in the IJP development, this method has the ability to create 3D multi-layered ceramic structure by substituting the liquid with well-dispersed ceramic material in liquid solvents. In BJT, binder droplets are selectively deposited from the nozzle onto powder-bed filled with ceramic particles. The benefits of this technique are the inexpensive and simple processes; and wide variety of applicable materials. The main limitation of this technique is the inflexibility in complex structure printing due to inability to construct overhanging and hollow structures.

Peng, et al. (2018) have researched on printing alumina through IJP process and resulted into IJP printed alumina product with 3.73 g/cm^3 ($\sim 95\%$ relative density) and 10.80% of porosity after sintering at $1550 \text{ }^\circ\text{C}$. Moreover, Huang, et al. (2019) utilized the different zirconium basic carbonate (ZBC) contents in inorganic binder in BJT and had proven that when ZBC increase from 0 – 35 wt%, the alumina *green* relative density has an 27 % rise to 51 %.

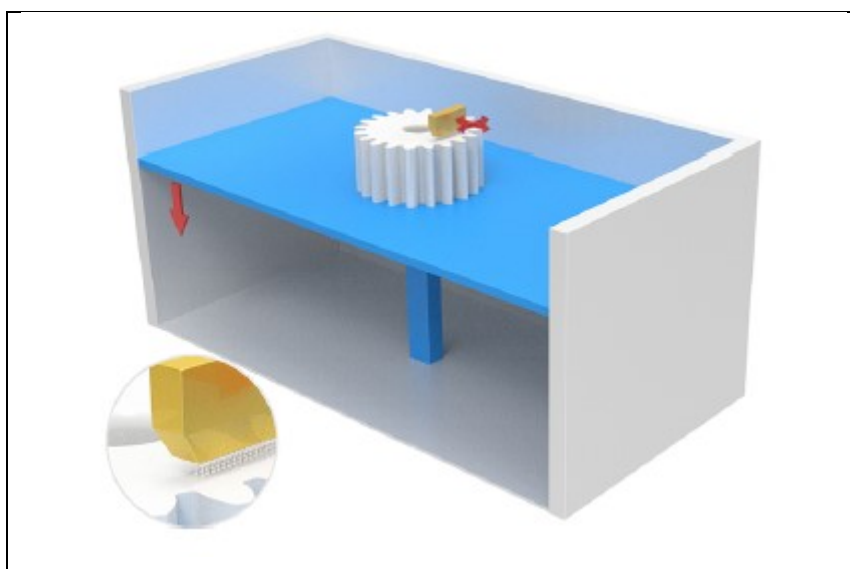


Figure 2.16: IJP Schematic Diagram (Chen, et al., 2019).

2.5 Cellulose Acetate (CA)

CA is an essential ester of cellulose and it is conventionally produced through acetylation or esterification of cellulose. Generally, the main source of cellulose is wood pulp and cotton linter. This biopolymer is important due to its vast applications in fabrics, separation technology, magnetic tapes, films, eyeglass frames, cigarette filters, moulded plastics, and medical field due to its remarkable properties and renewable features (Egot and Alguno, 2018). Benefits of using CA are: decent solubility in various solvents; its molecular weight; and its melting properties (Puls, Wilson and Hölter, 2011). Also, CA remains solid at room temperatures and this could draw long period constant viscose properties. This substance gains more attention from the industries due to its renewability and biodegradability that provide less harm to the earth.

The most common degree of substitution (DS) found in CA is between 2 (cellulose diacetate) – 2.5. Due to abundance of cellulose diacetate, cellulose “acetate” normally refers to “diacetate” (Fischer, et al., 2008). Figure 2.17 demonstrates the chemical formula for CA.

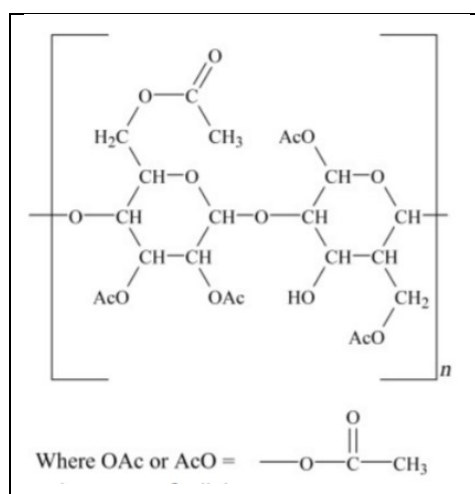


Figure 2.17: Structural Formula of CA (McKeen, 2019).

The properties of CA will be discussed as follows:

- Solubility

CA can be dissolved in various organic solvents and it is contingent on its DS. Figure 2.18 shows the comparison in solubility of CA in various kinds of organic solvents which are acetone, methyl acetate, ethyl acetate, nitromethane,

nitromethane-ethanol 8:2, ethyl acetate, diacetone alcohol, methylene chloride, methylene chloride methanol 9:1, and formic acid. In Figure 2.18, the acetic acid % has replaced the DS. Table 2.5 represents the relationship between the DS and acetyl as well as acetic acid content. Equation 2.1 defines the formula between the DS and the acetyl content. According to figure 2.18, methylene chloride methanol 9:1 and formic acid are the best solvents to dissolve all CA at any acetic acid. Commonly, acetone which is another decent organic solvent is utilized to dissolve CA (up to cellulose diacetate). Figure 2.18 also proves that ethyl acetate can only dissolve CA with acetic acid of approximately 55 %.

$$DS = \frac{Mw_C \times \%_{Acetyl}}{(Mw_A \times 100) - [(Mw_A - 1) \times \%_{Acetyl}]} \quad (2.1)$$

Where

DS = degree of substitution

Mw_C = cellulose monomer molecular weight = 162

Mw_A = acetyl group molecular weight = 43

$\%_{Acetyl}$ = acetyl content in wt%

Table 2.5: CA's Acetyl and Acetic Acid Content in Different DS (Bao, 2015).

Compound	DS	Acetyl Content (%)	Acetic Acid Content (%)
Cellulose	0	0.0	0.0
Cellulose Monoacetate	1	21.1	29.4
Cellulose Diacetate	2	34.9	48.8
Cellulose Triacetate	3	44.8	62.5

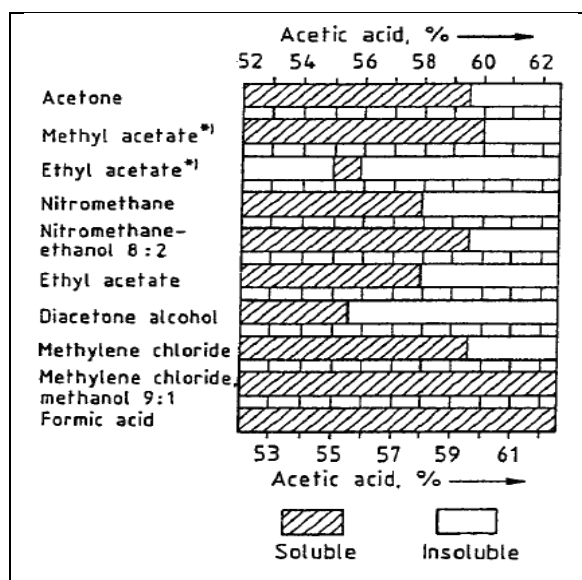


Figure 2.18: Solubility of CA in Different Organic Solvents (Bao, 2015).

- Thermal properties

Figure 2.19 describes the thermogram and behaviour of CA with different degrees of substitution at different temperature. The interference between the glass transition temperature T_g and the decomposition temperature T_d at 1.7 DS denotes that from this point onward, the CA will not decompose before achieving T_g and it starts to be measurable by conventional methods. The next interference occurs between the melting point T_m and T_d at approximately 2.5 DS. This is the only DS where T_m is slightly lower than T_d . At this point, CA is allowed to be transformed via processes and techniques that includes melting. Indisputably, this is the reason DS 2.5 or 2.46 (to be exact) of CA can be commercially found and, in this investigation, DS 2.46 is going to be utilized due to this special feature. Based on Figure 2.20, 463 K or 190 °C is the glass transition point for DS 2.5 CA while the T_m and T_d are identified at the following peaks at around 520 K. Figure 2.21 signifies the relationship between T_d of CA DS 2.46 against weight average molecular weight, M_w . The process for Figure 2.21 is conducted on a Shimadzu TGA-30 M from Kyoto with continuous nitrogen gas, N_2 supply at a rate of 50 cm^3/min and 10 °C/min heating-up. Figure 2.21 also has shown that a linear increase in T_d with rising M_w where $\frac{\partial T_d}{\partial M_w} = 8 \times 10^{-5} K$. These statements mentioned have clearly denoting that the T_g , T_d , and T_m are highly dependable on DS and another factor like M_w .

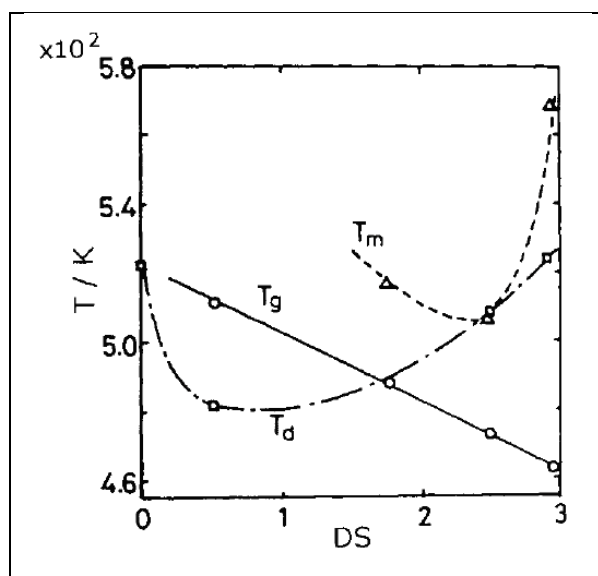


Figure 2.19: Graph of relationship between melting temperature T_m , glass transition temperature T_g , and decomposition temperature T_d with various degrees of substitution of CA (Bao, 2015).

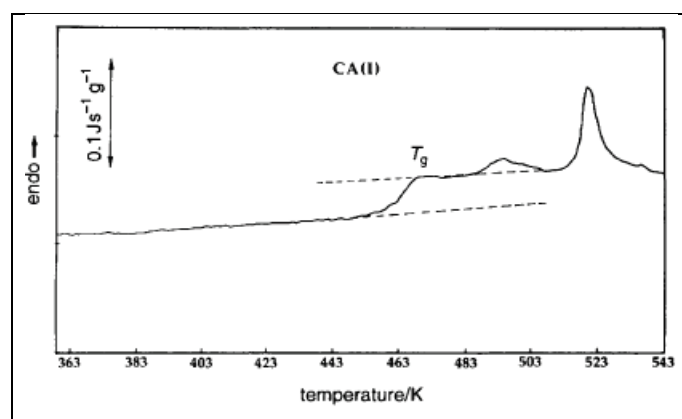


Figure 2.20: Thermogram of DS 2.5 CA (Bao, 2015).

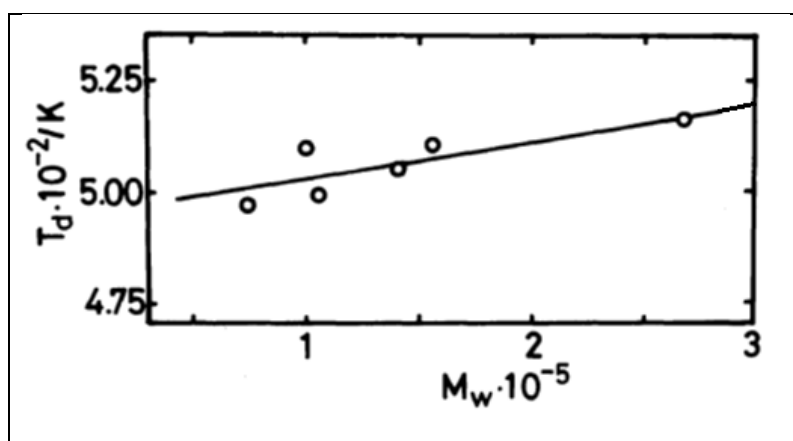
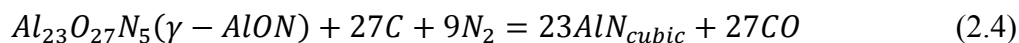
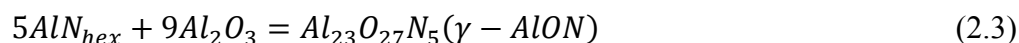


Figure 2.21: Graph of T_d of CA DS 2.46 against M_w which determined by Thermogravimetry (TG) Analysis (Kamide and Saito, 1985).

2.6 Binder Removal

Binder, as mentioned before, serves a purpose of providing gluing effects on the particles of *green* body so that the *green* body has a sufficient strength to maintain the shape. Generally, high-polymeric components; for examples, polysaccharides and cellulose (in this case); are utilized as plasticisation or binding agents. The presence of binders allows smooth flow of extrusion process, which is crucial in FDM printer.

Binder removal is also known as debinding process and it defined as removing the binder from the *green*. It is an essential process before the sintering process (will be explained later in Chapter 2.4.3). Figure 2.22 depicts the debinding model. Becker and Gmbh (2006) stated that organic polymeric binders have to be decomposed entirely from the *green* due to the influence of carbon delays on sintering process and this will eventually lower the quality of end product. Michálek, et al. (2017) have provided an important insight that the carbothermal reductions shown in equation 2.2, 2.3, and 2.4 will take place. Also, diffusion of carbon into α -alumina can occur at high temperature from 570 °C onwards.



Also, time is intensive in binder removal process as the binder decomposition speed could not overtake the transport speed of product pyrolysis. Destruction of the *green* body will take place when there is an excess pressure of the gaseous pyrolysis products.

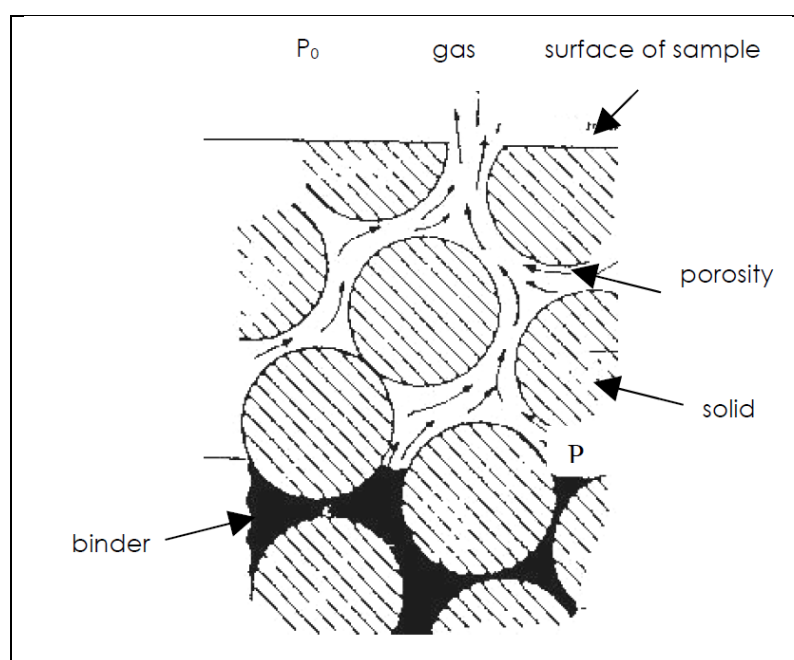


Figure 2.22: Binder Removal Model (Becker and Gmbh, 2006).

Binder can be pyrolyzed thermally. TG is one of the thermal analysis methods that records the changes in mass of a component which is generally exposing to a linear heating-up. Figure 2.21 shows an example of TG analysis. The temperatures in decomposing organic binders are normally ranging from 150 °C to 600 °C. Table 2.6 lists out various organic binders and their maximum decomposition temperature. Figure 2.23 shows another piece of investigation on the TG analysis of decomposition of CA from Trivedi, et al. (2015) by

utilizing a Mettler Toledo, differential thermal analysis, and TG analyser with constant heating of 5 °C/min from room temperature until 400 °C and oxygen supply. According to their investigation, 24.99 % of CA weight loss occurs from 230 °C to 290 °C in the first thermal degradation and another 68.08 % occurs in the second degradation from 310 °C to 370 °C. The maximum pyrolysis of CA falls at 351 °C according to Trivedi et al. (2015). According to Becker and Gmbh (2006), alumina can act as a catalyst and draw impact on polymer pyrolysis; for example, the presence of alumina might assists in decomposition of polymers (PEG) and henceforth bring the maximum decomposition temperature down as shown in Figure 2.24.

Table 2.6: Organic Binders and Their Maximum Decomposition Temperature.

Organic Binders	Temperature of Maximum Decomposition (°C)	Reference
PVA	200 – 300	(Becker and Gmbh, 2006)
PEG	150 – 250	(Becker and Gmbh, 2006)
PAA	250 – 350	(Becker and Gmbh, 2006)
CA	224 – 243 (Initiate decomposition) 351	(Kamide and Saito, 1985) (Trivedi, et al., 2015)

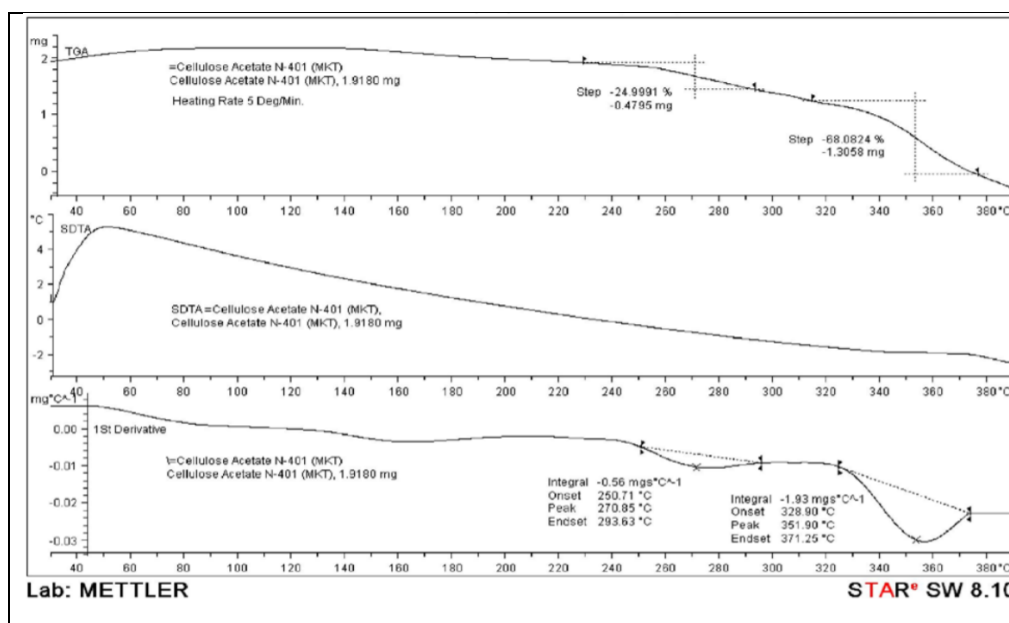


Figure 2.23: CA TG Analysis Thermogram (Trivedi, et al., 2015).

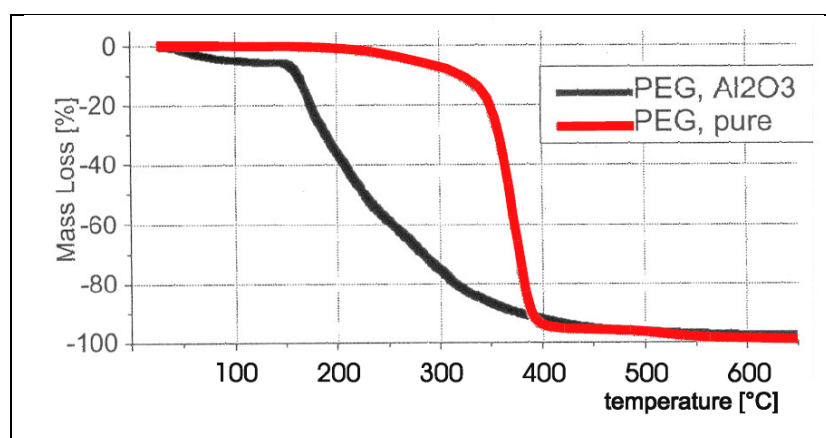


Figure 2.24: PEG Decomposition With and Without Alumina (Becker and Gmbh, 2006).

2.7 Sintering

Sintering is a technique utilized to generate materials and components mainly from ceramic or metal powder with controlled density through thermal energy (Kang, 2005). Ceramic product before the process of sintering are called *green body*. Green bodies are fragile and having weak bonding between particles. Thus, it can be said that sintering is the process which links the particles together and strengthens their bonding without reaching the melting point of the components or materials. Sintering is normally treated on materials or components after shaping and forming process to maintain the product shape. When powder compact is subject to a certain thermal energy, two basic

phenomena: densification and increment in the average grain size; will take place in the compact as shown in Figure 2.25. An effective sintering process can greatly decrease the porosity and boost the properties for example strength.

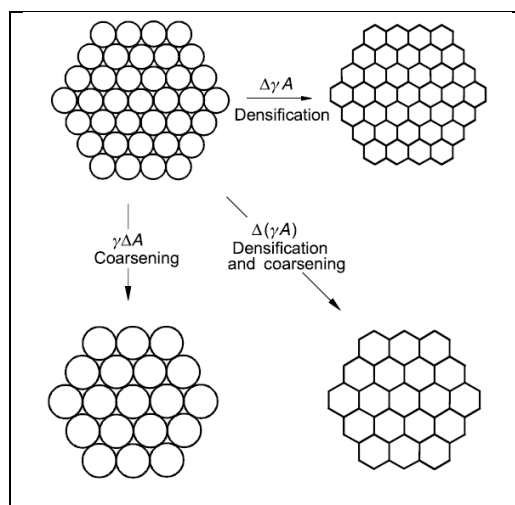


Figure 2.25: Effect of Sintering (Kang, 2005).

Pulgarín and Albano (2015) have conducted analyses on the effect of sintering on alumina and other composites at different temperature range from 1100 °C to 1600 °C (heating rate of 5 °C/min and 2 hours for every sample). Figure 2.26 shows the curves of relative sintered of samples density against sintering temperature. According to Figure 2.26, the relative density rises along with the temperature with relative density more than 95 % and starts to decline slightly at 1600 °C. Figure 2.27 depicts the graph of mean grain size of alumina and other samples against sintering temperature. It is obvious in the graph showing that sintering leads to great escalation in the grain growth. Figure 2.28 has illustrated the microstructure and the grain size of the sintered alumina.

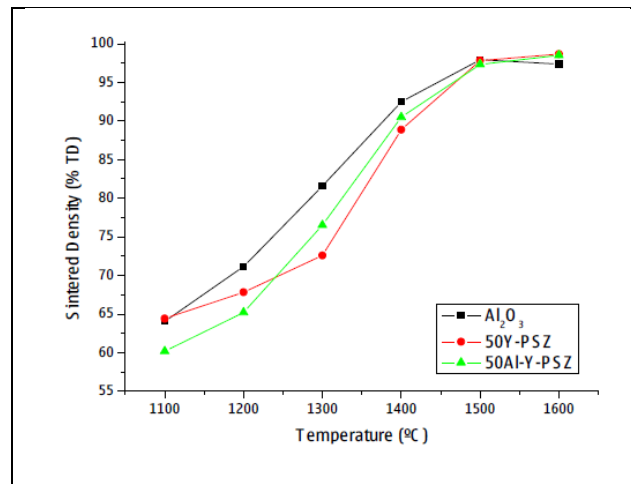


Figure 2.26: Graphs of Relative Sintered Density against Sintering Temperature (Pulgarín and Albano, 2015).

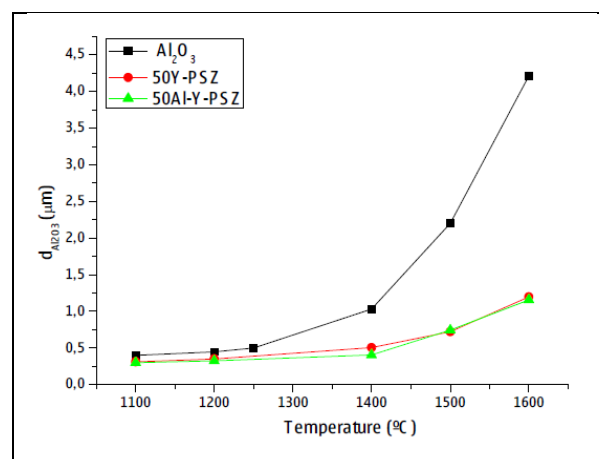


Figure 2.27: Graphs of Mean Grain Size against Sintering Temperature (Pulgarín and Albano, 2015).

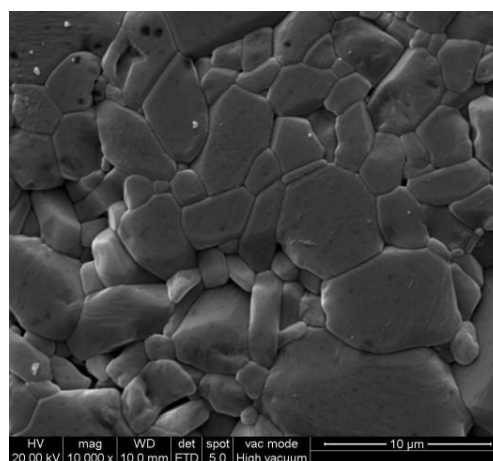


Figure 2.28: SEM Image on Sintered Alumina at 1600 °C (Pulgarín and Albano, 2015).

Roy, et al. (1993) did investigations on effect of sintering on alumina too. They stated that alumina samples are going to be densified through sintering temperature up to 1600 °C and beyond this point, the samples will start to “dedensify” or become less dense which is not desirable. This statement is supported by Figure 2.29 and the highest relative density of 98.9 % in this case is attained by sintering at 1600 °C for 1 hour. However, sintering at 1650 °C for 3 hours and sintering at 1600 °C for longer period of 5 hours will result into lower relative density which is 98.5 % and 98.7 % respectively. For pressureless alumina sintering, 1600 °C for 1 hour is the best case; best sintering parameter for alumina in overall based on Table 2.7 is hot-pressing of 1600 °C with 50 MPa for 1 hour. Table 2.7 shows the sintering result by Roy, et al. (1993) where sample 1 to 7 are pressureless sintered and sample 8 to 11 are hot-pressed sintered.

Table 2.7: Alumina Sintering Result (Roy, et al., 1993).

Samples	Time (hr)	Temperature (°C)	Pressure (MPa)	Relative Density (%)	Grain Elongation Percentage
1	1	1500	–	96.3	11
2	5	1500	–	98.1	14
3	3	1550	–	98.7	14
4	1	1600	–	98.9	15
5	5	1600	–	98.7	24
6	3	1650	–	98.5	25
7	3	1400	–	93.4	–
8	1/6	1450	50	99.4	16
9	1	1450	10	99.3	14
10	1/6	1600	10	98.9	22
11	1	1600	50	99.5	25

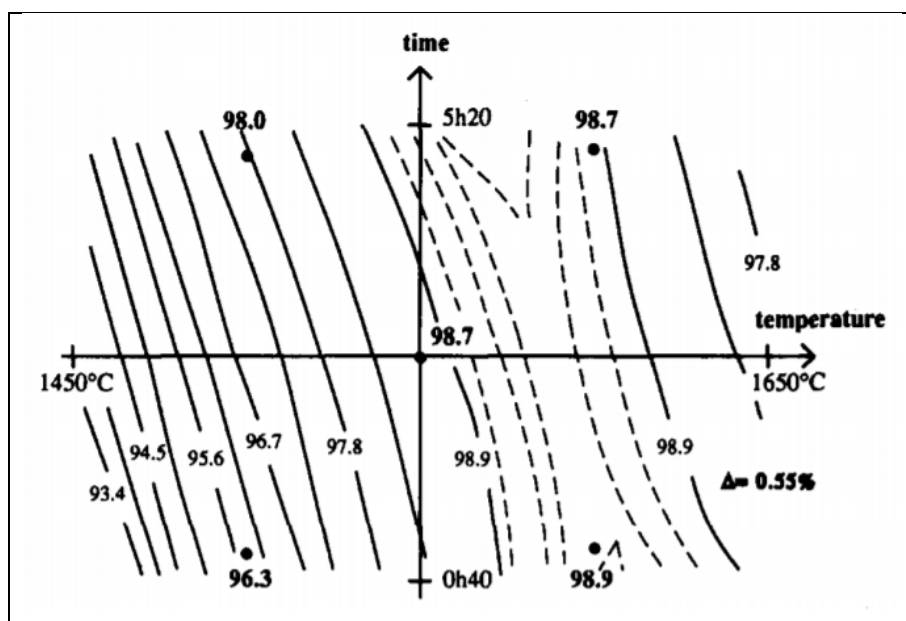


Figure 2.29: Isodensity Curves of Alumina under Pressureless Sintering (Roy, et al., 1993).

2.7.1 Sintering Behaviour of TiO₂-Doped Alumina

According to Chapter 2.6, the best case for pressureless alumina sintering is at 1600 °C for 1 hour. To attain temperature of 1600 °C, it requires high-temperature furnace which is more expensive and this furnace might not be available in some of the research institutes. Therefore, the sintering temperature of alumina has to be reduced.

Ting, et al. (2008) had undergone a research in order to reduce sintering temperature whilst maintaining the properties of the final product. They stated this situation could be succeeded by doping TiO₂ into the alumina. Table 2.8 depicts the relative bulk density of alumina product with increasing weightage of TiO₂. Figure 2.30 and 2.31 describe how sintering temperature and TiO₂ addition affect the Vickers hardness and Young's modulus of alumina ceramics.

Table 2.8: Relative bulk density of alumina product with increasing weightage of TiO₂ (Ting, et al., 2008).

Sintering Temperature (°C)	Weightage of TiO ₂ (wt%)				
	0	0.5	1.0	2.0	5.0
1400	61.4	81.1	97.1	97.4	96.5
1450	86.8	97.8	97.8	97.2	96.7
1600	97.8	-	-	-	-

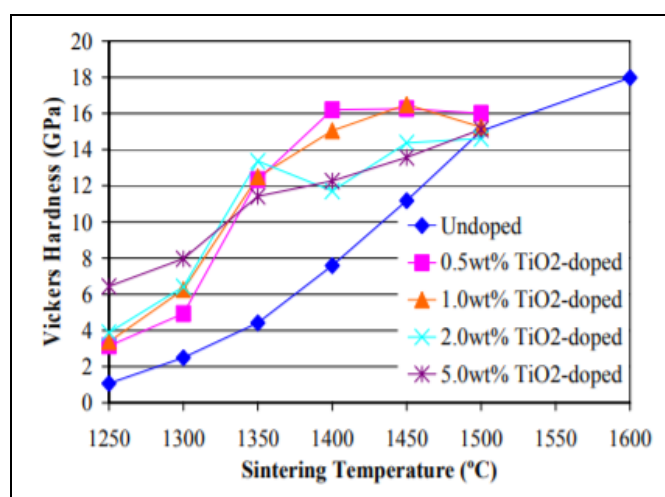


Figure 2.30: The relationship between TiO₂ addition, sintering temperature, and Vickers hardness on alumina (Ting, et al., 2008).

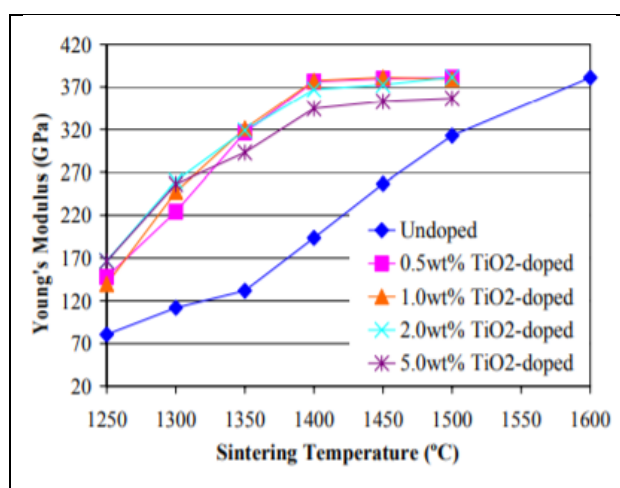


Figure 2.31: The relationship between TiO₂ addition, sintering temperature, and Young's modulus on alumina (Ting, et al., 2008).

According to Ting, et al. (2008), the best composition of TiO₂-doped alumina that draws the most advantages is 1 wt% of TiO₂ by sintering at 1450 °C. Based on Table 2.8, Figure 2.30, and Figure 2.31, the relative bulk density of this composition is the highest at 97.8 %; the Vickers hardness of this composition is attained at 16.49 GPa; and the Young's modulus of this composition is as high as 16.49 GPa.

To conclude this section, it can be said that the sintering temperature can be reduced to 1450 °C from 1600 °C whilst maintaining the final properties of alumina ceramics by doping 1.0 wt% of TiO₂.

2.8 Ceramography

Ceramography brings up the meaning of the science and art of preparation, investigation, and evaluation of microstructures on ceramic materials; or it could be simplified as metallography of ceramics (Chinn, 1998). By applying ceramography onto the ceramic samples, it enables the observers to study the microstructures including grain sizes, grain boundaries, pores, and microcracks. These investigations on microstructure could allow the observers to understand better on the mechanical, electrical, thermal, and other properties of the ceramic samples.

Etching is defined by the process that removes the deformed thin layer produced by grinding and polishing. Generally, etching is utilized to reveal the microstructures. Ceramographic etching can be distinguished into 3 main parts; the optical etching, electrochemical etching, and physical etching. The review on ceramographic etching is shown in Figure 2.32.

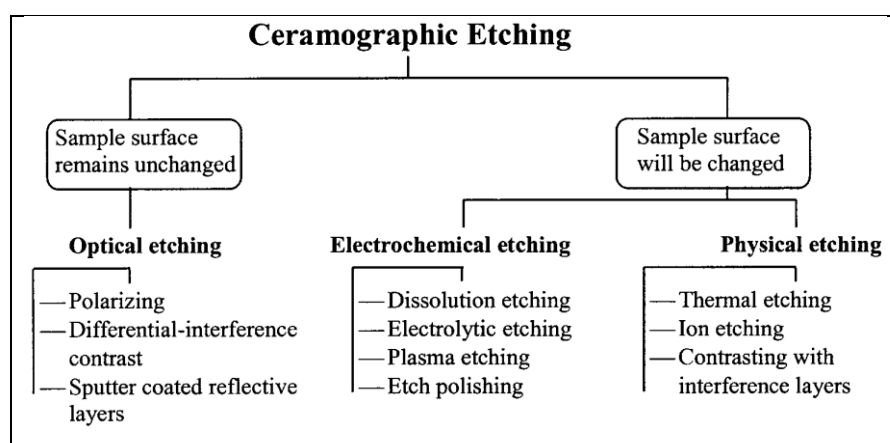


Figure 2.32: Ceramographic etching methods (Taffner, et al., 2004).

2.8.1 Thermal etching

As contrast to metal, chemical inertness is one of the outstanding features of ceramics that allow them to withstand in corrosive environment. Thus, chemical etching is effective in metal but not in ceramics. Therefore, Taffner, et al. (2004) expressed that thermal etching is one of the ways to reveal the microstructure of ceramics mainly the alumina and zirconia; However, the temperature and time of the heat treatment have to be carefully designated so that it will not affect the microstructure of the samples. Typically, the thermal etching temperature should be around 100 °C to 150 °C beneath the sintering temperature of the samples and the time of heating should be approximately 15 minutes to 30 minutes (Taffner, et al., 2004). Chinn (1998) etched the alumina samples thermally at 1500 °C and held for 20 to 30 minutes and his SEM image of his samples is illustrated in Figure 2.33. Figure 2.34 shows the SEM image of thermally etched alumina sintered at 1400 °C. Grain growth, degradation of the desired features, and enhancement of scratches could occur if the temperature is too near to or over the sintering temperature and it is left heating for too long. This is called over-etching (Chinn, 1998).

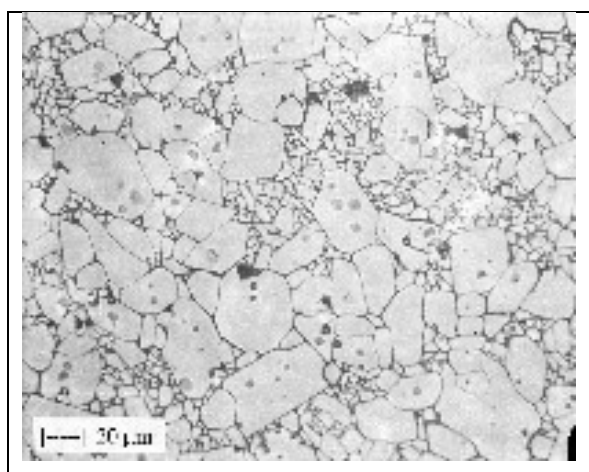


Figure 2.33: Microstructure of thermally etched and cold isostatically pressed alumina (Chinn,1998).

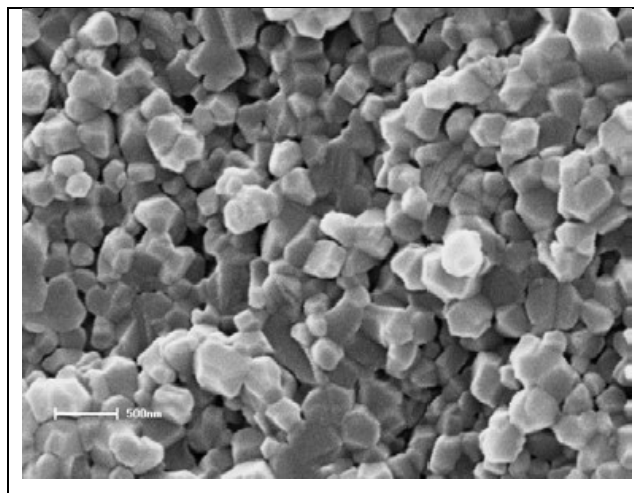


Figure 2.34: SEM image of thermally etched alumina sintered at 1400 °C (Chinelatto, et al., 2012).

2.9 X-Ray Diffraction of Alumina, CA, and TiO₂

The basic working principle of XRD is by emitting x-ray into the samples and to study the XRD pattern formed by data collected from the intensity and the angle of the diffracted ray of the sample. Every material has distinct XRD pattern and thus his distinctive property allows the researchers to determine the types of materials presented in the samples. In the development of alumina-based feedstock for FDM printer, alumina, CA, and TiO₂ are utilized as raw materials. Therefore, the composition of the final products could be determined through XRD pattern for further studies.

Barma and Mandal (2014) has determined the XRD pattern of pure α -alumina powder which is shown in Figure 2.35. the XRD pattern of alumina powder peaks at around 26°, 35°, 38° between 20° to 50° (focused range of angle). Kamal, et al. (2018) has found out the XRD pattern for pure CA and chitosan as illustrated in Figure 2.36. The XRD pattern of CA peaks at around 20 ° and its intensities drops until 200 count/sec at 50 °. Furthermore, Figure 2.37 shows the TiO₂ XRD pattern which is found by Thievasanthi and Alagar (2013). It could be seen that in the range of 20° to 50°, TiO₂ peaks at 25°, 38°, and 47°. Other than 47 °, the peaks of alumina are similar to TiO₂ within the stipulated range.

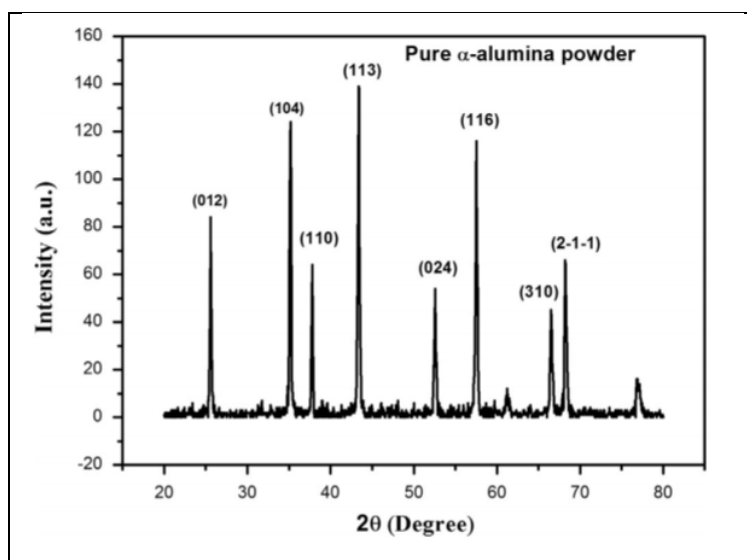


Figure 2.35: XRD Pattern of Pure α -Alumina Powder (Barma and Mandal, 2014).

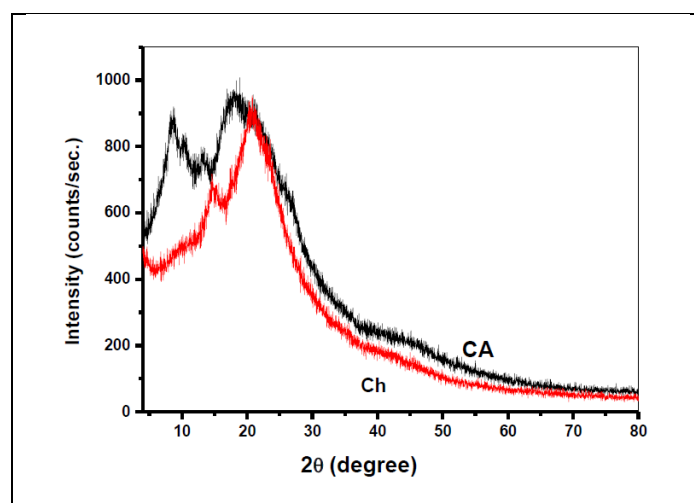


Figure 2.36: XRD Pattern of Pure CA and Chitosan (Kamal, et al., 2018).

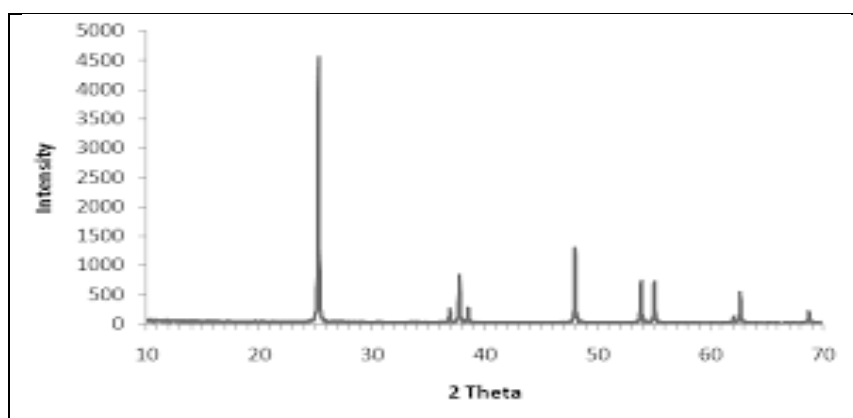


Figure 2.37: XRD Pattern of TiO_2 (Theivasanthi and Alagar, 2013).

2.10 Summary

This literature review has shown profound apprehension on properties of ceramics and alumina; various kinds of ceramic and alumina conventional forming processes; AM and types of 3D printing containing FDM, SL, DLP, IJP, and BJP; effect of particle size; CA and its solubility and thermal properties; binder removal with CA thermal decomposition properties; sintering on alumina; sintering behaviour of TiO₂-doped alumina; and the XRD of alumina, CA, and TiO₂. Undoubtedly, these understandings are going to aid greatly in the experimental process.

CHAPTER 3

METHODOLOGY AND WORK PLAN

3.1 Introduction

In this chapter, detailed and comprehensive methodology and work plan in order to study the physical and mechanical properties of FDM-3D-printed alumina are listed and discussed.

3.1.1 Raw Materials

Alumina powder (Spray dried grade; Al₂O₃ 96 %; crystal size 2 μm; granulate 180 – 230 μm; density 1.25 – 1.35 g/cm³; lost of ignition (LOI) 3.8 %) was the main raw materials used as the printed ceramic core. The properties of CA (acetylcellulose) utilized in this experiment as solid-state binder is described in Table 3.1.

Table 3.1: Properties of CA from Sigma Aldrich, USA.

Properties	Explanation
Molecular weight	Average M_n (Number average molecular weight) ~ 30000 by GPC (Gel permeation chromatography)
Extent of labelling	39.8 wt% acetyl group
Impurities	≤ 3.0 % water
Density	1.3 g/mL (temperature at 25 °C)
Refractive Index	n _{20/D} 1.475

M_n is representing the average molecular weight of entire polymer chains in the sample. M_n is described as in equation 3.1.

$$M_n = \frac{\sum N_i M_i}{\sum N_i} \quad (3.1)$$

Where

M_n = Number average molecular weight

N_i = Number of chains of M_i

M_i = Chain molecular weight

M_w is the weight-average molecular weight. Equation 3.2 is defining M_w .

$$M_w = \frac{\sum N_i M_i^2}{\sum N_i M_i} \quad (3.2)$$

Where

M_n = Number average molecular weight

N_i = Number of chains of M_i

M_i = Chain molecular weight

Titanium (IV) oxide or TiO₂ (assay: $\geq 99.5\%$ trace metals basis; form: nanopowder; primary particle size: 21 nm (TEM); surface area: 35 – 65 m²/g (BET); melting point: 1850 °C; density: 4.26 g/mL at 25 °C) from Sigma Aldrich was implemented in doping into alumina.

According to technical review in 2015 by Agilent Technologies, for equal chain lengths or a monodisperse polymer, $M_w/M_n = 1$. Thus, M_w in this case was 30000 as well. By substituting 39.8 wt% acetyl that acquired from Table 3.1 into equation 2.1, it had evidently shown that the DS of acetyl cellulose used in this experiment is 2.46. Acetone, in this experiment, acted as an organic solvent to dissolve CA in order to form a solution and to blend together with alumina powder. The acetone or dimethyl ketone utilized was product from QRĕC company with molecular weight of 58.08 g/mol. The chemical formula for acetone is C₃H₆O

3.1.2 Preparation of TiO₂-doped Alumina Powder

As mentioned in Chapter 2.6.1, doping of TiO₂ in alumina contributes in lowering the sintering temperature of alumina without affecting the physical and mechanical properties of alumina so that the furnace available in the research institute can support this project. Also, it is stated in the same section where 1.0

wt% of TiO₂ is the best composition to be doped. In this experiment, wet milling was employed in the doping process.

99 wt% of alumina and 1 wt% of TiO₂ were weighed. Weighed alumina was poured into a beaker with addition of ethanol to result into slurry. The beaker was placed in a WiseClean ultrasonic cleaner filled with distilled water and 5 minutes of ultrasonication was applied to the slurry. Weighed TiO₂ was then added into the beaker. The mixture was left ultrasonicated for 30 minutes with stirring occurred every 5 minutes interval. The ultrasonication process served the purpose of inducing agitation to the liquid which will eventually generate high force to allow adherence of TiO₂ particles onto the alumina particles.

The semi-liquid suspension was subsequently transferred into a bottle with addition of zirconia balls for ball milling process. The bottle was left for rolling for one hour to complete the ball milling process and the mixture was shaken for every 10 minutes interval. Ball milling process was done to crush the particles into smaller size.

After ball milling was done, the zirconia balls were sieved and separated from the slurry. Ethanol was added to clean the zirconia balls and ensure the slurry was completely separated from the balls. The solution obtained was moved into a drying oven and was being dried at 70 °C overnight. The product was removed from the oven and sieving process was carried out to ensure the fine powder form of the product. The powder yielded was the 1 wt% TiO₂-doped alumina powder.

3.1.3 Preparation of *Green* Samples

The sample compositions were being divided into two main categories: The CA-acetone concentration and the CA-acetone volume occupation of the samples in vol%. For CA-acetone concentration, 100 g CA per litre acetone (g/L), 150 g/L, and 200 g/L were implemented. Samples with CA-acetone volume occupation of 70 vol%, 80 vol%, and 90 vol% CA-acetone were applied to the stated concentrations respectively. The details of the CA-acetone concentration and CA-acetone loading are stated clearly in Table 3.2.

After determining the concentration of CA-acetone and the volume percentage of the samples, the mass of CA and alumina as well as the volume

of acetone required were calculated as depicted in Table 3.3. The total volume for each sample was set at 10 mL.

Table 3.2: Volume Composition of TiO₂-doped Alumina Powder, CA, and Acetone for 3 Different Concentrations of Binder (Total of 9 Samples).

CA-Acetone Concentration (g/L)	CA-Acetone Volume		TiO₂-doped Alumina Volume	
	Vol%	mL	Vol%	mL
100	70	7	30	3
	80	8	20	2
	90	9	10	1
150	70	7	30	3
	80	8	20	2
	90	9	10	1
200	70	7	30	3
	80	8	20	2
	90	9	10	1

Table 3.3: Weight of CA and TiO₂-doped Alumina with Acetone Volume for Each of the Samples.

Sample Composition		CA Weight	Acetone	TiO₂-doped
CA-Acetone	CA-	(g)	Volume	Alumina
Concentration	Acetone		(mL)	Weight(g)
(g/L)	Volume			
	Occupation			
	(vol%)			
100	70	0.6500	6.5000	11.85
	80	0.7429	7.4286	7.90
	90	0.8357	8.3571	3.95
150	70	0.9414	6.2759	11.85
	80	1.0759	7.1724	7.90
	90	1.2103	8.0690	3.95
200	70	1.2133	6.0667	11.85
	80	1.3867	6.9333	7.90
	90	1.5600	7.8000	3.95

The preparation of *green* started with weighing the CA and TiO₂-doped alumina according to Table 3.3. The weighed CA was poured into a glass (weight of the glass had to be predetermined) followed by addition of acetone with stated volume in Table 3.3 through syringe. Mixing and stirring of the mixture were done until total dissolve of CA in acetone. The glass containing the solution was then placed in a vacuum chamber for 10-minute-vacuum-process. This process ensured that the bubbles trapped in the solution could escape. Bubbles formation was one of the reasons to increase the porosity of the final products which were not desirable. Subsequently, after the extraction of the glass from the chamber, the weighed TiO₂-doped alumina was poured into the solution. The new mixture was weighed again together with the glass, acetone was then added into the mixture in order to rectify the evaporated acetone. The volume for the acetone addition was specified by subtracting the total weight of the TiO₂-doped alumina, CA, acetone, and glass onto the newest weight of the mixture. The mixture was then stirred and mixed, gently, to prevent formation of bubbles. This process was on-going until even slurry

mixture was formed. The slurry was ready for rheological test. If it was serving the purpose of preparing final product, it had to undergo the vacuum process once again followed by pouring into mould made by Teflon sheets. Optionally, wiping of CA-acetone mixture on the wall of the mould could be done first before filling up with the slurry to avoid sticking of the samples onto the wall.

Same processes of preparation of *green* samples were used on undoped alumina powder which was not ball-milled and doped with TiO₂. The compositions of the undoped alumina samples were the same as Table 3.2 and 3.3 by replacing the TiO₂-doped alumina powder with alumina powder. This was done to check the differences between doped and undoped samples.

3.1.4 Rheological Test on Slurry

Rheological test is an examination that study on the flow of the matter; for example, liquid, slurry, and suspensions. It could also be defined as the test on matters' deformation in response to induced forces. When samples undergo deformation or flow, there are three main factors that should be study on, which are the internal structure of the samples, the external forces applied on the samples, and the environmental or surrounding conditions such as the temperature. Rheological tests are vital for many fields such as material sciences, geophysics, pharmaceuticals, etc.

Rheometer in the laboratory was used to undergo rheological study on the slurry. Rheoplus was the software the incorporated with the rheometer in the laboratory. In this study, rheology test on the slurry samples have to be done to apprehend clearly the behaviour of the slurry flow and its applicability in the FDM printer. The test is run at constant temperature of 30 °C. There are numerous data can be obtained from this test; for instances, intrinsic and relative viscosity, stress relaxation, and frequency sweeps. The flow curve test for the slurry was the focus and it was recorded for further analysis.

3.1.5 Binder removal and Sintering

The profound explanation for binder removal and sintering can be viewed in Chapter 2.5 and 2.6.

Before the debinding process was done, the *greens* were left naturally dried for one day. The binder had to be removed from the body before sintering

process to prevent the influence of carbon delay that could distort the properties of final product. The *greens* were placed in the tube furnace at 400 °C for 1 hour for debinding. After debinding process, the *green* was removed and left for cooling. The *greens* were then placed in the tube furnace again but this time the temperature was set at 1400 °C for 1 hour for sintering process. All of the rate of temperature increase is at 10 °C/min. The sintered samples were removed and left for cooling. The graph of furnace temperature over time is plotted in Figure 3.1.

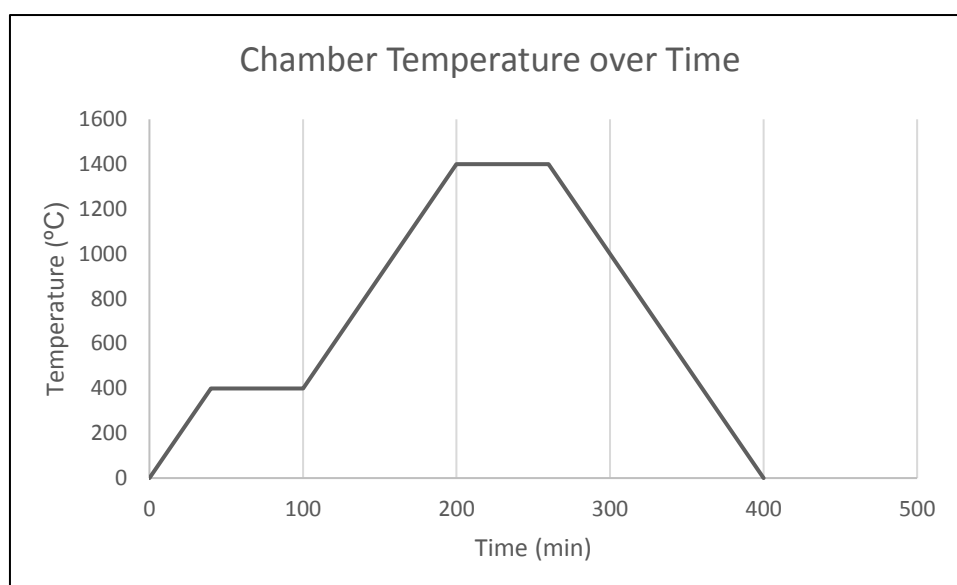


Figure 3.1: Graph of Chamber Temperature over Time.

3.1.6 Grinding and Polishing

Grinding and polishing are a type of process to make sure flat and good surface finishing of the final product. Grinding serves the purpose of material removal that cleans the surface of the specimen while polishing is utilized to develop a decent appearance on the specimen, avoid contamination, get rid of oxidation, and form a reflective surface. Flat and good surface finish of final product is beneficial by easing the visualization of indentation during Vickers hardness test, meeting flat surface requirement for XRD test, and allowing SEM in capturing clear and desired image.

In this experiment, a Metkon FORCIPOL grinding machine was used for the process. Sandpapers with grit size of 180, 320, 400, 600, and 1000 were used in the grinding process in ascending order from coarse to fine abrasion.

Water was kept rinsing on the specimen to get rid of the grinded leftover. During the grinding process, the orientation of the samples being grinded was altered by turning clockwise 90 ° every time when the sandpaper was changed to remove the saw mark of previous grinding. After grinding the sintered samples, a polishing paper was stick on the on the polishing wheel. Water based polycrystalline diamond suspension of 6 μm was sprayed on the polishing paper followed by scrubbing the grinded sample surfaces onto it. This process was continued by water based polycrystalline diamond suspension of 3 μm and 1 μm . After polishing, the samples were having good and flat surface finishing and ready for subsequent processes.

3.1.7 Thermal Etching

Thermal etching is explained thoroughly in Chapter 2.7.

The polished samples were placed in crucibles. The crucibles were then transferred into the carbolite furnace and the chamber temperature was adjusted to 1300 °C for 30 minutes. They were left for cooling and removed from the chamber.

3.1.8 Bulk Density Measurement

There are two ways in measuring the bulk density of the; by dividing the mass with the volume of the sample; or by water immersion method. Water immersion method was chosen since the shape of samples might be too complex and too time-consuming in calculating the volume. This method has a simple principle which follows the Archimedes principle where the density can be defined through the known density of liquid which is typically water, the dry weight of the sample in air, the wet weight of the sample when immersed in the liquid in which it will be lighter due to the buoyancy force caused by the weight of water displaced, and the wet dry weight of the samples (only for porous products). In this experiment, the liquid utilized was distilled water and the tool used was a standard Mettler Toledo Balance AG204 desi-meter to obtain the samples' density.

According to Fernandesl and Rego (1998), this technique provides a few notable benefits: it is fast, straightforward, and inexpensive; high flexibility even though the sample is geometrically complex; and it allows direct

determination of the density of the sample. However, water absorption is one of the limitations; for instance, this technique is not effective on hairy samples. Sample size that is too small for handling is also not practical in this technique. In this experiment, water had chances in being absorbed in the pores. In order to diminish the inaccuracy, the excess weight of water was not involved in calculations. After measuring the density of the samples, the experimental results were then compared to the theoretical density. Equation 3.1 depicted how the experimental density for porous sample was calculated.

$$\rho = \left(\frac{w_a}{w_a - (w_w - (w_{a+w} - w_a))} \right) \rho_w \quad (3.3)$$

Where

ρ = Sample's bulk density, g/cm³

w_a = Sample's weight in air or dry weight, g

w_w = Sample's weight in water or wet weight, g

w_{a+w} = Wet sample's weight in air or wet dry weight, g

ρ_w = Distilled water density (0.997 g/cm³ at 25 °C)

3.1.9 Vickers Hardness Determination

Hardness is defined as the measure of a material in resisting localized plastic deformation. The plastic deformation can be produced by abrasion or mechanical indentation. The hardness of specimen in this investigation was determined through Vickers hardness determination technique. Indentations on the specimen were induced by applying a 2 kgf load on a pyramidal diamond indenter. The load was slowly applied and the force was maintained for 10 seconds in order to induce an indentation. Throughout the testing, the force and the indenter had to be monitored and controlled carefully in order to achieve force accuracy and high indentation quality. Figure 3.2 shows the scheme for Vickers hardness test. Based on Figure 3.2, two notable diagonals of the indentation, D_1 and D_2 , were visible after the load was released and the indenter was removed. If indentations were made on work-hardened regions or areas near to edges, the result will not be accurate. To prevent this from occurring, the indentations were made away from the edges and more on the centre region of

the specimen. Equation 3.4 and 3.5 guide the calculation in order to obtain the Vickers hardness for each specimen.

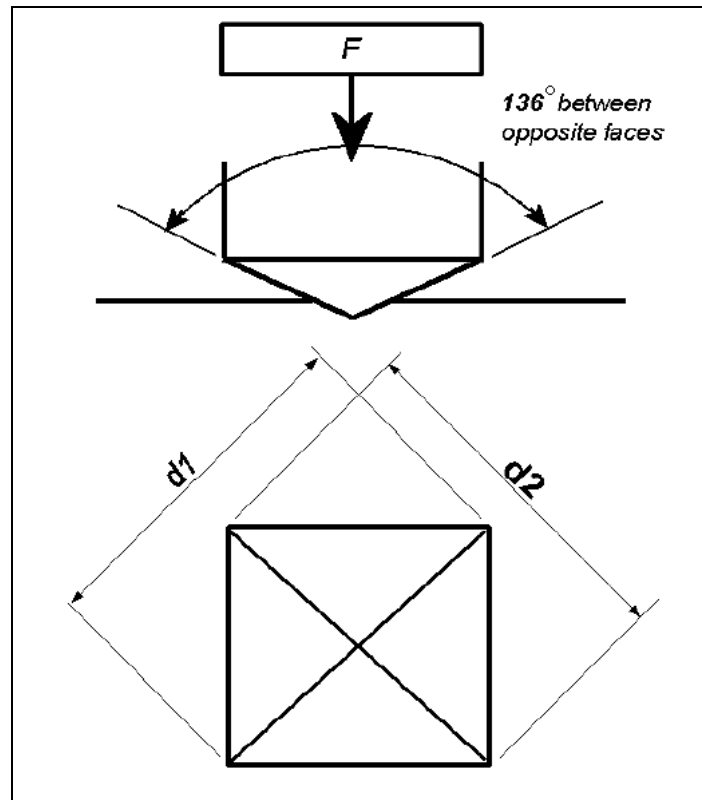


Figure 3.2: Vickers Hardness Test Schematic Diagram (Mohamed and Hegazy, 2017).

$$D = \frac{D_1 + D_2}{2} \quad (3.4)$$

Where

D = Arithmetic mean of two diagonals, D_1 and D_2 , μm

$$H_V = \frac{2F \sin \frac{136}{2}}{D^2} = \frac{1.854F}{D^2} \quad (3.5)$$

Where

H_V = Vickers hardness, kg/mm^2

F = Applied load, N

3.1.10 Microstructure Investigation

“Micro” stands for extreme small and “structure” stands for the arrangement of elements. Analysis of microstructure such as grain size can normally show the physical and mechanical properties; strength, toughness, hardness, etc.; of a material. In order to reveal microstructure, an SEM microscope with magnification up to 10000× has to be utilized. In this investigation, a Hitachi SEM model S-3400N as shown in Figure 3.3 was used to observe and capture the image of microstructure of the specimens. The procedure of microstructure investigation was as follows:

1. Samples were stuck firmly on each of the holders.
2. Samples with poor electrical conductivity were undergoing palladium sputter coating of around 15 nm before placing them into the SEM chamber to enhance the image because metal coating inhibits charges (Echlin, Gee and Chapman, 1985).
3. SEM was used to focus on a tiny region of the samples with electrostatic or electromagnetic force. The samples were scanned by SEM in a series of lines.
4. Electrons were emerged from the top face of the specimen and they were collected by an electron detector.
5. Microstructure images of the samples will be screened on the monitor.
6. Images were taken for further analysis and discussion.



Figure 3.3: Hitachi SEM model S-3400N

3.1.11 X-Ray Diffraction (XRD)

XRD is an analytical technique in determining the crystallization of the atomic and molecular structure. Its working principle is by shooting an x-ray beam towards the specimen while the beam will then be diffracted by the crystalline structure of the specimen. The data regarding the angle and the intensity of the diffracted beams is to be collected for further analysis. This data leads into visualization of the electron density within the crystal structure. This information brings into determination of atoms' mean positions in the structure, chemical bonds, etc.. Thus, the chemical composition within the samples can be known as well. The verification of the presence of impurities in the samples can be done through XRD.

In this experiment, the XRD device utilized was as shown in Figure 3.4. The angles of scanning onto the samples were from 20 ° to 50 ° with scanning steps of 2 °/min. The XRD information was then collected for further research.



Figure 3.4: XRD Device in UTAR

3.2 Work Plan Gantt Chart

Table 3.4: Final Year Project Part I Gantt Chart.

No.	Project Activities	W1	W2	W3	W4	W5	W6	W7	W8	W9	W10	W11	W12	W13	W14
M1	Problem Formulation and Project Planning	■	■												
M2	Literature Review and Data Gathering			■	■	■	■	■	■	■	■				
M3	Preliminary Test										■	■	■		
M4	Report Writing and Presentation													■	■

Table 3.5: Final Year Project Part II Gantt Chart.

No.	Project Activities	W1	W2	W3	W4	W5	W6	W7	W8	W9	W10	W11	W12	W13	W14
M1	Rheological Test on Slurries and <i>Green</i> Samples Preparation	■	■	■	■	■	■								
M2	<u>Debinding</u> and Sintering					■	■	■	■						
M3	Characteristic Tests, SEM photo taking, and XRD Test							■	■	■	■				
M4	Data Analysis										■	■	■		
M5	Report Writing and Presentation											■	■	■	■

3.3 Summary

First, alumina powder was doped with 1 wt% of TiO₂ and it was ball-milled. Doped alumina, CA, and acetone were mixed and vacuumed according to the compositions stated in Table 3.3. The rheological properties of the slurry were tested using rheometer. Then, the slurry was poured into mould and it was left drying for a day. Binder removal process was applied to the samples at 400 °C and followed by sintering process at 1400 °C in carbolite furnace. Bulk density tests, Vickers hardness tests, SEM investigation and XRD were done on the sintered samples.

CHAPTER 4

RESULTS AND DISCUSSION

4.1 Introduction

This chapter reveals the experimental result for properties of alumina-based feedstock for FDM 3D printer as well as the detailed analysis and the discussion on the results obtained. Highlighting of key data, interpretation and explanation of the results, and comparison of results to other researches can be found in this chapter. This chapter is divided into a few main parts: doping of TiO₂ into alumina powder, flow curve, condition of powder and sintered samples, bulk density, Vickers hardness, XRD analysis, and microstructural analysis.

4.2 Doping of TiO₂ into Alumina Powder

Doping of 1 wt% of TiO₂ into the alumina was done to reduce the sintering temperature to 1400 °C due to the inability of existing carbolite furnace to go beyond the mentioned temperature. Table 4.1 lists out the final weight or the weight of successfully doped alumina powder, the initial weight or the total weight of undoped TiO₂ and alumina, and the percentage difference or the percentage of wasted material for the two different batches of preparation. Both of the results obtained are acceptable due to low percentage difference. This result indicates that the percentage difference of doping of TiO₂ into alumina powder should be as close to zero as possible to prevent wastage of materials. According to researches done by Matsunaga, et al. (2003) and Kim, Hong and Kim (2000) and other researches regarding to doping in alumina, mass loss from doping is not emphasized because it can be done with almost 100 % efficiency. The lower the percentage difference, the higher the efficiency of the doping process. Mass loss only occur on carelessness throughout the doping process such as spilling of materials during handling.

Table 4.1: The Final Weight, Initial Weight, and the Percentage Difference of the TiO₂-doped Alumina Powder for Two Batches.

Batch	Initial Weight (g)	Final Weight (g)	Percentage Difference
1st	80	78.5232	1.8 %
2nd	150	148.2826	1.1 %

4.3 Flow Curve

Flow curve is best in determining the degree at which the semi-fluid or slurry resist to deform at different shear rate; in short, the viscosity of the slurry. Figure 4.1, Figure 4.2, and Figure 4.3 reveal the flow curve for TiO₂-doped, ball-milled alumina samples with CA-acetone concentration of 100 g/L, 150 g/L, and 200 g/L respectively. By observing Figure 4.1, Figure 4.2, and Figure 4.3, it can be obtained that when shear rate rises, the viscosity drops. As compared to experiment done by Muhammad (2015), the flow curves of the FDM machine feedstock materials are similar that when shear rate increases, the viscosity decreases. This phenomenon proves that high shear rates yield into alignment of polymer chain, and this will result into decrease in internal friction of the slurry and therefore diminish the viscosity.

Apparently, the similarity among Figure 4.1, Figure 4.2, and Figure 4.3 is that when the CA-acetone volume occupation goes up from 70 vol% to 90 vol%, this viscosity lessens. Slurry with 70 vol% of CA-acetone it is the most viscous. It is followed the slurry with 80 vol% and 90 vol%. Doped alumina powder and CA powder is the solute while the acetone is the solvent. According to Demirel and Gerbaud (2019), viscosity of pure acetone is at 0.224 mPa·s; therefore, the higher the volume percentage of the CA-acetone, the higher the proportion occupied by acetone in a unit volume, the less viscous the slurry will be.

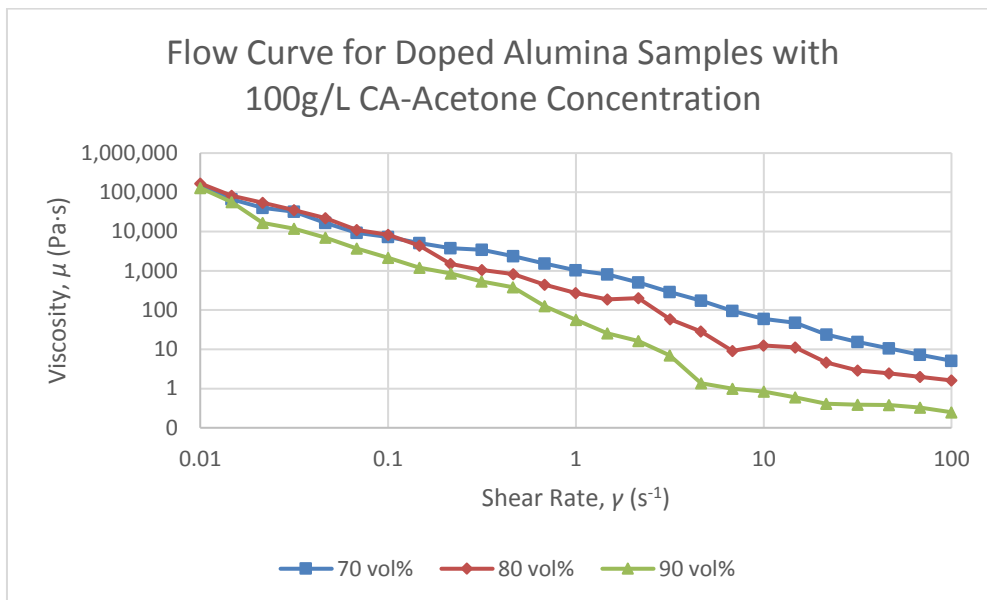


Figure 4.1: Flow Curve for Processed Alumina Samples with Binder CA-Acetone Concentration of 100 g/L.

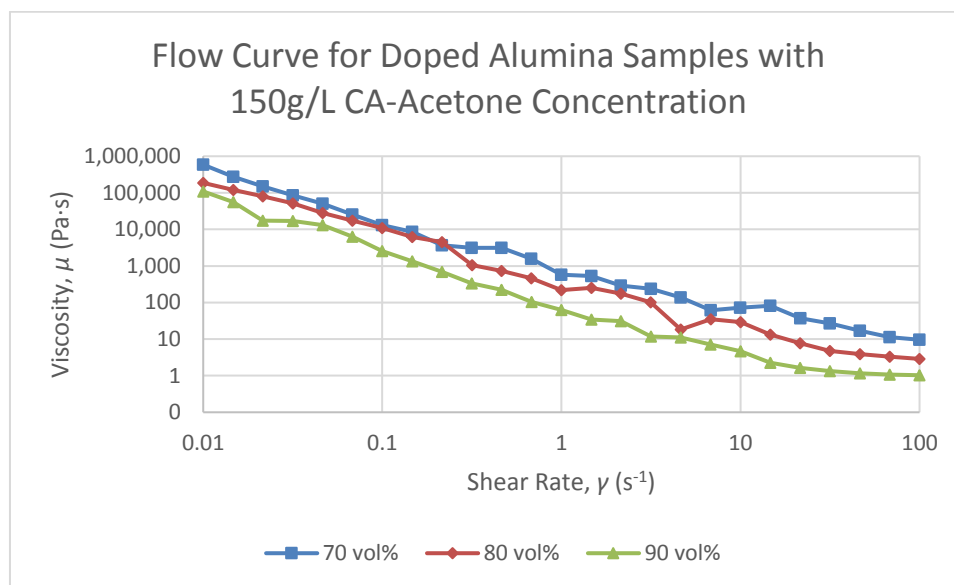


Figure 4.2: Flow Curve for Processed Alumina Samples with Binder CA-Acetone Concentration of 150 g/L.

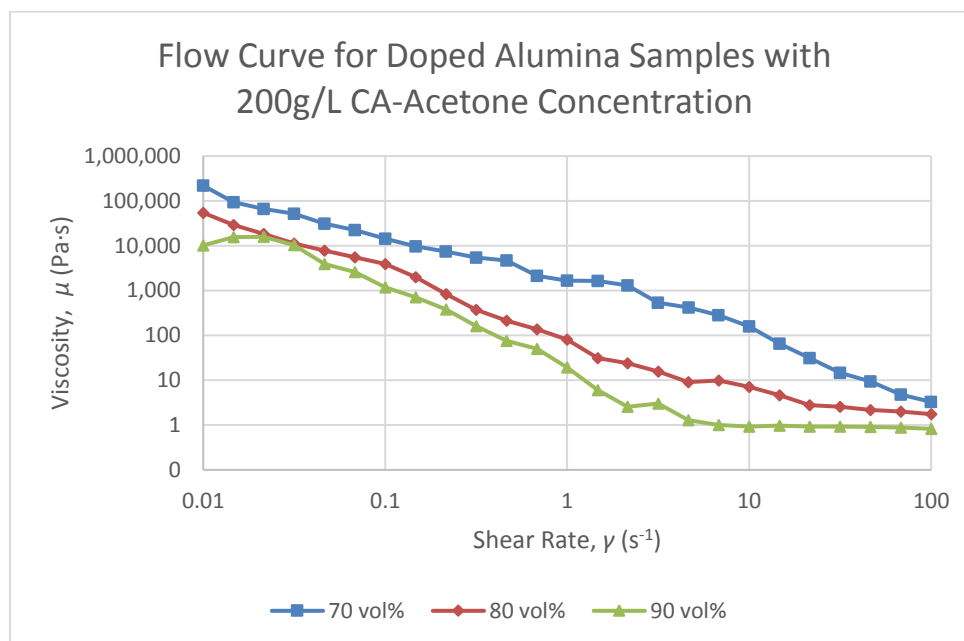


Figure 4.3: Flow Curve for Processed Alumina Samples with Binder CA-Acetone Concentration of 200 g/L.

Based on Chen, et al. (2019), the viscosity of the slurry, in general, is in between 10 Pa·s to 100 Pa·s to ensure steady, constant, and stable flow when passing through the FDM nozzle with a condition of well-dispersed ceramic particles in the slurry. Also, low viscosity is preferred due to better sintering properties and better adhesion between the extruded layers. With low viscosity, the material can be 3D printed in a shorter time as compared to high viscosity as the nozzle finds difficulties during extrusion of high viscosity slurry. However, too low a viscosity means that the ceramic particles occupy very less volume whereas the polymer binder is plenty; this could result in reduce in bulk density for the end-product. Therefore, Figure 4.1, Figure 4.2, and Figure 4.3 are summarised into Table 4.2 to record down the shear rate range that intersect the optimum slurry viscosity of 10 to 100 Pa·s. Geng, et al. (2019) discovered that the optimum nozzle extrusion speed is range from 5 mm/min to 80 mm/min and once the speed exceeded 109.8 mm/min, the sample printed will not in stable state and in bad quality. With a nozzle diameter of 400 μm , the optimum shear rate is in range from 0.1 to 1.1 s^{-1} . As compared to the shear rate in Table 4.2, slurry with 100 g/L 90 vol%, 150 g/L 90 vol%, 200 g/L 80 vol%, and 200 g/L 90 vol% show the best rheological properties for FDM nozzle extrusion;

slurry with 100 g/L 80 vol%, 150 g/L 80 vol%, shows moderate rheological properties for nozzle extrusion; while 100 g/L 70 vol%, 150 g/L 70 vol%, and 200 g/L 70 vol% can be totally excluded for FDM nozzle extrusion due to high viscosity that will disrupt the printing process.

Table 4.2: Table of Shear Rate Range that Falls between Viscosity of 10 to 100 Pa·s for Different CA-Acetone Concentration and Volume Occupation.

CA-Acetone Concentration (g/L)	CA-Acetone Volume Occupation (vol%)	Shear Rate Range Falls between 10 – 100 Pa·s (s⁻¹)
100	70	6.8 – 46.4
	80	2.5 – 14.7
	90	0.7 – 2.5
150	70	5.0 – 100
	80	3.2 – 18
	90	0.7 – 4.8
200	70	12 – 46
	80	0.8 – 6.81
	90	0.4 – 1.2

4.4 Condition of Powder and Sintered Samples

This section aims to show the differences between undoped, unball-milled alumina powder and TiO₂-doped, ball-milled alumina powder. Figure 4.4 and Figure 4.5 show the SEM micrographs of undoped, unball-milled spray dried grade alumina powder and TiO₂-doped, ball-milled alumina powder respectively with ×100 on the left and ×1000 on the right. Figure 4.4 proves that the agglomerate size of the unprocessed alumina powder is ranging from 150 μm to 450 μm and it has an average size of 300 μm while the right of Figure 4.4 shows the surface of the agglomerate which consist of the alumina particles. On the other hand, the processed powder particle size is averagely 50 μm which is shown in Figure 4.5. Apparently, the size of ball-milled powder is finer at it is only 16.7 % the size of the unball-milled powder.

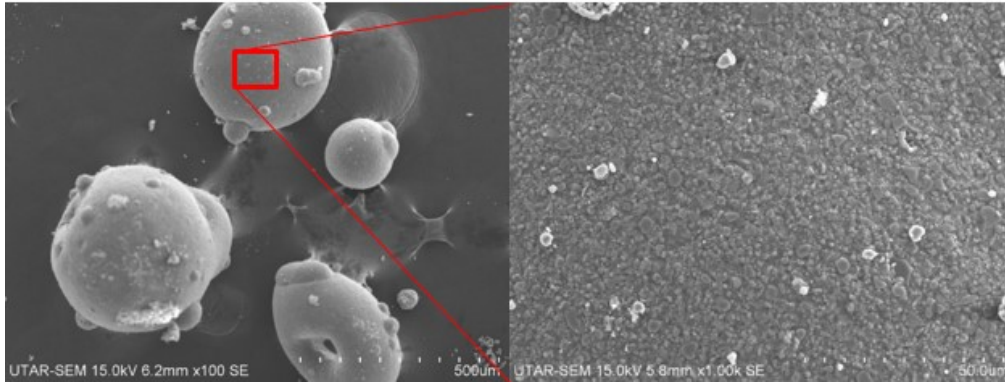


Figure 4.4: SEM Micrographs of Undoped, Unball-milled Spray Dried Grade Alumina Powder.

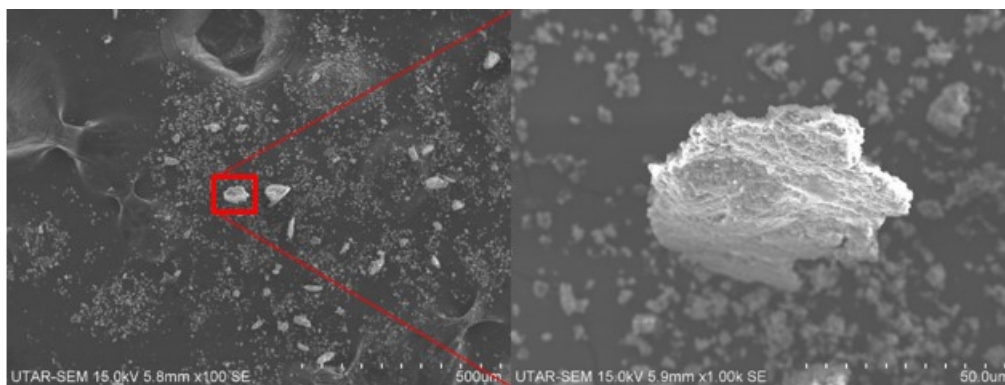


Figure 4.5: SEM Micrographs of TiO₂-doped, Ball-milled Alumina Powder.

Figure 4.6 and Figure 4.7 demonstrates the condition of sintered samples for untreated and treated alumina powder respectively. Figure 4.6 displays that the sintered sample with untreated powder crushed when it is removed from the carbolite furnace while Figure 4.7 displays that the sintered sample with treated powder has become hard, strong, and uncrushable by bear hands. This result provides unequivocal evidence that a large granulate size of 300 μm results into failure in densification, linking of particle, and strengthening of the necks or sintered contacts during sintering; however, the sintering process success in the particle size of 50 μm . This experimental outcome is similar to researches done by Sofia, Barletta, and Poletto (2018) and Rahimian, et al. (2009) which are shown in Figure 2.7 and Figure 2.8 respectively that it is the best to maintain the particle size between 10 to 50 μm .

There is another reason that supports this situation, which is the sintering temperature. According to Roy, et al. (1993) in Chapter 2.6, it is clearly stated

that the best sintering temperature for pure alumina is at 1500 °C and it should be held for 1 hour; Likewise in Chapter 2.6.1, it is evidently confirmed that if the alumina is doped with 1 wt% of TiO_2 , the best sintering temperature drops to 1400 °C with duration of 1 hour (Ting, et al., 2008). Due to limitation of the available carbolite furnace, the maximum temperature can be attained is 1400 °C. Undisputably, this situation satisfies the doped alumina samples but not the pure alumina. This is going to result in slight inconsistency in densification, linking of particle, and strengthening of the necks of the pure alumina during sintering.

Due to unfavourable condition in undoped, unball-milled pure alumina powder, pure alumina samples are excluded in the proceeding material characterization tests.



Figure 4.6: Sintered Samples with Undoped, Unball-milled Alumina Powder.



Figure 4.7: Sintered Samples with TiO_2 -doped, Ball-milled Alumina.

4.5 Bulk Density

Bulk density test is an essential method in analysing the quality of the final product. Table 4.3 has listed out the bulk density and relative density results for sintered TiO₂-doped alumina samples while Figure 4.8 represents an analysis of comparisons of relative density of those samples. Sample calculation of the bulk density is in Appendix A. The chart has evidently shown that the lowest bulk density obtained is 2.123 g/cc (53.75 %) from sample of 200 g/L CA-acetone concentration and CA-acetone volume occupation of 90 vol% while the highest bulk density obtained is 2.963 g/cc (75.01 %) from sample of 200 g/L CA-acetone concentration and CA-acetone 80 vol%. The comparisons of result with various other methods by other researchers are done in Table 4.4. This comparison shows that the SL method is by far the best method in 3D printing; However, printing method using CA as binder is still feasible and still having potential. Due to limitation of equipment for sintering, the alumina samples could attain the ideal pressureless sintering temperature of 1600 °C and to hold for 1 hour.

Figure 4.8 reveals that the bulk density peaks at 80 vol% of binder-acetone for all of the CA-acetone concentration. From this, it can be deduced that as the CA-acetone volume occupation goes down from 80 vol%, the binder does not bind the alumina particles properly; likewise, if the CA-acetone volume occupation goes beyond 80 vol%, too much binder content results into the worst binding density due to lesser alumina particles per unit volume (only 10 vol%), according to Zaitsev, et al. (2017), lower viscosity of paste induces lower binding action; at 80 vol%, the alumina particles adhere to each other closely and perfectly with the help of the binder. This peaking trend is similar to research done by Pigram and Freer (1995) where the bulk density of their samples peaks at 91.5 % of relative density when the binder PEG is at 1.0 wt%.

It is important to consider another phenomenon that can be seen by observing Figure 4.8; As the CA-acetone is more diluted, the binder-solvent volume occupation will be more insignificant to the bulk density as the graph goes flatter. This occurrence is because decrease in CA-acetone concentration in a sample will, mathematically act as a multiplication factor, develop less difference in CA amount with different CA-acetone volume occupation. In

simpler word, CA-acetone concentration is going to multiply the CA-acetone volume occupation to get the result. Higher CA-acetone concentration with the meaning of higher multiplication factor induce a higher magnitude of fluctuation in the results.

Table 4.3: The Bulk Density and Relative Density Results for Sintered TiO₂-doped Alumina Samples.

Sample Composition		Bulk Density	Relative Density
CA-Acetone Concentration (g/L)	CA-Acetone Volume Occupation (vol%)	(g/mL)	(%)
100	70	2.666	67.49
	80	2.759	69.85
	90	2.611	66.10
150	70	2.618	66.28
	80	2.819	71.37
	90	2.221	56.23
200	70	2.708	68.56
	80	2.963	75.01
	90	2.123	53.75

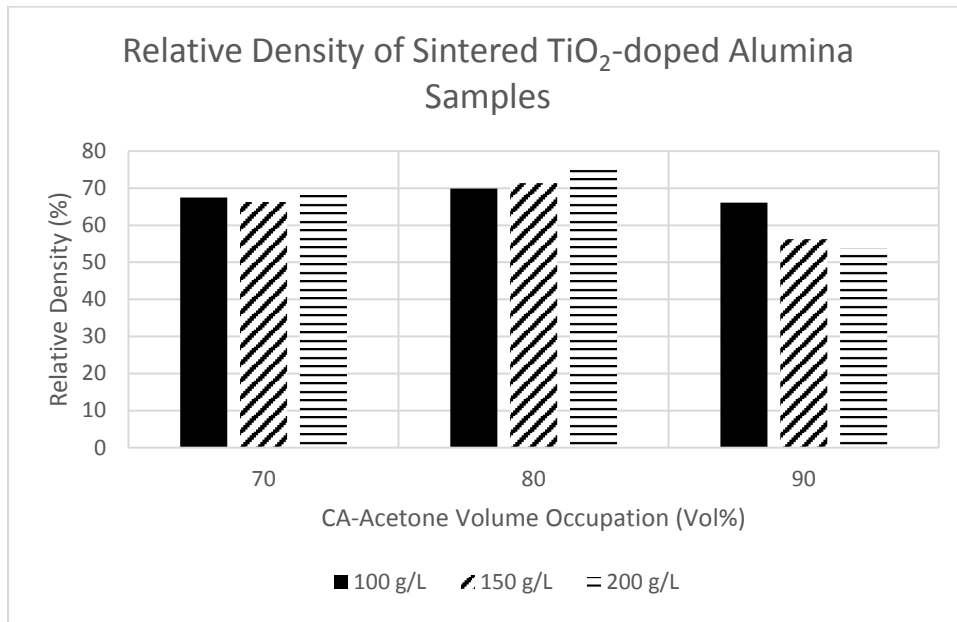


Figure 4.8: Bar Chart of Comparison between Relative Density of TiO₂-doped Alumina Samples.

Table 4.4: Comparison of Relative Bulk Density of Different 3D Printing Method.

3D Printing Method	Condition	Relative Density
Present work	Mixed with CA-Acetone and sintered at 1400 °C for 1 hour	75 %
IJP (Hamano and Ikoma, 2018)	Mixed with PAA and sintered at 1500 °C for 5 hours	40 %
IJP (Peng, et al., 2018)	Mixed with ethylene glycol, deionized water, and acrylic acid and sintered at 1450 °C for 3 hours	82 %
DLP (Varghese, et al., 2017)	Mixed with poly(ethylene glycol) diacrylate and phenyl bis (2,4,6-trimethyl(benzoyl)phosphine) and sintered at 1500 °C for 6 hours	74 %
SL (Zhou, et al., 2016)	Mixed with acrylamide and methylene-bis-acrylamide and sintered at 1650 °C for 1 hour	99 %
SL (Zhang, Sha and Zhao, 2016)	Mixed with dicarboxylic acid, methanol and phosphoric acid and sintered at 1550 °C for 2 hours	96 %

4.6 Vickers Hardness

Vickers hardness is one of the main physical properties that shows how resist a sample is to localized plastic deformation that is made by abrasion or mechanical indentation. Table 4.5 tells the results of Vickers hardness for three different samples with same binder occupation of 80 vol% but different CA-acetone concentration (100 g/L, 150 g/L, and 200 g/L). Sample calculation of Vickers hardness is in Appendix A. The results with the highest hardness of 3504 MPa and the lowest hardness of 3396 MPa have apparently validated that the changes in CA-acetone concentration with same binder-solvent volume occupation are not resulting in notable changes in the hardness. They have an average hardness of 3450 MPa. As compared to the theoretical alumina hardness which is 28 GPa from (Andersson, 2005), the hardness of alumina samples obtained is just 12.3 % of the theoretical. The comparison of the results on hardness with other sources is recorded in Table 4.6. Evidently, the hardness of the samples prepared is comparatively much lower than the other researches. The faulty and inconsistent result can be induced by the shape of the samples which, occasionally, their bases are not flat enough the prevent the samples from moving when force is being applied. Also, defective Vickers hardness tester could be the cause of unreliable result. The Vickers hardness tester shows blurred image of the sample surface after usage for a long time.

Table 4.5: Table of Vickers Hardness Results of Samples Binder 80 vol% with Three Different CA-Acetone Concentration.

Sample Composition		Average	Hardness
CA-Acetone Concentration (g/L)	CA-Acetone Volume Occupation (vol%)	Vickers Hardness, Hv (kg/mm ²)	(MPa)
100	80	346.30	3396
150	80	357.35	3504
200	80	351.90	3451

Table 4.6: Comparison of Results on Hardness with Different Sources.

Source	Condition	Hardness Percentage to Theoretical
Theoretical value (Andersson, 2005)	Theoretical.	100 % (28 GPa)
Present work	1 wt% TiO ₂ -doped alumina powder mixed with CA-Acetone and sintered at 1400 °C for 1 hour.	12 % (3.45 GPa)
(Ting, et al., 2008)	Alumina green sample is doped with 1 wt% of TiO ₂ compacted uniaxially and CIPed with sintering at 1400 °C for 2 hours holding time.	59 % (16.49 GPa)
(Zhou, et al., 2016)	Stereolithography. Alumina powder mixed with acrylamide and methylene-bis-acrylamide and sintered at 1650 °C for 1 hour.	63 % (17.5 GPa)
(Mamatha, et al., 2018)	3DP with ram typer extruder. Alumina powder is mixed with methyl cellulose (0.25 wt%) and PEG. Sample is sintered at 1650 °C for 1 hour.	54 % (15 GPa)

4.7 XRD Analysis

Different types of materials vary in their own XRD patterns because different materials exhibit different intensities and angles of diffractions when an x-ray beam is shot through them. This distinctive property allows the researchers to determine the types of materials presented in the samples. Figure 4.9, Figure 4.10, and Figure 4.11 have illustrated the XRD patterns and the analysis for “search and match” for samples with CA-acetone concentration of 100 g/L, 150 g/L, and 200 g/L respectively. Three of the mentioned samples come with the same binder occupation level of 80 vol%. Similar to expectation, the “search and match” results have clearly stated that three of the samples below predominantly match the XRD pattern of alumina. This brings up the meaning that the final samples consist of mainly alumina.

Also, the XRD pattern of CA is not visible in Figure 4.9, Figure 4.10, and Figure 4.11. The reason to this observation is that the binder removal process which involve heating of 400 °C has successfully decomposed all of the CA from the samples. This result proves that Trivedi, et al. (2015) is correct on the temperature that can fully decompose the CA. Debinding process is essential to prevent carbon delay (occur when temperature gets over 570 °C) on the sample during sintering process that will distort the end result. The details of this situation are described in Chapter 2.5.

Figure 4.9, Figure 4.10, and Figure 4.11 show that as the CA-acetone concentration increases from 100 g/L to 200 g/L, the peak intensities increase as well. The increasing peak intensities trend is similar to the research done by Barma and Mandal (2014) where increasing sintering temperature will result in increasing peak intensities. It can be explained by the theory of rising peak intensities represent higher crystallinity which means sample with 200 g/L binder concentration has the best crystallinity. The increasing CA content per litre of acetone could result in better binding action and eventually the microcrystal of α -alumina is being able to undergo a more intense recrystallization and grain growth during heat treatment process.

The results also do demonstrate that there are no changes between XRD pattern of the final samples and the pure α -alumina powder. By comparing this result to the research done by Varghese, et al. (2017), their result was identical

which the raw powder and sintered 3D printed sample showed no difference in XRD. One contributing factor to these outcomes is that there is no phase change throughout the processes. This proves that 3D printing done by Varghese and the methods done in this research do not affect the phase stability of alumina.

It is important not to overlook that the XRD pattern for TiO_2 is not obvious in Figure 4.9, Figure 4.10, and Figure 4.11. According to Figure 2.37, the peaks of TiO_2 falls at around 25° , 38° , and 47° between 20° to 50° . Except for 47° , the other two peaks are similar with the peaks of alumina which they might be covered up and become unobvious. The situation of invisible TiO_2 XRD pattern could also be induced because of too little weightage of only one percent in the composition which makes it hard to be diffracted properly by the ray.

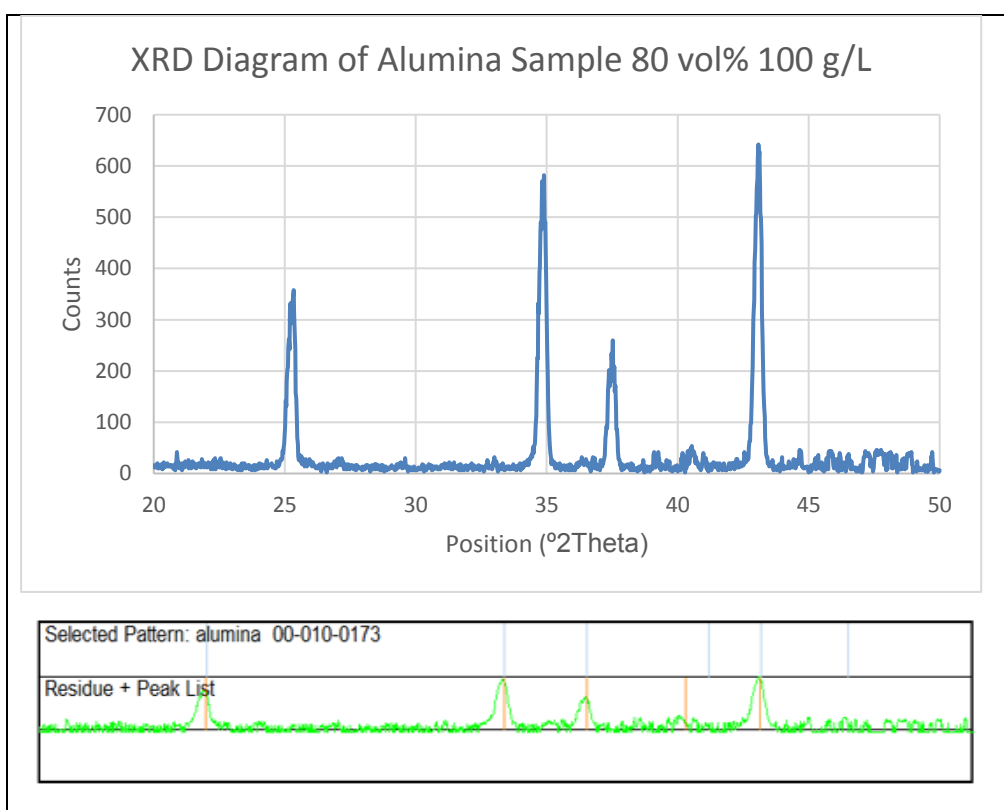


Figure 4.9: XRD Pattern and “Search and Match” Result of Samples with CA-acetone Concentration of 100 g/L and CA-acetone Volume Occupation of 80 vol%.

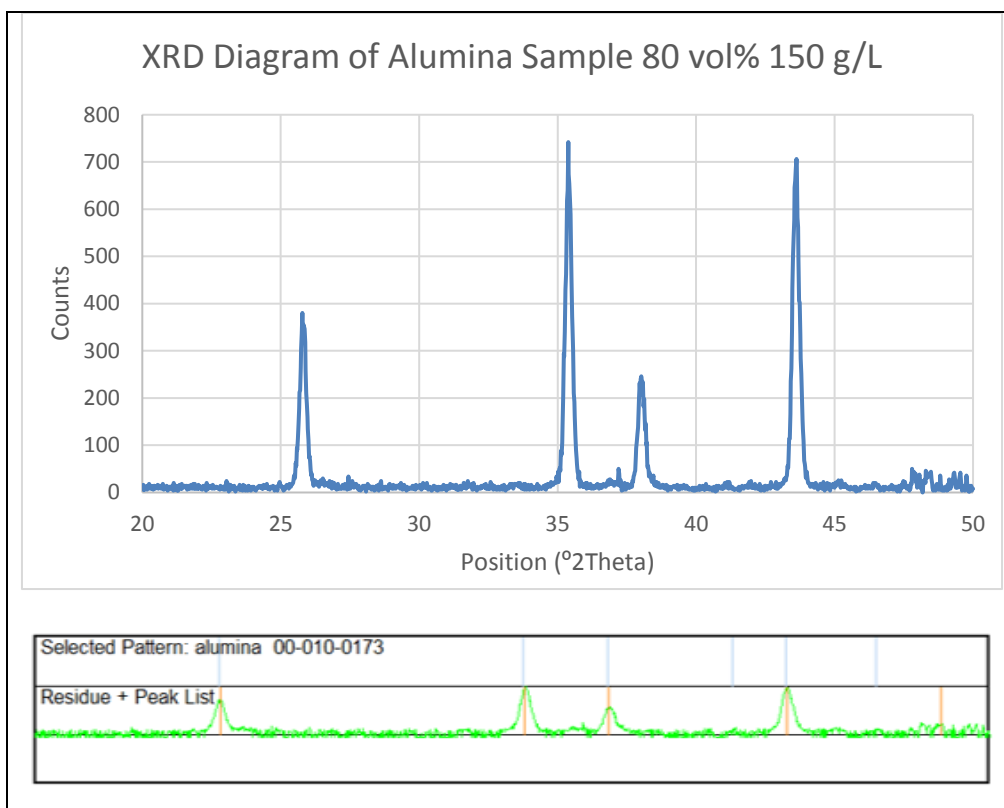


Figure 4.10: XRD Pattern and “Search and Match” Result of Samples with CA-acetone Concentration of 150 g/L and CA-acetone Volume Occupation of 80 vol%.

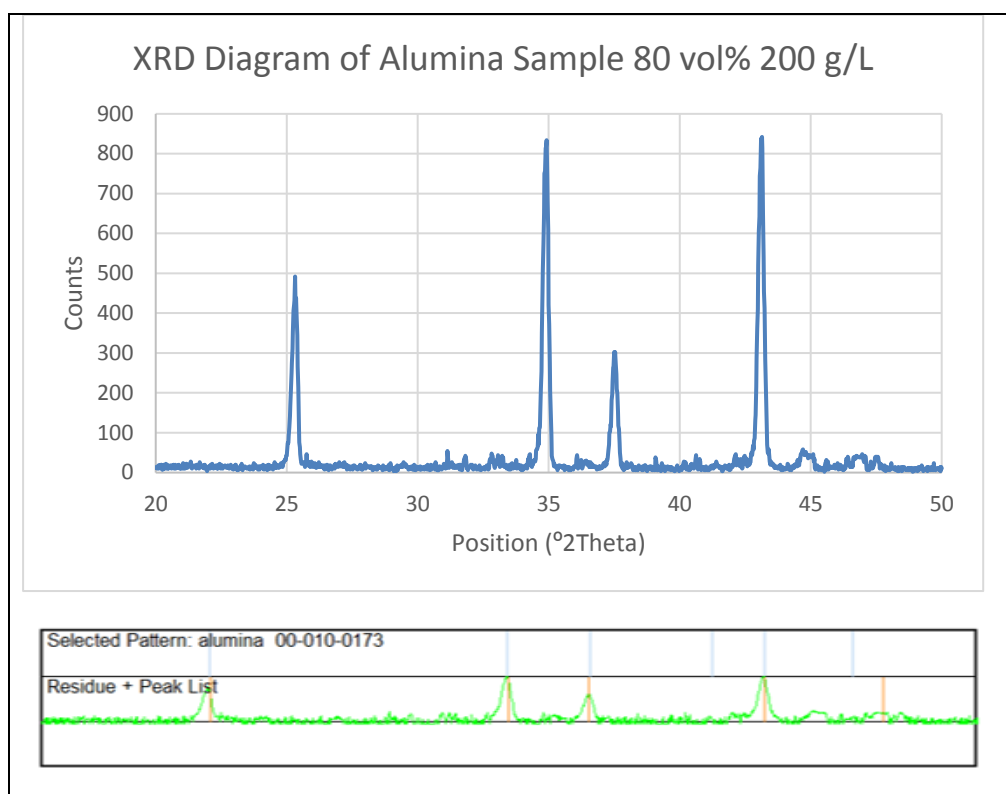


Figure 4.11: XRD Pattern and “Search and Match” Result of Samples with CA-acetone Concentration of 200 g/L and Binder CA-acetone Volume Occupation of 80 vol%.

4.8 Microstructure Analysis

Microstructure analysis is to study the magnified image of the surface of the samples in order to examine the grain growth, the porosity, and the microstructural homogeneity. Figure 4.12 and Figure 4.13 portray the SEM micrographs of 1400 °C sintered TiO₂-doped alumina samples with CA-acetone volume occupation of 80 vol% and CA-acetone concentration of 100 g/L, 150 g/L, and 200 g/L. In the figures mentioned, Figure 4.12 shows micrographs with ×1000 magnification while Figure 4.13 shows micrographs with ×5000 magnification.

As comparing Figure 4.12 (a), (b), and (c), it can be evidently seen that the microstructure compaction or the packing density enhances as acetone concentration increases from 100 g/L to 200 g/L. Also, the sample with 200 g/L is having the highest bulk density of 2.963 g/cc. One of the reasons contributing to better microstructural properties is that the binding action in 200 g/L CA-acetone concentration is higher as compared to lower concentration and this

provides a better densification platform in the sintering process. With a more compact microstructure, porosity is lower. Besides, porosity could be formed by air bubbles that trapped in the slurry during the preparation process; or by shrinkage during solidification; or by poor binding action. According to Aqida, Ghazali and Hashim (2004), porosity is one of the main sources to poor mechanical properties including reducing Young's modulus, diminishing yield strength, and increasing crack formation; therefore, porosity is not desirable.

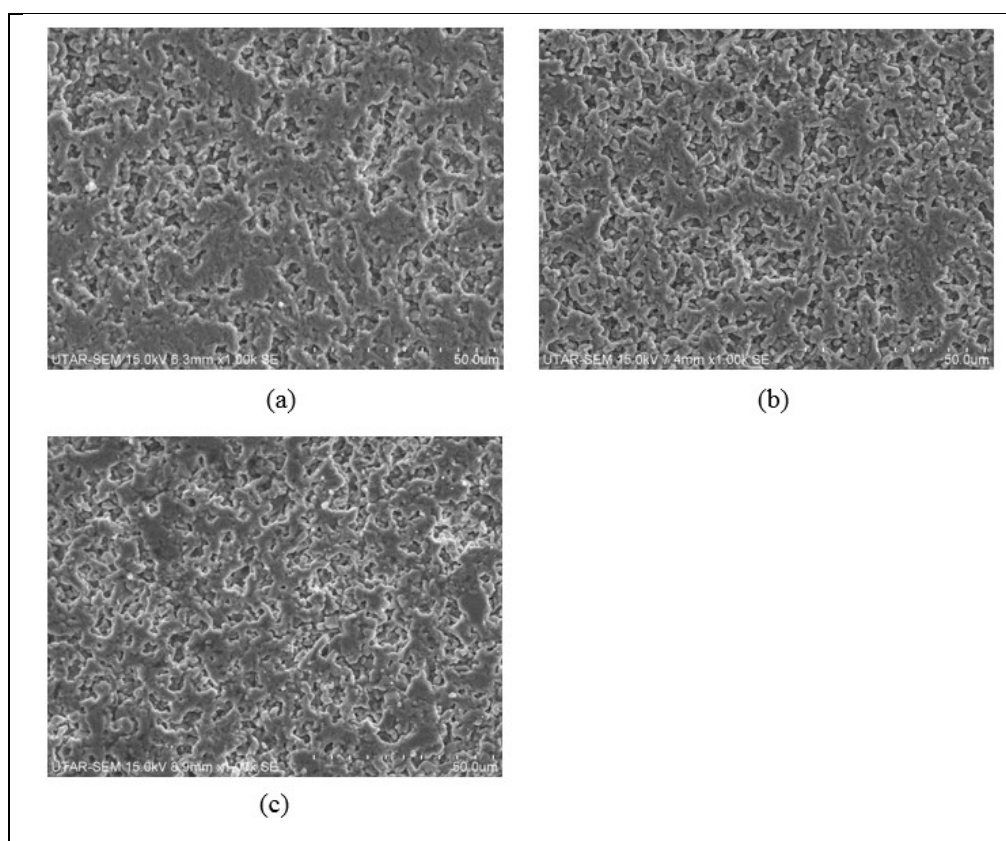


Figure 4.12: SEM Micrographs of $\times 1000$ Magnification of TiO_2 -doped Alumina Sample with CA-acetone Volume Occupation of 80 vol% and CA-Acetone Concentration of (a) 100 g/L, (b) 150 g/L, and (c) 200 g/L; Sintered at 1400 °C.

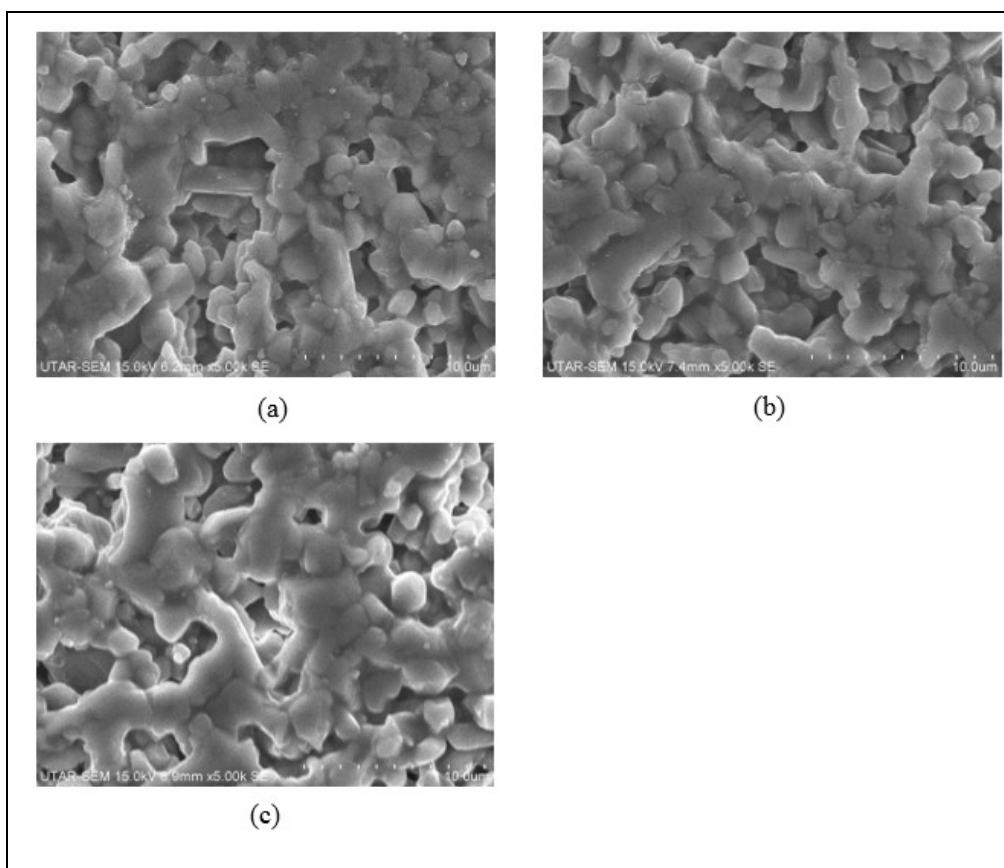


Figure 4.13: SEM Micrographs of $\times 5000$ Magnification of TiO_2 -doped Alumina Sample with CA-acetone Volume Occupation of 80 vol% and CA-Acetone Concentration of (a) 100 g/L, (b) 150 g/L, and (c) 200 g/L; Sintered at 1400 °C.

4.9 Summary

This chapter has revealed the results of this research in details followed by reasonable comparison and explanation. The doping of TiO_2 into alumina powder is successful with mass percentage difference of 1.1 % and 1.8 %. The ceramic-binder suspension flow curve determination has shown that 100 g/L 90 vol%, 150 g/L 90 vol%, 200 g/L 80 vol%, and 200 g/L 90 vol% of ceramic suspension are giving out the best viscosity for nozzle extrusion; which their viscosity falls between 10 to 100 Pa·s under the working shear rate of 0.1 to 1.1 s^{-1} as suggested by Chen, et al. (2019). Moreover, this research has also shown that implementation of the spray dried grade alumina powder is resulting into weak and fragile sintered product while implementation of ball-milled TiO_2 doped powder is resulting into strong and hard sintered product. The bulk density test has disclosed that sample with 200 g/L of binder concentration and

80 vol% of binder-solvent volume occupation is having the highest bulk density of 2.963 g/cc (75.01 % relative density). Furthermore, this research has shown that Vickers hardness of the three densest samples have the average hardness of 3450 MPa. The XRD analysis has validated that only alumina is detectable in the final samples and CA has proven to be decomposed entirely. The microstructure analysis has verified that the sample of 200 g/L of binder concentration and 80 vol% of binder-solvent volume occupation is possessing the best microstructural properties because it is having the highest compaction of microstructure and the least porosity. Also, the microstructural analysis has shown that all of the samples result in no phase change after sintering.

CHAPTER 5

CONCLUSION AND RECOMMENDATIONS

5.1 Conclusion

This research has formulated the best alumina-based feedstock for FDM 3D printer and the properties of the final products including viscosity, bulk density, XRD pattern, and microstructure have been determined. It was found that the best alumina-binder (CA) suspension composition for FDM comprises:

- Concentration of binder: 200 g CA per litre acetone (200 g/L),
- Binder-solvent volume occupation: 80 vol%,
- Ball-milled powder with 50 μm mean particle size.

The composition mentioned is chosen because the research has provided clear evidence that it possesses the highest bulk density of 2.963 g/cc (75.01 % relative density) with viscosity of 10 to 100 Pa·s (working shear rate of 0.1 to 1.1 s^{-1}) as recommended by Chen, et al. (2019) for FDM extrusion. Plus, XRD pattern shows only alumina due to total decomposition of CA after binder removal heat treatment, and it owns the best microstructural properties of low porosity and no phase change after sintering. A possible explanation is that the proper CA-acetone concentration of binder could enhance the binding action between alumina particles which succeeded in the densification process. However, binder volume occupation shall not exceed 80 vol% because it causes reduction in bulk density in the samples. On the other hand, it shall not be lower than 80 vol% because the incomplete binding action diminishes the densification process. These results suggest the mixing of CA and acetone into ball-milled alumina powder with correct composition could develop a slurry that is feasible to be used in FDM 3D printer.

5.2 Recommendation for future work

The sintering process in this project is restricted to maximum heating temperature of only 1400 °C due to the limitation of equipment available in the laboratory. It is recommended to sinter the alumina samples at 1500 °C and above to have a better densification of the sintered samples. Moreover, the sticky, mud-like, and uneven-drying nature of the ceramic suspension is causing difficulties in sample shape manipulation. The shape of end product tends to be irregular and it toughens the latter property testing such as in Vickers hardness test, the sample surface was bumpy and it made the indentation faulty. To achieve good sample shape manipulation, a thin protective layer of CA-acetone has to be laid between the ceramic suspension and the other contacted surfaces to prevent from undesirable sticking. This project is limited to manual stirring method with separated vacuuming process that is not able to ensure totally no air bubble in the slurry. Air bubbles are one of the main reasons of porosity and low bulk density. To overcome this concern for future work, a vacuum mixer is suggested. Other physical and mechanical properties such as tensile strength and fracture toughness could be conducted lead to a more accurate result with more considerations. Last but not least, it is recommended that future work should focus on the method in maintaining the viscosity of the slurry in the printing process because the slurry is subject to high volatile acetone.

REFERENCES

Agarwala, M. K., Jamalabad, V. R., Langrana, N. A., Safari, A., Whalen, P. J. and Danforth, S. C., 1996. Structural quality of parts processed by fused deposition. *Rapid Prototyping Journal*, [e-journal] 2(4), pp. 4–19. <http://dx.doi.org/10.1108/13552549610732034>.

Agilent Technologies, 2015. *Polymer Molecular Weight Distribution and Definitions of MW Averages*. [online] Available at: <<https://www.agilent.com/cs/library/technicaloverviews/Public/5990-7890EN.pdf>> [Accessed 20 August 2019].

Anand, R., 2014. *Preparation of Dense Alumina Ceramic by Slip Casting Method*. B. Eng.. National Institute of Technology Rourkela.

Andersson, J. M., 2005. *Controlling the Formation and Stability of Alumina Phases*. PhD. Linköping University. Linköping: UniTryck.

Aqida, S. N., Ghazali, M. I. and Hashim, J., 2004. Effect of Porosity on Mechanical Properties of Metal Matrix Composite: An Overview. *Jurnal Teknologi*, [e-journal] 40(A), pp. 17–32. <http://dx.doi.org/10.11113/jt.v40.395>.

Auerkari, P., 1996. Mechanical and physical properties of engineering alumina ceramics. *VTT Manufacturing Technology*, 1792, pp 1-26.

Bao, C., 2015. *Cellulose acetate / plasticizer systems : structure , morphology and dynamic*. PhD. Université Claude Bernard. Available at: <<https://tel.archives-ouvertes.fr/tel-01186696>> [Accessed 13 August 2019].

Barma, S. and Mandal, B., 2014. Effects of sintering temperature and initial compaction load on alpha-alumina membrane support quality. *Ceramics International*, [e-journal] 40(7), pp. 11299–11309. <http://dx.doi.org/10.1016/j.ceramint.2014.03.134>.

Becker, F. H. and Gmbh, R., 2006. Debinding Processes - Physical and Chemical Conclusions and Their Practical Realisations. *Ceramic Forum International*, 83(5), pp. 88–99.

Ben Best, 2008. *Lessons for Cryonics from Metallurgy and Ceramics*. [online] Available at: <<https://www.benbest.com/cryonics/lessons.html>> [Accessed 10 July 2019].

Mukhaimar, S., Makhool, S. and Samara, Q., 2015. *3D printing technology*. B.Eng.. Berzeit University.

Black, J. T. and Kohser, R. A., 2011. *DeGarmo's Materials and Processes in Manufacturing*. 11th ed. New Jersey: Wiley.

Carter, C. B. and Norton, M. G., 2013. *Ceramic materials: Science and engineering*. Berlin: Springer.

Chen, Z., Li, Z., Li, J., Liu, C., Lao, C., Fu, Y., Liu, C., Li, Y., Wang, P. and He, Y., 2019. 3D printing of ceramics: A review. *Journal of the European Ceramic Society*, [e-journal] 39(4), pp. 661–687. <http://dx.doi.org/10.1016/j.jeurceramsoc.2018.11.013>.

Chinelatto, A. S. A., Pallone, E. M. d. J. A., Souza, A. M. d., Manosso, M. K., Chinelatto, A. L. and Tomasi, R., 2012. Mechanisms of Microstructure Control in Conventional Sintering. In: A. Lakshmanan, ed. 2012. *Sintering of Ceramics: New Emerging Techniques*. London: IntechOpen. pp. 401–422.

Chinn, R. E., 1998. *Ceramography: Preparation and Analysis of Ceramic Microstructures*. Ohio: ASM International.

Demirel, Y. and Gerbaud, V., 2019. *Nonequilibrium Thermodynamics*. 4th ed. Lincoln: Elsevier.

Echlin, P., Gee, W. and Chapman, B., 1985. Very low voltage sputter coating. *Journal of Microscopy*, 137(2), pp. 155–169.

Egot, M. P. and Alguno, A. C., 2018. Preparation and Characterization of Cellulose Acetate from Pineapple (*Ananas comosus*) Leaves. *Key Engineering Materials*, [e-journal] 772, pp. 8–12. <http://dx.doi.org/10.4028/www.scientific.net/kem.772.8>.

Encyclopaedia Britannica, 2016. *Traditional Ceramics*. [online] Available at: <<https://www.britannica.com/technology/traditional-ceramics>> [Accessed 10 July 2019].

Fernandesl, P. M. and Rego, F. C., 1998. A New Method to Estimate Fuel Surface Area- to-Volume Ratio Using Water Immersion. *Int. J. Wildland Fire*, 8(3), pp. 121–128.

Fischer, S., Thümmeler, K., Volkert, B., Hettrich, K., Schmidt, I. and Fischer, K., 2008. Properties and applications of cellulose acetate. *Macromolecular Symposia*, [e-journal] 262(1), pp. 89–96. <http://dx.doi.org/10.1002/masy.200850210>.

Garechana, G., Río-Belver, R., Bidosola, I. and Cilleruelo-Carrasco, E., 2019. A method for the detection and characterization of technology fronts: Analysis of the dynamics of technological change in 3D printing technology. *PLoS ONE*, [e-journal] 14(1), pp. 1–28. <http://dx.doi.org/10.1371/journal.pone.0210441>.

Geng, P., Zhao, J., Wu, W., Ye, W., Wang, Y., Wang, S. and Zhang, S., 2019. Effects of extrusion speed and printing speed on the 3D printing stability of extruded PEEK filament. *Journal of Manufacturing Process*, [e-journal] 37, pp. 266–273. <http://dx.doi.org/10.1016/j.jmapro.2018.11.023>.

Gonzalez-Gutierrez, J., Cano, S., Schuschnigg, S., Kukla, C., Sapkota, J. and Holzer, C., 2018. Additive manufacturing of metallic and ceramic components by the material extrusion of highly-filled polymers: A review and future perspectives. *Materials*, [e-journal] 11(840), pp. 1–36.

<http://dx.doi.org/10.3390/ma11050840>.

Hamano, R. and Ikoma, T., 2018. Preparation of α -alumina powder and binder for 3D printer. *MRS Advances*, [e-journal] 3(18), pp. 969–975. <http://dx.doi.org/10.1557/adv.2018.300>.

Hatzenbichler, M., Geppert, M., Gruber, S., Ipp, E., Almedal, R. and Stampfl, J., 2012. *DLP based light engines for additive manufacturing of ceramic parts*. In: SPIE (Society of Photo-Optical Instrumentation Engineers) 8254, Emerging Digital Micromirror Device Based Systems and Applications IV. San Francisco, California, United States of America, 13 February 2012. Washington: SPIE.

Huang, S., Ye, C., Zhao, H. and Fan, Z., 2019. Additive Manufacturing of Thin Alumina Ceramic Cores Using Binder-Jetting. *Additive Manufacturing*, [e-journal] 29(100802), pp. 1–16. <http://dx.doi.org/10.1016/j.addma.2019.100802>.

Jakus, A. E., 2018. An Introduction to 3D Printing—Past, Present, and Future Promise. In: M. Dipaola and F. M. Wodajo, eds. 2019. *3D Printing in Orthopaedic Surgery*. Missouri: Elsevier. pp. 1–15.

Jasveer, S. and Jianbin, X., 2018. Comparison of Different Types of 3D Printing Technologies. *International Journal of Scientific and Research Publications (IJSRP)*, [e-journal] 8(4), pp. 1–9. <http://dx.doi.org/10.29322/ijsrp.8.4.2018.p7602>.

Junji, H. and Sandström, S., 2013. *Investigation of a 3D printer*. [online] Sweden. Available at: <https://www.diva-portal.org/smash/get/diva2:708219/FULLTEXT01.pdf> [Accessed 8 August 2019].

Kamal, M., Abdelrazek, E.M., Sellow, N.M. and Abdelghany, A.M., 2018. Synthesis and optimization of Novel Chitosan/Cellulose Acetate Natural Polymer Membrane for water treatment. *Journal of Advances in Physics*, 14(1), pp. 5303–5311.

Kamide, K. and Saito, M., 1985. Thermal Analysis of Cellulose Acetate Solids with Total Degrees of 0.49, 1.75, 2.46, and 2.92. *Polymer Journal*, [e-journal] 17(8), pp. 919–928. <http://dx.doi.org/10.1295/polymj.17.919>.

Kang, S. L., 2005. *Sintering: Densification, Grain Growth & Microstructure*. Oxford: Elsevier Butterworth Heinemann.

Kim, Y., Hong, S. and Kim, D., 2000. Anisotropic Abnormal Grain Growth in TiO₂ / SiO₂ -Doped Alumina. *J. Am. Ceram. Soc.*, 83(11), pp. 2809–2812.

Kumar, R., Prabhakar, V. and Saini, J., 2013. Alumina. *International Journal of Current Engineering and Technology*, 3(5), pp. 1679–1685.

Lin, F. J. T., Jonghe, L. C. De and Rahaman, M. N., 1997. Microstructure Refinement of Sintered Alumina by a Two-Step Sintering Technique. *J. Am. Ceram. Soc.*, 80(9), pp. 2269–2277.

- Long, Y., Pan, J., Zhang, Q. and Hao, Y., 2017. 3D printing technology and its impact on Chinese manufacturing. *International Journal of Production Research*, [e-journal] 55(5), pp. 1488–1497. <http://dx.doi.org/10.1080/00207543.2017.1280196>.
- Mamatha, S., Biswas, P., Ramavath, P., Das, D and Johnson, R., 2018. 3D printing of complex shaped alumina parts. *Ceramics International*, [e-journal] 44(16), pp. 19278–19281. <http://dx.doi.org/10.1016/j.ceramint.2018.07.153>.
- Matsunaga, K., Nakamura, A., Yamamoto, T. and Ikuhara, Y., 2003. First-principles study of defect energetics in titanium-doped alumina. *Physical Review B*, [e-journal] 68(214102), pp. 1–8. <http://dx.doi.org/10.1103/PhysRevB.68.214102>.
- McKeen, L. W., 2019. *The Effect of UV Light and Weather on Plastics and Elastomers*. Oxford: Elsevier.
- Michálek, M., Michálková, M., Blugan, G. and Kuebler, J., 2017. Effect of carbon contamination on the sintering of alumina ceramics. *Journal of the European Ceramic Society*, [e-journal] 38(1), pp. 193–199. <http://dx.doi.org/10.1016/j.jeurceramsoc.2017.08.011>.
- Mohamed, G. and Hegazy, R., 2017. Comparison of GUM and Monte Carlo methods for the uncertainty estimation in hardness measurements. *International Journal of Metrology and Quality Engineering*, [e-journal] 8(14). <http://dx.doi.org/10.1051/ijmqe/2017014>.
- Muhammad, H. K., 2015. *Key Features of Materials for the Fused Deposition Modelling Process*. MSc. University of Minho.
- Peng, Z., Luo, X., Xie, Z., An, D. and Yang, M., 2018. Effect of print path process on sintering behavior and thermal shock resistance of Al₂O₃ ceramics fabricated by 3D inkjet-printing. *Ceramics International*, [e-journal] 44(14), pp. 16766–16772. <http://dx.doi.org/10.1016/j.ceramint.2018.06.108>.
- Pigram, A. J. and Freer, R., 1995. The Effect of Binder Additions on the Green and Sintered Properties of Mn-Zn Ferrite Ceramics. *Ceramics International*, 21, pp. 33–41.
- Pulgarín, H. L. C. and Albano, M. P., 2015. Sintering and Microstructure of Al₂O₃ and Al₂O₃-ZrO₂ Ceramics. *Procedia Materials Science*, [e-journal] 8, pp. 180–189. <http://dx.doi.org/10.1016/j.mspro.2015.04.062>.
- Puls, J., Wilson, S. A. and Hölder, D., 2011. Degradation of Cellulose Acetate-Based Materials: A Review. *Journal of Polymers and the Environment*, [e-journal] 19, pp. 152–165. <http://dx.doi.org/10.1007/s10924-010-0258-0>.
- Rahimian, M., Ehsani, N., Parvin, N. and Baharvandi, H. R., 2009. The effect of particle size, sintering temperature and sintering time on the properties of Al – Al₂O₃ composites, made by powder metallurgy. *Journal of Materials Processing Technology*, [e-journal] 209(14), pp. 5387–5393.

<http://dx.doi.org/10.1016/j.jmatprotec.2009.04.007>.

Roy, J. F., Descemond, M., Brodhag, C. and Thevenot, F., 1993. Alumina microstructural behaviour under pressureless sintering and hot-pressing. *Journal of the European Ceramic Society*, [e-journal] 11(4), pp. 325–333. [http://dx.doi.org/10.1016/0955-2219\(93\)90032-M](http://dx.doi.org/10.1016/0955-2219(93)90032-M).

Ruslam, R., 2009. *Fabrication of alumina crucible*. B. Eng.. Universiti Teknikal Malaysia Melaka.

Schwab, K., 2016. *The Fourth Industrial Revolution*. Switzerland: World Economic Forum.

Singh, R. and Garg, H. K., 2016. Fused Deposition Modeling – A State of Art Review and Future Applications, Reference Module in Materials Science and Materials Engineering. *Reference Module in Materials Science and Materials Engineering*, [e-journal] 2016, pp. 1–20. <http://dx.doi.org/10.1016/b978-0-12-803581-8.04037-6>.

Sofia, D., Barletta, D. and Poletto, M., 2018. Laser sintering process of Ceramic powders : the effect of particle size on the mechanical properties of sintered layers. *Additive Manufacturing*, [e-journal] 23, pp. 215–224. <http://dx.doi.org/10.1016/j.addma.2018.08.012>.

Taffner, U., Carle, V., Schafer, U. and Hoffmann, M. J., 2004. Preparation and Microstructural Analysis of High-Performance Ceramics. *ASM Handbook*, 9, pp. 1059–1066.

Theivasanthi, T. and Alagar, M., 2013. *Titanium dioxide (TiO₂) Nanoparticles - XRD Analyses – An Insight*. Tamilnadu: Centre for Research and Post Graduate Department of Physics, Ayya Nadar Janaki Ammal College.

Ting, C. H., Tan, C. Y., Ramesh, S., Sopyan, I. and Teng, W. D., 2008. *Sintering Behaviour of TiO₂-doped Alumina for Biomedical Application*. Kuala Lumpur: Universiti Malaya.

Trivedi, M. K., Nayak, G., Patil, S., Tallapragada, R. M. and Mishra, R., 2015. Impact of Biofield Treatment on Chemical and Thermal Properties of Cellulose and Cellulose Acetate. *Journal of Bioengineering & Biomedical Science*, [e-journal] 5(3), pp. 1–7. <http://dx.doi.org/10.4172/2155-9538.1000162>.

Varghese, G., Moral, M., Castro-garcía, M., López-lópez, J. J., Marín-rueda, J. R., Yagüe-alcaraz, V., Hernández-afonso, L., Ruiz-morales, J. C. and Canales-vázquez, J., 2017. Fabrication and characterisation of ceramics via low-cost DLP 3D printing. *Boletín de la Sociedad Española de Cerámica y Vidrio*, [e-journal] 57(1), pp. 9–18. <http://dx.doi.org/10.1016/j.bsecv.2017.09.004>.

Wong, K. V. and Hernandez, A., 2012. A Review of Additive Manufacturing. *International Scholarly Research Network Mechanical Engineering*, [e-journal] 2012(208760), pp. 1–10. <http://dx.doi.org/10.5402/2012/208760>.

Yan, Q., Dong, H., Su, J., Han, J., Song, B., Wei, Q. and Shi, Y., 2018. A Review of 3D Printing Technology for Medical Applications. *Engineering*, [e-journal] 4(5), pp. 729–742. <http://dx.doi.org/10.1016/j.eng.2018.07.021>.

Zaitsev, S. V., Doroganov, V. A., Doroganov, E. A. and Evtushenko, E. I., 2017. Study of Artificial Ceramic Binder Properties in the System $\text{Al}_2\text{O}_3\text{-SiO}_2\text{-SiC}$. *Refractories and Industries Ceramics*, [e-journal] 57(5), pp 526–530. <http://dx.doi.org/10.1007/s11148-017-0017-z>.

Zhang, S., Sha, N. and Zhao, Z., 2016. Surface modification of $\alpha\text{-Al}_2\text{O}_3$ with dicarboxylic acids for the preparation of UV-curable ceramic suspensions. *Journal of the European Ceramic Society*, [e-journal] 37(4), pp. 1607-1616. <http://dx.doi.org/10.1016/j.jeurceramsoc.2016.12.013>.

Zhou, M., Liu, W., Wu, H., Song, X., Chen, Y., Cheng, L., He, F., Chen, S. and Wu, S., 2016. Preparation of a defect-free alumina cutting tool via additive manufacturing based on stereolithography – Optimization of the drying and debinding processes. *Ceramics International*, [e-journal] 42(10), pp. 11598–11602. <http://dx.doi.org/10.1016/j.ceramint.2016.04.050>.

APPENDICES

Appendix A: Sample Calculation

Sample Calculation for Bulk Density

Example Calculation for CA-Acetone Concentration 200 g/L with Binder Loading 80 vol%.

$$\rho = \left(\frac{w_a}{w_a - (w_w - (w_{a+w} - w_a))} \right) \rho_w$$

Where

ρ = Sample's bulk density, g/cm³

w_a = Sample's weight in air or dry weight, g = 0.6002 g

w_w = Sample's weight in water or wet weight, g = 0.4410 g

w_{a+w} = Wet sample's weight in air or wet dry weight, g = 0.6430 g

ρ_w = Distilled water density = 0.997 g/cm³ at 25 °C

$$\rho = \left(\frac{0.6002 \text{ g}}{0.6002 \text{ g} - (0.4410 \text{ g} - (0.6430 \text{ g} - 0.6002 \text{ g}))} \right) 0.997 \frac{\text{g}}{\text{cm}^3}$$

$$\rho = 2.963 \frac{\text{g}}{\text{cm}^3}$$

$$\begin{aligned} \text{Relative Density} &= \frac{\rho}{\text{Theoretical Density}} \times 100 \% = \frac{2.963}{3.95} \times 100 \% \\ &= 75.01 \% \end{aligned}$$

Sample Calculation for Hardness

Example Calculation for One of the Sample Test for CA-Acetone Concentration
150 g/L with Binder Loading 80 vol%.

$$D = \frac{D_1 + D_2}{2}$$

$$H_V = \frac{2F \sin \frac{136}{2}}{D^2} = \frac{1.854F}{D^2}$$

Where

H_V = Vickers hardness, kg/mm²

F = Applied load, N

D = Arithmetic mean of two diagonals, D_1 and D_2 , μm

$$D = \frac{103.69 + 100.17}{2} \mu\text{m} = 101.93 \mu\text{m}$$

$$H_V = \frac{1.854(2 \text{ kg}F)}{(101.93 \mu\text{m})^2} = 356.9 \frac{\text{kg}}{\text{mm}^2} = 3501 \text{ MPa}$$